Aerosol Ion Mobility based Techniques for the Improved Analysis of Chemical Mixtures

A DISSERTATION

SUBMITTED TO THE FACULTY OF

UNIVERSITY OF MINNESOTA

BY

Jihyeon Lee

IN PARTIAL FULFILLMENT OF THE REQUIREMENTS

FOR THE DEGREE OF

DOCTOR OF PHILOSOPHY

Professor Christopher J. Hogan Jr.

April 2022

Acknowledgment

This dissertation is the culmination of my research during my PhD program at the University of Minnesota. I am tremendously grateful to everyone who has contributed to this work by guiding me to conduct this study with their scientific knowledge or by providing me with their warm and unconditional support.

First, I would like to express huge gratitude to my advisor Dr. Chris Hogan who made all this research happen. His intelligence and passion always inspired me to pursue the completion of this research and his broad expertise in a range of areas provided me with opportunities to work on diverse projects with collaborators from different fields. The scientific knowledge, problem solving ability, and mindsets I learned from him will last with me my entire career as a researcher. Lastly, I can't thank him enough for always being caring and supportive.

I am also grateful to Dr. Cari Dutcher, Dr. William Northrop, and Dr. Kenneth Leopold for being part of the committee for my preliminary exam and for my final defense. Their feedback was essential for the completion of my dissertation. Fortunately, I had an opportunity to do my first internship at Kanomax FMT and the experience at KFMT trained me to have more practical approach thanks to Dr. Siqin He, Dr. Derek Oberreit, their products, and all the other employees I worked with. Especially, the first two studies in this dissertation would not have been possible without their supports and systems. Lastly, I would like to thank my previous advisor Dr. Jungho Hwang who guided me through my master's work at Yonsei University and encouraged me to pursue my PhD at the University of Minnesota.

I must admit that it has been a miracle that I have been surrounded by such amazing colleagues in our lab. I thank Dr. Bernard Olson, Ian Marabella, Dr. Eirini Goudeli, Dr. Souvik Ghosh, David Buckley, Dr. Steven Fredericks, Dr. Jikku Thomas, Dr. Chenxi Li, Dr. Xiaoshuang Chen, Dr. Huan Yang, Dr. Yensil Park, Dr. Toshiato Ono, Dr.Shyam Kumar, Dr. Li Li, Dr. Hui Yang, Dr. Tomoya Tamadate, Yuechen Qiao, Guanyu Song, Austin Andrews, Stephanie Eilts, and Abhilash Ojha (and all the others) for all the knowledge, help, and memories we have shared. The time I spent in our lab will be a very precious chapter of my life.

I want to express extreme gratitude to my friends and family for the consistent and unconditional support during my entire life. Even though I can't list everyone, I really appreciate that they have been on my side here in Minnesota, and in Korea, and around the world. Especially, I owe an immense debt for the invaluable support from my parents Namsoon Kim and Donku Lee, as well as my brother Chiwoo Lee, my sister-in-law Hyunsu Lee, Ohee Kwon and Jinyoung Kim, Jill, Greg, Shelby, and Faith from the lovely Dvergsten family, and my fiancé Isaac Dvergsten. Isaac, I was able to make it thanks to you.

To my parents

Abstract

Particle and ion separations in the gas phase are typically based upon ion mobility (K), also often called the electrical mobility, or simply, the mobility. The mobility is the proportionality coefficient between the steady velocity a particle (charged) moves with and the magnitude of an applied external electric field driving motion. At low electric field strengths, particles are in thermal equilibrium with ambient gas molecules, and the mobility is a constant value independent of field strength. Under these conditions, the mobility is largely a function of particle size, and can be linked to particle diameter. Meanwhile, at high electric field, the translational kinetic energy of charged particles and ions exceeds the thermal energy of gas molecules, and this leads to deviations from thermal equilibrium. Under these conditions the mobility is a function of the field strength, specifically the ratio of the field strength to the gas number density (*E/N*).

The goal of the studies described here was to exploit ion mobility measurement principles in numerous new ways, at both low and high field strengths, to develop particle analysis techniques amenable not only to aerosol particles, but also to particles from liquid suspensions introduced into the gas phase via sprays. The first portion of my dissertation research focuses on an air-jet nebulizer-IMS system consisting of a nanoparticle nebulizer (NPN), a differential mobility analyzer (DMA), and a condensation particle counter (CPC) for the size analysis of chemical mechanical planarization (CMP) slurries. For silica slurries, an air-jet nebulizer-IMS system showed better repeatability and capability for multimodal size distributions. For non-silica slurries, the air-jet nebulizer-IMS system, DLS, and EM differed from each other with peak size shifts of 10 nm or less.

The second portion of my dissertation focuses on an IMS-IMS system consisting of two nano DMAs to examine vapor binding to protein molecules in the gas phase. These experiments were performed to determine if vapor binding, leading to mobility shifts, was vapor and protein specific, which would lead to expanded separation capabilities with IMS. In the experiments, the first DMA determined the mobility of protein ions at atmospheric pressure conditions and the second DMA examined shifts in their mobility after the introduction of condensable vapor molecules. It is found that low charge state protein ions adsorb water, nonane, and 1-butanol vapor molecules and the affinity of protein ions to nonane is shown to be higher than to butanol or water when κ- Köhler theory is applied to experimental results.

The third portion of my dissertation research focuses on an IMS-DMS system consisting of a DMA and a field asymmetric ion mobility spectrometer (FAIMS). This system allows a tandem mobility analysis by separating ions both at low field limit and at high field limit. Importantly DMA-FAIMS analysis also enables determination of the actual mobility versus *E/N* function in a single system. This study also results in the realization of a DMA-FAIMS system and demonstrates the capability of separating ions with the same mobility; benefitting analysis methods in atmospheric new particle formation events and detection of pesticide volatility.

The last portion of my dissertation focuses on a Langevin dynamics simulation of particulate film deposition with polydisperse and agglomerated particles. While distinct from the other studies in that it is numerical, the simulations depend upon modeling particle equations of motion, which are also the fundamental equations governing IMS separation. Simulation-deposited films are characterized based their porosities and pore size

distributions which are incorporated into calculation of thermal conductivities. The results suggest that the pore size distribution is highly dependent on porosity regardless of other parameters and particle deposited films can achieve comparable thermal conductivities to conventional aerogels.

Table of contents

List of Tables

List of Figures

Chapter 1. Introduction

Characterization of charged particles or ions in the gas phase based on their mobility is a measurement approach of central importance in aerosol science and in chemical physics (Mason and McDaniel, 1988a, Cohen and Karasek, 1970). The mobility is the proportionality coefficient for an ion or charged particle between its velocity and an external electric strength in a bath gas. The prevalence of ion mobility spectrometry (IMS) can be explained in part by its fast measurement time, instrumental simplicity, and portability which make it highly advantageous in real time detection of drugs, chemical warfare agents, explosives, and pollutants (Makinen et al., 2010, O'Donnell et al., 2008, Kafle et al., 2016, Ewing et al., 2001, Eiceman and Stone, 2004, Covington et al., 2015, Roehl, 1991).

IMS, and charged particle measurements in the gas phase, also generally provide easy-to-interpret information, and for this reason, many seminal discoveries of the past century utilized such measurement principles. IMS hinges upon a balance between electrostatic forces and drag forces acting on a moving object. In the early 1900s, implementation of IMS led to discoveries including but not limited to Millikan's oil droplet measurements (Millikan, 1911, Millikan, 1923) which determined the charge of a single electron, verified Stokes's law within the continuum limit, and determined the slip correction factor for Stokes law. Cloud chamber experiments (Wilson, 1933, Wilson, 1912, Wilson, 1911), also leveraging the properties of charged particles and ions in the gas phase, served as the very first sub-atomic particle detectors. IMS still plays an important role in fundamental measurements in chemical physics (Cumeras et al., 2015a), and there continues to be numerous efforts to improve IMS performance and expand its applications,

including development of new system designs (planar to cylindrical, higher sheath flow rate, high frequency wave forms, higher field strength, smaller channel size, different carrier gas, etc.; Krylov, 2003, Rosser and De La Mora, 2005, Miller et al., 2001, Barnett et al., 2000), and advances in theorical and analytical models (charging kinetics, diffusion broadening, and collision coefficient; Stolzenburg and McMurry, 2008, Li et al., 2020b, Thajudeen et al., 2012, Gopalakrishnan and Hogan Jr, 2011).

The use of IMS as a hyphenated system with other techniques such as electrospray ionization, air-jet nebulizer, liquid chromatography, and mass spectrometry has also been shown to be an effective method to extend the applications of IMS (Jeon et al., 2016c, Fenn et al., 1989, Baker et al., 2010, Thomas et al., 2016, Cumeras et al., 2015b). One of most widely used hyphenated systems is an ion mobility-mass spectrometry (IM-MS). In IM-MS system, analytes are classified based on their mobility by an IMS and a mass spectrometer then measures the mass-to-charge ratio (m/z) of mobility selected ions. This yields two-dimensional analysis in both mobility and mass. IM-MS techniques are used in the detection of biomolecules, viruses, and volatile organic compounds (VOCs; Valentine et al., 2006, Armenta et al., 2011, Hogan and de la Mora, 2011). However, mass spectrometers remain expensive and are difficult to make portable. There are several IMS based hyphenated systems which have not been fully explored including combinations of mobility analyzers themselves such as differential mobility analyzers (DMAs) and field asymmetric ion mobility spectrometers (FAIMSs). Furthermore, IMS can function as a powerful analysis tool for hydrosol samples when it is connected to improved aerosolization sources (Jeon et al., 2016c, Jeon et al., 2016b). Motivated by the unexplored potential of IMS in hyphenated methods and in optimizing aerosol technology for chemical

analysis, the purpose of the studies carried out in this dissertation are to implement newly hyphenated systems and to optimize already existing systems to expand the usage of gas phase ion mobility spectrometry technologies.

1.1 Ion mobility spectrometry

When an electric field (E) is applied in a gas laden with ions or charged particles, the drift velocity (v_d) of the ions or particles is determined by a balance between the electrostatic force and drag force on the ion/particle. In low Reynolds number and low Mach number limit, the drift velocity can be determined by first examining the force balance equation on a particle:

$$\mathrm{m}\frac{dv_d}{dt} = -f(v_d - u) + qE \tag{1.1}$$

where m is an ion/particle mass, f is the friction factor of an ion/particle, u is the velocity of the fluid, and q is charge of an ion/particle. For ions/particles with nanometer scale, the inertia term on the left side can be neglected, simplifying equation (1.1) into equation (1.2):

$$f(v_d - u) = qE\ . \tag{1.2}$$

In equation (1.2), the proportionality factor between v_d and E, which is called ion/particle mobility (K), is given by $\frac{q}{f}$. The friction factor for particles/ions depends on the collisionality of gas molecules as they approach the particle. Collisionality is determined by the Knudsen number (K_n), which is the ratio of particle radius (a_p) to mean free path of gas molecules (λ). For particles significantly larger than the mean free path of gas molecules ($K_n \to \infty$), f is determined via Stokes's law (Fuchs and Stechkina, 1962):

$$f_c = 3\pi\mu d_p \tag{1.3}$$

where ‘c’ indicates the continuum (fully collisional) limit, μ is the gas dynamic viscosity, and d_p is particle diameter. The friction factor in the free molecular (collisionless) limit ($K_n \to 0$) is determined as follows (Epstein, 1924, Tammet, 1995, Mason and McDaniel, 1988a, Zhang et al., 2012b, Larriba and Hogan Jr, 2013, Revercomb and Mason, 1975a):

$$f_{FM} = \frac{4}{3}\rho \bar{c} \Omega \tag{1.4}$$

where ‘FM’ indicates the free molecular limit, ρ is density of the gas, $\bar{c}$ is the mean thermal speed of the reduced mass of ions/particles and gas molecules, and Ω is the collision cross section of ions/particles. For particles with known density and spherical structure, the collision cross section can be expressed as follows:

$$\Omega = \xi\pi \frac{{d_p}^2}{4} \tag{1.5}$$

where ξ is the momentum transfer coefficient between ion/particles and gas molecules (Millikan, 1923, Rader, 1990, Kim et al., 2005, Ku and de la Mora, 2009, Hogan and de la Mora, 2011, Larriba et al., 2011b). ξ is empirically determined as 1.36 at standard conditions but also inferred by comparison of equation (1.4) and equation (1.6) which describes the friction factor in the transition regime between two limits via Stokes-Millikan equation (Millikan, 1911):

$$f = \frac{3\pi\mu d_p}{C_C(K_n)} \tag{1.6}$$

Cunningham slip correction factor ($C_C(K_n)$) corrects the deviation of small ions/particles from the no-slip boundary condition of Stokes’s law and is written as (Cunningham, 1910):

$$C_c(Kn) = 1 + Kn * \left(A_1 + A_2 \exp\left(\frac{-A_3}{Kn}\right)\right) \tag{1.7}$$

where A_1, A_2, *and* A_3 are empirically determined constants (Davies, 1945a). Equation (1.6) converges to equation (1.3) and (1.4) at each limit. Hence, the mobility of ions/particles not in the free molecular regime can be written as follows:

$$K = \frac{qC_c}{3\pi\mu d_p} \tag{1.8}$$

In the free molecular regime, the mobility of spherical ions/particles is described as:

$$K = \frac{q}{\frac{4}{3}\rho\bar{c}1.36\pi\frac{{d_p}^2}{4}} \tag{1.9}$$

Additional corrections are needed in equation (1.9) for small particles to account for the finite size of gas molecules (d_g; Larriba et al., 2011b). As noted on the previous page, to ensure the validity of equations (1.8) and (1.9), the particles or ions must be in the low Mach number limit. Stated differentially, ion/particle mobility can be determined by equations (1.8) and (1.9) at low electric field strengths where ions/particles are in thermal equilibrium with ambient gas molecules, and the gas molecule mean thermal speed is significantly higher than the drift velocity. Under this condition, gas molecule particle collisional velocities are largely determined by the thermal energy of the gas, and the impinging gas molecule velocity distribution is determined by the thermal equilibrium distribution with the superposition of a small drift component from the electric field (Mason and McDaniel, 1988a). Therefore, the steady-state drift velocity is usually determined in a short time after a few collisions with gas molecules, enabling the use of constant *K* based on equation (1.8) and (1.9). In contrast, at high electric field ions/particles drift much faster than the mean thermal speed of the surrounding bath gas. At extremely high field strengths, gas molecule-particle collisional velocities are governed by the electric field and the effect of thermal energy significantly deceases in this high field limit. K,

therefore, cannot be considered as a constant but is a function of the ratio of electric field to the number density of gas molecules (*N*). Often, this function is expressed as follows (Mason and McDaniel, 1988b):

$$\mathrm{K}\left(\frac{E}{N}\right) = K_0 \frac{N_0}{N}\left(1 + \alpha_2 \left(\frac{E}{N}\right)^2 + \alpha_4 \left(\frac{E}{N}\right)^4 + \cdots\right) \tag{1.10}$$

where K_0 is the standard mobility at low field limit (which is determined by equation (1.8) or (1.9)), N_0 is gas number density at standard conditions, and α_2 and α_4 are parameters which are ion/particle chemical composition, size, gas molecule chemical composition, and gas temperature dependent, and are usually fit (not calculated) to describe mobility variation as a function of *E/N* (Ellis et al., 1976, Ellis et al., 1978, Viehland and Mason, 1995). Noticeably, *K* is not a function of individual *E* or *N* since the drift velocity is determined by the acceleration magnitude determined by E and acceleration time between collisions which is inversely proportional to *N* (Tyndall, 1938, Mason and McDaniel, 1988a). The unit for *E/N* is denoted as townsend (Td) where $1\mathrm{Td} = 10^{-17}\, V/cm^2$ (Huxley et al., 1966). The electric field is considered to be at low field limit when the field energy gained from *E* is significantly smaller than thermal energy by the gas and to be at high field limit when the inequality is reversed (Revercomb and Mason, 1975a).

With the definition of mobility noted, ion mobility spectrometry (IMS) is an analytical technique that separates ionized analytes in the gas phase based on their mobility. Conventional ion mobility spectrometers (IMSs) separate analytes based on the constant ion mobilities at low field limit. Drift tube Ion mobility spectrometers (DTIMSs) and differential mobility analyzers (DMAs) are conventional IMSs. Differential mobility analyzers (DMAs) are the most commonly encountered type of spatial spectrometer; they are widely used in aerosol science. In DMAs (depicted in Figure 1.1) fluid flow drives

analyte motion in one direction (and all analytes move at the same speed in this direction) and an external constant electric field drives mobility dependent analyte motion in an orthogonal direction (Chen et al., 1998). Analytes hence take mobility dependent trajectories, i.e. they are spatially separated. The instrument inlet and outlet are at precise points, and because of these spatially dependent trajectories, only analytes of a specific mobility (or falling within a specific mobility window) are transmitted from inlet to outlet. The mobility selected for transmission can be easily tuned in a DMA by increasing or decreasing the strength of the applied electric field.

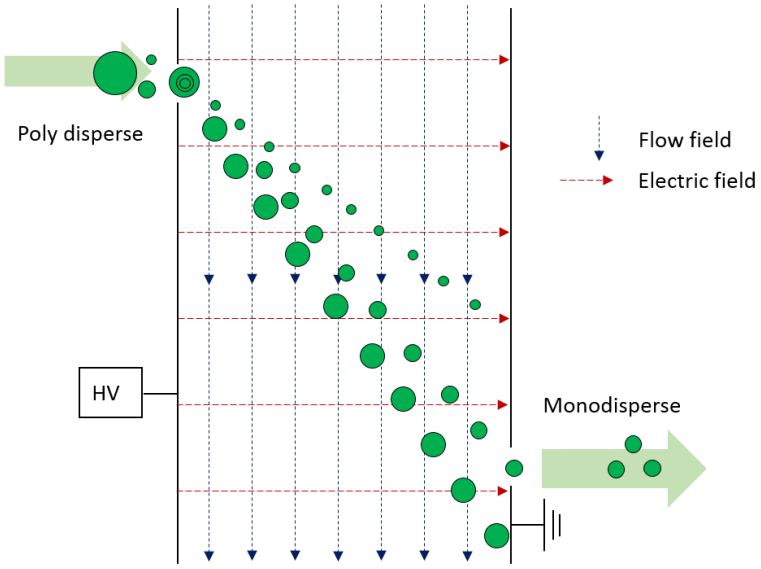

Figure 1.1 A schematic diagram of the operating principle of a differential mobility analyzer.

Conversely, similarly named differential mobility spectrometers (DMSs) classify analytes based on the difference in ion mobility at low field and high field, which is measured by applying a time-dependent, asymmetric electric field as shown in figure 1.2 (hence DMSs are also called FAIMSs, field asymmetric ion mobility spectrometers).

FAIMSs utilize this dependency of mobility on *E/N* to separate gas-phase ions. In a FAIMS system, alternating high and low electric fields are generated by a waveform generator and applied to a set of plates or concentric cylindrical electrodes. A high electric field (E_h), generated upon application of the maximum voltage to a FAIMS unit (called the dispersion voltage, DV), is applied for a shorter period of time (t_h) and a low electric field (E_l), is applied for a longer time (t_l). Over a period, the absolute values of E_h t_h and $E_l t_l$ are equal. If mobility was not a function of field strengths, all ions would be transmitted through the device. However, since the mobility of an ion differs at E_h and E_l, ions begin to drift to one of the electrodes and finally reach the surface of an electrode as shown in Figure 1.2(a). Ions depositing on an electrode can be transmitted through the system by applying a small dc potential called the compensation voltage (CV) as shown in Figure 1.2 (b); the field brought about by CV application can cancel out the ion drift towards an electrode. CV is hence a function of the difference between an ion's mobility at low field and at high field strengths. A FAIMS can transmit particular ions allowing separation of ions by adjusting CV.

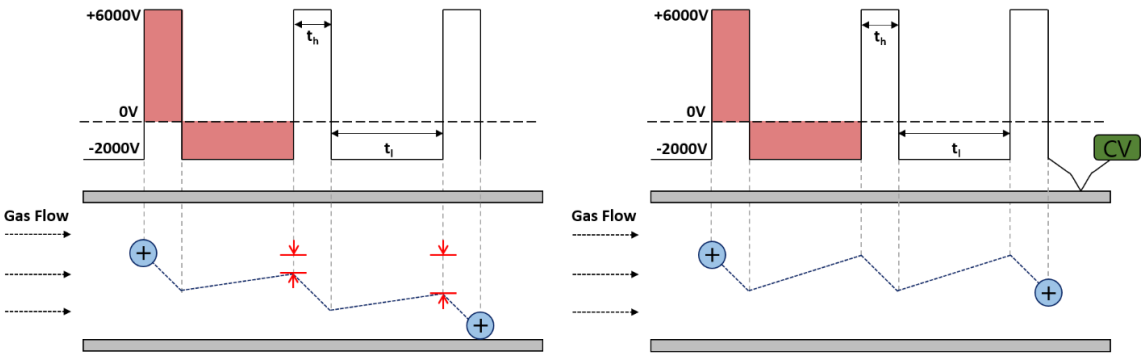

Figure 1.2 (a) A trajectory of an ion in FAIMS without compensation voltage **(b)** A trajectory of an ion in FAIMS with compensation voltage applied.

1.2 Dissertation summary

After this introductory chapter, there are three chapters focusing on IMS hyphenated techniques, i.e. the development of a new technique or optimization of an existing technique requiring separation of charged particles in the gas phase based upon their physical chemical properties.

Chapter 2 focuses on the characterization of CMP slurry particles utilizing the IMS system consisting of an air-jet nebulizer, a differential mobility analyzer (DMA), and a condensation particle counter (CPC). This study compared the size distribution of 8 commercial slurries including SiO_2, Al_2O_3, ZrO_2, and CeO_2 to those obtained by dynamic light scattering (DLS) and electron microscopy (EM). Further evaluation on the system was conducted to demonstrate the conversion process of aerosol concentration to hydrosol concentration and to examine the distortion of particle size distribution by agglomeration and non-volatile residue (NVR) particles during the aerosolization process.

Chapter 3 utilized an IMS-IMS system consisting of two nano DMAs to investigate vapor uptake by low charge state protein ions. Ion mobilities of protein ions in low field strength measurements are single scalar values and can be affected by Coulombic stretching. Here, we used a nano particle nebulizer and a Kr-85 source to maintain the low charge states on the surface of protein ions. Through tandem IMS measurements, we measured the mobility shifts of protein ions with introduction of vapor molecules (water, nonane, and 1-butanol) in addition to their mobility at low field strength.

Chapter 4 implements an IMS-DMS system consisting of a half mini DMA and a field asymmetric waveform ion mobility spectrometry (FAIMS), wherein a half mini DMA separates ions based on mobility at low field strengths, after which the FAIMS separates

ions based upon the differences in mobility at low field strength and high field strength. In this study, tetrabutylammonium iodide (TBAI), tetraheptylammonium bromide (THAB), tetradecylammonium bromide (TDAB), and tetradodecylammonium bromide (TDDAB) were aerosolized and ionized by an electrospray. Then, they were analyzed by the DMA and by the FAIMS consecutively. The mobility dependency of 4 ions were predicted based on the truncated form of α function shown in equation (1.10).

Chapter 5 is a standalone simulation study on the deposition of particulate films expanding up a study performed by a former member of our lab (Lindquist et al., 2014). Aerosol deposition methods yield sub micrometer thin films and the structures of the resulting films depend on the physics of particle transport to the substrate and the characteristics of the primary particles. This study investigated the effects of polydispersity and morphology of particles on the properties of deposited particulate films formed via Langevin dynamics simulation. The pore size distribution and the porosity of the films were analyzed, and a gas thermal conductivity model was developed to consider non-continuum effects in the pores. The calculated thermal conductivity was compared to measured thermal conductivities of silica aerogels determined from previous studies.

Chapter 2. Size Distribution Monitoring for Chemical Mechanical Polishing Slurries: An Intercomparison of Electron Microscopy, Dynamic Light Scattering, and Differential Mobility Analysis

Adapted from: Jihyeon Lee, Siqin He, Guanyu Song, and Christopher J. Hogan Jr. "Size distribution monitoring for chemical mechanical polishing slurries: An intercomparison of electron microscopy, dynamic light scattering, and differential mobility analysis." Powder Technology 396 (2022): 395-405.

Abstract: In chemical mechanical planarization (CMP), a particle slurry is used to polish semiconductor wafers. Key to its performance is the size distribution of the particles. We evaluate the potential of an aerosol technique, namely differential mobility analysis (in a liquid nanoparticle sizer, LNS, system) to characterize size distributions of CMP slurries. LNS measurements are compared to size distributions inferred from electron microscopy (SEM), and dynamic light scattering (DLS). LNS measurements are more repeatable than DLS measurements, and for 4 silica slurries, LNS distributions are in better agreement with SEM measurements than DLS. We find also that the LNS can quantify multimodal size distributions. For non-silica slurries, LNS, DLS, and SEM measurements have geometric mean diameters which can vary from another by 10 nm or more. However, because each measurement type is internally consistent, the combination of LNS and DLS, which are automated, yields augmented information on slurry properties.

2.1 Introduction

Chemical mechanical planarization (CMP) has been widely used in the integrated circuit (IC) industry since its development in the 1980s. A slurry is utilized in CMP, which consists of abrasive nanoparticles, an oxidizer, and organic compounds in deionized water. Prior research has examined the effects of the abrasive nanoparticle size on the removal rate in CMP. (Xie and Bhushan, 1996, Wang et al., 2020, Pohl and Griffiths, 1996, Gandhi and Borse, 2004, Choi et al., 2004, Bastaninejad and Ahmadi, 2005, Basim et al., 2000) . In general, large particles (either large primary particles or agglomerates of smaller particles) can cause defects on the wafer (Remsen et al., 2006, Kim et al., 2006) through their action with the surface. The particle size distribution parameters are significantly correlated to microscratch performance. (Eckhardt et al., 2019) The CMP process is therefore extremely sensitive to the size and shape distribution of the nanoparticles in the slurry, and the cost of slurry manufacturing accounts for nearly 50% of the total cost of the entire polishing process (Philipossian and Mitchell, 2003). Regular characterization of the complete size distribution of particles in slurries, i.e. not only the mean particle size but size, polydispersity, and distribution modality, is necessary to ensure repeatability of CMP processes.

The nanoparticles in slurries are commonly metal oxides, including but not limited to silica (SiO_2), alumina (Al_2O_3), titania (TiO_2), zirconia (ZrO_2), and ceria (CeO_2). Commercially applied CMP slurries typically do not contain highly monodisperse particles, which are prohibitively expensive to synthesize at the volumes required industrially. Instead, modestly-to-highly polydisperse suspensions wherein the particles may also be highly irregularly shaped are utilized. Such broad and non-spherical particle size

distributions present a challenge in characterization, as conventional size distribution analysis methods, namely electron microscopy (EM, with size determination of single particles) and dynamic light scattering (DLS, where distributions are fit) are often tailored to spherical, low polydispersity and unimodal distributions. There thus has been and continues to be a need to improve size distribution characterization techniques for CMP slurries, both in slurry product development and as a part of regular quality control processes.

In contrast to EM and DLS, aerosol size distribution measurement systems, specifically incorporating differential mobility analyzers (DMAs; Liu and Pui, 1974, Knutson and Whitby, 1975a) coupled with condensation particles counters (CPCs; Agarwal and Sem, 1980, McMurry, 2000, Stolzenburg and McMurry, 1991) and upstream particle charge modulation (Wiedensohler, 1988, Gopalakrishnan et al., 2015a), are capable of accurately analyzing polydisperse, multimodal particle size distributions in the 2 nm – 500 nm mobility equivalent size range. They are applicable to both spherical and irregularly shaped particles (Rogak et al., 1993, Gopalakrishnan et al., 2015b, Thajudeen et al., 2015). The DMA-CPC combination (often termed a scanning mobility particle sizer when the DMA is operated in a scanning mode; Wang and Flagan, 1990) would be advantageous to apply to CMP slurries, but its use first requires a hydrosol-to-aerosol conversion minimizing agglomeration and CMP slurry particle size change due to non-volatile residue attachment. A number of studies have previously demonstrated the hydrosol-to-aerosol conversion for aerosol based size distribution measurement along these lines. However, they largely focus on monodisperse particles and combinations of monodisperse particles. Key to these efforts has been the use of electrosprays to produce

small monodisperse droplets (De Juan and de la Mora, 1996, Lenggoro et al., 2002, Lenggoro et al., 2007, Li et al., 2020a) as well as nebulizers producing sub-micrometer droplets (Roth et al., 2015, Jeon et al., 2016c, Jeon et al., 2016b). Here, we expand upon these efforts to demonstrate that aerosol based size measurement approaches can be applied to highly polydisperse and non-spherical CMP slurry particle characterization, for more broadly distributed particles in a broad size range from 4 nm – 150 nm. Specifically, we utilize a unique small droplet size distribution nebulizer for hydrosol to aerosol conversion, with online dilution to reduce aerosolization-induced aggregation and non-volatile residue effects (Jeon et al., 2016c, Jeon et al., 2016b). The CMP slurry-aerosol is then analyzed by a DMA-CPC combination, with a soft X-ray ionizer for particle charge modulation. We compare aerosol measurements to both DLS and electron microscopy for 8 types of CMP slurries.

In describing the methods applied in the subsequent section we pay specific attention to the details of data inversion (Wiedensohler et al., 2012) utilized in aerosol measurements, examine the effect of droplet size distribution on the potential for particle agglomeration and non-volatile residue influences (Davidson et al., 2017, Li et al., 2011), and make efforts to correlate measurements to the concentration in the slurry (i.e. quantitative size distributions). For these reasons, we believe the current study advances the application of aerosol instruments in colloidal analysis. At the same time, we do note there have been several successful efforts to apply aerosol technology to CMP slurry analysis, though such studies do point to the need for a more systematic investigation for a wider variety of CMP slurries (i.e. the present study). Kim et al. (2010) appears to be the first effort to apply aerosol instruments for CMP slurry characterization, measuring the size

distribution of a silica sample and three ceria samples. They utilized a rather standard air-jet nebulizer with a commercial DMA-CPC system and compared measurements to a static light-scattering (SLS) system. Particles fell largely within the 100 nm -300 nm size range (on the larger side for CMP slurries). Good agreement was found between DMA-CPC and SLS system for silica, but unresolved differences in size distributions were observed between the two measurement systems for ceria samples. Roth et al. (2015) used an electrospray for aerosolization and measured the sizes of alumina, silica, and ceria samples in the 10 nm – 100 nm range using EM, DLS, DMA-CPC, and SP-ICP-MS (single particle inductively coupled plasma-mass spectrometry) and further estimated nanoparticle concentration using DMA-CPC, SP-ICP-MS, and ICP-OES. While their reported sizes and concentrations agreed reasonably well with one another, full size distributions were not reported from measurements, which are critical for CMP slurries. Jang et al. (2016) aerosolized CMP slurry particles using an air-jet nebulizer and measured particle size distributions in the 10 nm – 300 nm size range using a DMA-CPC, two distinct DLS systems, and EM for a ceria slurry and 3 silica slurries. Agreement in size distribution was improved between instruments in this study, but information on potential for agglomeration during aerosolization, non-volatile residue, and on the DMA-CPC data inversion routine applied was not provided. Similarly, Shin et al. (2019) measured size distributions of standard silica dispersions in the 10 nm – 300 nm size range using a DMA-CPC, DLS, and EM, using an air-jet nebulizer and a similar nebulizer to that applied in the present study. They uniquely found that DLS results were concentration-dependent but found good agreement between the DMA-CPC and EM measurements for the narrowly distributed silica suspensions studied. Finally, Kwak et al. (2020) measured the size distribution of

standard colloidal silica particles (20 nm and 80 nm) and two commercial ceria slurry abrasives below 10 nm in size using an air-jet nebulizer-DMA-CPC system, an electrospray-DMA-CPC system, and EM analysis. They highlight the importance of generating small droplets, as the air-jet nebulizer led to agglomeration during aerosolization, while with the electrospray, pH adjustment was required for dispersion stability. This study expands upon these prior works through (1) demonstrating use of a volume standard to infer nanoparticle concentration in the slurry from DMA-CPC measurements, (2) describing important details on the data inversion process applied and any sample-specific methods needed for a wider range of samples than tested previously, and (3) advancing methods to estimate the potential for agglomeration and non-volatile residue incorporation during the aerosol-to-hydrosol conversion.

2.2 Methods

We measured the size distribution of CMP slurry particles using an air-jet nebulizer-DMA-CPC system, a DLS system, and an EM system. We examined the size distribution for 4 distinct SiO_2 slurries, one Al_2O_3 slurry, a TiO_2 slurry, a ZrO_2 slurry, and a CeO_2 slurry. Each commercial water-based slurry was purchased from Nyacol Nano Technologies, Inc. The manufacturer sample names, manufacturer provided nominal size, and refractive index for the materials are summarized in Table 2.1. The refractive index for SiO_2, Al_2O_3, and TiO_2 were taken from the MALVERN reference guide and those for ZrO_2 and CeO_2 were taken from previous studies. (Wood and Nassau, 1982, Chiu and Lai, 2010) Beyond the additional sample preparation steps noted for each measurement system, samples were examined without modification.

Table 2.1 Sample name, material, data sheet provided sizes (diameters), dilution ratios for LNS (DMA-CPC) and DLS measurements, and real refractive index for the tested CMP slurries.

Sample name	Material	Nominal Size (nm)	LNS dilution ratio	DLS dilution ratio	Refractive Index
Dp7525	SiO_2	20-30	1000:1	1000:1	1.54
DP7560	SiO_2	50-60	1000:1	1000:1	1.54
DP7590	SiO_2	90-110	1000:1	1000:1	1.54
50ZKDI	SiO_2	40-60	10:1	10:1	1.54
Al25HP	Al_2O_3	70-80	1000:1	1000:1	1.77
Tisol A	TiO_2	20	1000:1	1000:1	2.59
Zr10020	ZrO_2	100	30:1 (Centrifugation)	1000:1	2.17
Ce8010	CeO_2	70-80	30:1 (Centrifugation)	30:1	2.20

2.2.1 *An air-jet nebulizer-DMA-CPC*

In air-jet nebulizer-DMA-CPC measurements, particles are nebulized under conditions wherein there are fewer than one particle per droplet, and droplet evaporation yields aerosol particles originally from a hydrosol, which are subsequently analyzed via a DMA-CPC combination with bipolar charging carried out prior to DMA measurement. For these measurements, we employed the Kanomax FMT 9310 liquid nanoparticle sizer (referred to as LNS hereafter), which incorporated a nebulizer containing an impactor to remove large droplets (nanoparticle nebulizer, NPN), an online water dilution system prior to nebulization, a soft X-ray bipolar charger (Shimada et al., 2002, Liu et al., 2020) to ionize particles, and a DMA and butanol based CPC. The LNS system target liquid particle concentration range is $3x10^7$-$3\ x10^{11}$ # mL^{-1} after all dilution; however, the number concentration in samples is unknown prior to measurement. Therefore, for all samples, a 1000:1 dilution (with ultrahigh purity water, Smith Engineering Inc) was performed offline,

prior to system injection. For samples where particles were not detected at this dilution level, the extent of dilution was progressively reduced until a signal was detected. The eventual dilution ratios applied are noted in Table 2.1. Samples of silica, alumina, and titania were directly measured by the LNS system after the dilution. We found that zirconia and ceria required additional preparation for LNS measurements due to the presence of excess non-volatile residue (NVR) particles, formed from non-volatile solutes within empty droplets. Many more empty droplets are produced than particle-containing droplets (a requirement to avoid aerosolization induced agglomeration), and NVR particle signal can overwhelm actual particle signal if the NVR particles are too large. To reduce NVR levels, we centrifuged the zirconia and ceria samples for 20 minutes at 8000 rpm in a centrifuge (Eppendorf 5418). The deposited material at the bottom of the centrifuge vial was mixed with 30 ml of ultrapure water. All samples were prepared immediately before measurement to minimize the effects of environmental changes brought on by dilution (e.g. pH changes).

During LNS measurement, each sample was first injected into the NPN using a peristaltic pump and was diluted by its online dilution with ultrapure water. We used sample flow rates in the range of 50-100 μL min^{-1} and dilution flow rates in the range of 100-200 mL min^{-1} to obtain online dilution ratios of 1000:1 to 2000:1 (hence total dilution factors in excess of 10^6 for many samples). A subsample of the diluted flow at a flow rate of 1-2 mL min^{-1} was then dispersed into a carrier gas of clean dry air flow at 0.6-0.8 L min^{-1} and the mixture of sample and the gas passed through the nebulizer, yielding small droplets. Large droplets (nominally larger than 500 nm) were removed by an impactor positioned right in front of the nebulizing disk. The resulting small droplets were

introduced to an evaporator held at 70 °C. After droplet evaporation, an additional clean gas flow of 1.0 L min^{-1} was mixed with the sample flow, and 1.5 L min^{-1} of the resulting aerosol flow was directed to the DMA (Length:10.00 inch, inner radius: 0.70 inch outer radius: 1.00 inch). The excess flow was vented directly before the outlet of the nebulizer. Only 0.6 L min^{-1} of this flow was sampled first into an ionization region for bipolar charging (with soft X-ray generated ions; Shimada et al., 2002), and then into the DMA, which was operated with a recirculating sheath flow rate of 6 L min^{-1} of air at 300 K and atmospheric pressure. DMAs act as mobility filters and 0.6 L min^{-1} of nearly monomobile particles were transmitted through the DMA to a CPC for detection. By stepping the voltage on the DMA with a log-linear slope of 0.0718 from 3.25 V – 4.77 kV with measurement times of 2 seconds per voltage, mobility spectra were collected. Each sample was measured at two online dilution ratios (1000:1 and 2000:1) and 5 replicates were obtained at each dilution ratio. As described subsequently, data inversion procedures were applied to determine particle size distributions from DMA-CPC measurements. Inversion corrects for particle charge distribution effects as well as DMA transmission efficiency, and by comparison to measurement of a standard, yields slurry particle concentration.

2.2.2 DLS measurements

A Zetasizer Nano ZS (Malvern) was used for DLS measurements. Before measurements the real and imaginary refractive index were input into the Malvern software operating the instrument for each material. For all measurements the dispersant was ultrapure water with temperature of 298 K, viscosity of 0.8872 cP, and a refractive index of 1.33. The sample temperature was set as 298 K and the equilibration time was set as 30

seconds. The cells used for measurements were disposable cuvettes (DTS0012, Malvern). The measurement angle was 175° backscatter and 5 consecutive measurements were made for each sample. Replicates (for a single measurement) were generated by the system which automatically determined the appropriate number of runs per replicate. Each individual run required a minimum duration of 10 seconds. The Malvern software provided the intensity distribution, the volume size distribution, and the number size distribution, which were normalized and used here without modification.

2.2.3 EM measurements

For EM sample collection, a Nano SpotLight system (model 9410, Kanomax FMT) was used, consisting of a NanoParticle Extractor (NPE, model 9410-00) and a NanoParticle Collector (NPC, model 9410-01; Eiguren Fernandez et al., 2014); the latter utilizes condensation to grow water droplets onto particles and subsequently inertial impaction to collect droplets onto a heated substrate. For nebulization the same offline and online dilution procedures as applied in LNS measurements were applied in EM sample preparation, and individual, unagglomerated particles were deposited in the system. Particles were deposited directly onto an EM substrate, and after the collection process, the substrates were coated with 1-3 nm of Gold or Iridium layers before EM measurements using Hitachi SU8230 and FEI Helios NanoLab G4 (scanning electron microscope, SEM).

2.3 Data processing

2.3.1 Data inversion process for Size Distributions from DMA-CPC Measurements

The output data from the LNS system is the measured particle number concentration within each mobility equivalent size bin, N_M, where the size bin corresponds to the maximally transmitted singly charged particle size for the DMA voltage applied. While data inversion procedures for DMA-CPC measurements make use of more advanced algorithms to improve accuracy (Stolzenburg and McMurry, 2008, Stolzenburg, 1988, Stratmann et al., 1997, Jiang et al., 2011, Collins et al., 2004), here we adopted a simplified approach wherein the mobility distribution (Knutson and Whitby, 1975a), $\frac{dN}{dlnZ_p}$, in the aerosol is approximated by correcting the measured values with the transmission efficiency of the DMA ε_T, the detection efficiency of the CPC $\varepsilon_{Det,}$ and the charging efficiency of the bipolar charger ε_{Chg}:

$$\frac{dN}{dlnZ_p} = \frac{N_M}{\varepsilon_T \varepsilon_{Det} \varepsilon_{Chg}} \tag{2.1a}$$

ε_{Det} is taken to be a value 1.0, as the CPC activation efficiency is high for particles in the size range examined(Liu et al., 2021), ε_{Chg} is calculated based on Wiedensholer's regression model (Wiedensohler, 1988), and ε_T is the ratio of the aerosol flowrate to the sheath flowrate of 0.1. Multiple charge correction, diffusional broadening (Stolzenburg, 2018), and inlet/outlet effects (Mai et al., 2018) were omitted in the current data inversion. The mobility distribution function is subsequently converted to a size distribution $\frac{dN}{dlnd_p}$ via the equation:

$$\frac{dN}{dlnd_p} = \frac{dN}{dlnZ_p}\left(\frac{dlnZ_p}{dlnd_p}\right) \tag{2.1b}$$

where $\frac{dlnZ_p}{dlnd_p}$ is based upon the Stokes-Millikan equation (Larriba et al., 2011b) and Z_p is also converted to $d_p$based on this equation. For the size range of interest, primarily above 10 nm, we neglected corrections for the gas molecule finite size. This simplified approach is adopted in an effort to demonstrate that it can be used to yield size distributions for spherical particles in agreement with other methods, as well as accurate particle concentrations in slurries.

2.3.2 Data inversion process for Colloidal Size Distributions from DMA-CPC Measurements

Jeon et al. (2016c) show that for a wide variety of particle types, LNS measurements can be used to determine a concentration of particles in the produced aerosol which correlates with the original colloidal concentration. Here, we expand on this finding and present a general approach to link aerosol size distribution to colloidal (slurry) size distributions. The original number concentration of particles in the slurry N_{sol} (sol particles) is linked to the aerosol number concentration (N_A) through the dilution factor (DF, combining dilution prior to injection and online dilution) and the volumetric rate of liquid entering the evaporator after removal of large droplets by the impaction during the nebulization process, denoted as VAR:

$$N_{sol} = \frac{N_A Q_A DF}{VAR} \tag{2.2a}$$

where Q_A is the aerosol flow rate leaving the nebulizer including the carrier gas flow rate (1.5 L min^{-1}). Equation (2.2a) can also be written in terms of volume fractions, i.e. the volume fraction of particles. The VAR of the NPN is first obtained by measuring the

volume concentration of aerosol particles V_{sol} in the slurry which is linked to the volume fraction in the aerosol V_A:

$$V_{sol} = \frac{V_A Q_A DF}{VAR} \tag{2.2b}$$

By using the LNS system to measure a volume standard (CT Associates, Eden Praire, MN) of spherical silica particles, where $V_{sol} = 5 \times 10^{17} nm^3 mL^{-1}$, or 0.0005 (dimensionless) with a peak diameter near 30 nm and a geometric standard deviation of 1.21, VAR can be determined for different dilution factors and aerosol flow rates as:

$$VAR = \frac{\pi Q_A DF_{VS}}{6V_{sol}} \int_{ln(10nm)}^{ln(56nm)} \frac{dN}{dlnd_p} d_p^3 \, dlnd_p \tag{2.2c}$$

In equation (2.2c), the subscript "VS" denotes the dilution factor when measuring the volume standard, and the integral represents the third moment of the aerosol size distribution over an interval found relevant for particles for the volume standard (empirically) to approximate V_A. The size distribution needed to determine VAR for the volume standard is shown in figure 2.1. Subsequently, with VAR known, the slurry size distribution function $\left.\frac{dN}{dlnd_p}\right|_{sol}$ can be determined via differentiation of equation (2.2a):

$$\left.\frac{dN}{dlnd_p}\right|_{sol} = \frac{Q_A DF}{VAR} \frac{dN}{dlnd_p} \tag{2.2d}$$

where $\frac{dN}{dlnd_p}$ is from the LNS measurement of the sample in question.

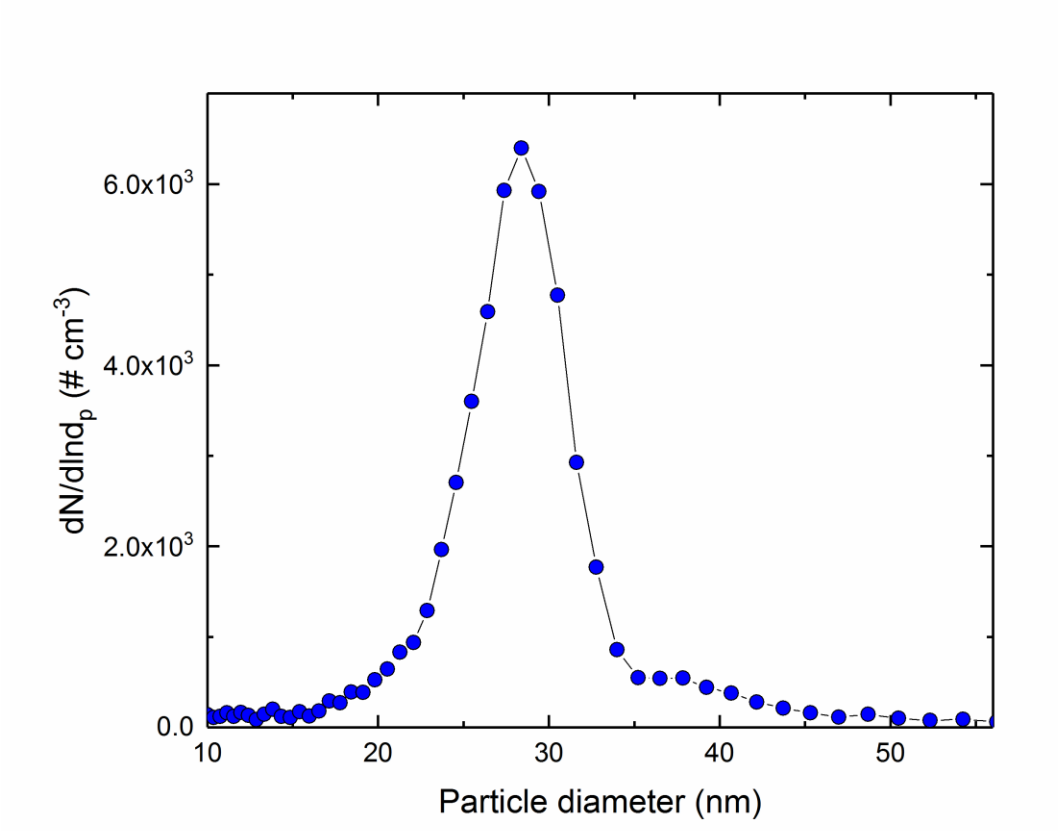

Figure 2.1 The size distribution of volume standard at dilution ratio of 10^3:1

2.3.3 Particle counting in SEM images

In examining SEM images we found the 4 colloidal SiO_2 samples and the ZrO_2 sample contained particles which can be approximated as spherical, and the diameters of 100 individual particles were used to construct histograms which were converted to normalized distributions by dividing by $\log_e$ of the bin width employed (variable increments). Meanwhile, the TiO_2 sample and Al_2O_3 sample were found to be highly non-spherical. While methods have been developed to infer gas phase mobility diameters from projections for agglomerated spheres (Chen et al., 2020, Thajudeen et al., 2015), such methods have not been generalized for arbitrary shaped particles. However, prior work also suggests that the projected area equivalent diameter is a reasonable approximation for

the mobility diameter in the free molecular and transition regimes (Rogak et al., 1993), hence for these samples we elected to utilize ImageJ to estimate the projected areas for individual particles and use projected area equivalent diameters for comparison to DMA-CPC and DLS measurements. For TiO_2, 72 particles were counted and for Al_2O_3, 100 particles were counted. The SEM analyses for CeO_2 particles were not conducted; as shown and discussed subsequently, for this sample, primary particles were not clearly discernable.

Table 2.2 Geometric mean diameter, geometric standard deviation, and mode diameter of size distributions from LNS , DLS and SEM measurements.

Sample Name	LNS			DLS			SEM		
	GMD (nm)	GSD	Mode (nm)	GMD (nm)	GSD	Mode (nm)	GMD (nm)	GSD	Mode (nm)
DP7525	24.7	1.33	28.4	35.1	1.35	32.7	29.1	1.06	30.5
DP7560	61.8	1.12	60.4	71.1	1.26	68.1	55.0	1.19	62.5
DP7590	72.3	1.70	1)37.9 2)72.3 3)103.7	88.4	1.24	78.8	84.1	1.49	102.5
50ZKDI	37.1	2.00	1)24.6 2)69.8 3)96.5	76.5	1.66	78.8	44.2	1.89	63.0
Al25HP	47.2	1.51	48.7	68.5	1.36	58.8	55.6	1.28	58.0
TiSol A	12.4	1.37	13.3	10.3	1.30	10.1	19.3	1.94	16.0
Zr10020	57.4	1.56	64.9	62.2	1.30	58.8	61.5	1.60	71.5
Ce8010	36.2	1.39	37.9	44.1	1.32	37.8	NA	NA	NA

2.4 Results & Discussion

2.4.1 Size Distribution Intercomparison

The geometric mean diameters (GMD), the geometric standard deviations (GSD), and mode diameters of LNS, DLS, and SEM measurements are summarized in table 2.2.

For distributions with multiple modes, a mode diameter is reported for each peak. For GSD and GMD calculations of LNS measurements, the peak caused by NVR was excluded (discussed subsequently, this peak is clearly identifiable in LNS spectra). We refer to table 2.2 throughout the results and discussion as it provides a summary of each measured sample type.

Beginning with silica samples, Figure 2.2 shows the size distributions for each of the 4 examined samples by LNS, DLS, and SEM analysis. SEM images are included for reference; particles deposit onto one another during the collection process and hence a large number of primary particles is present in each image. Monodisperse silica size standards have been examined via differential mobility analysis previously, showing excellent agreement between SEM inferred diameters and mode diameters via differential mobility analysis (Kimoto et al., 2017), hence the strong agreement between LNS size distributions and SEM size distributions (which are first taken as a percentage in predefined size bins, and then normalized by the natural logarithm bin width, comparable to LNS measurements) is not surprising. However, noteworthy is the disagreement between LNS and DLS measurements in terms of both mode diameter (or GMD) and GSD. For example, for the DP7560 sample, the GMDs are 61.8 nm, 71.1 nm, and 55.0 nm for LNS, DLS, and SEM respectively, with GSDs of 1.12, 1.26, and 1.19 for the same measurement systems. In general, we find DLS size distributions are skewed towards larger particle sizes, and more broadly distributed than either the LNS or SEM measurements, consistent with the observations of Jang et al. (2016). Furthermore, the LNS facilitates detection and characterization of multimodal distributions, which are not detected in DLS and which require a large number of particles to be manually analyzed for proper detection in SEM

images. For example, for the DP7560 and DP7590 samples, the LNS detects two non-dominant modes and a main mode at 60.4 nm and 103.7 nm respectively while DLS detects a single mode for each sample. The first mode size of each sample (19.1 nm for the DP7560 and 37.9 nm for the DP7590) by LNS was confirmed as actual particles by SEM analysis. The second mode within each sample a phantom caused by doubly charged particles. This can be determined as the mobility of this mode is half that of the dominant mode. This is further indicated by the absence of real particles in these size ranges within SEM analysis. In addition, for 50ZKDI LNS clearly has a trimodal distribution, while DLS shows a unimodal distribution, and SEM image shows a bimodal distribution where the two peaks agree reasonably well in size with the smaller two peaks in the LNS distribution. The larger LNS peak is presumably due to agglomeration of particles considering the fact that the ratio of the mobility diameter of larger peak to the mobility diameter of second peak is 1.29 which is in the range of the estimated mobility equivalent diameter of a dimer (Cho et al., 2007). however, this is likely agglomeration in the slurry sample itself. As shown in Figure 2.3, adjustments to dilution ratio (increasing by a factor of 10^2) in LNS measurements did not change the size of this peak.

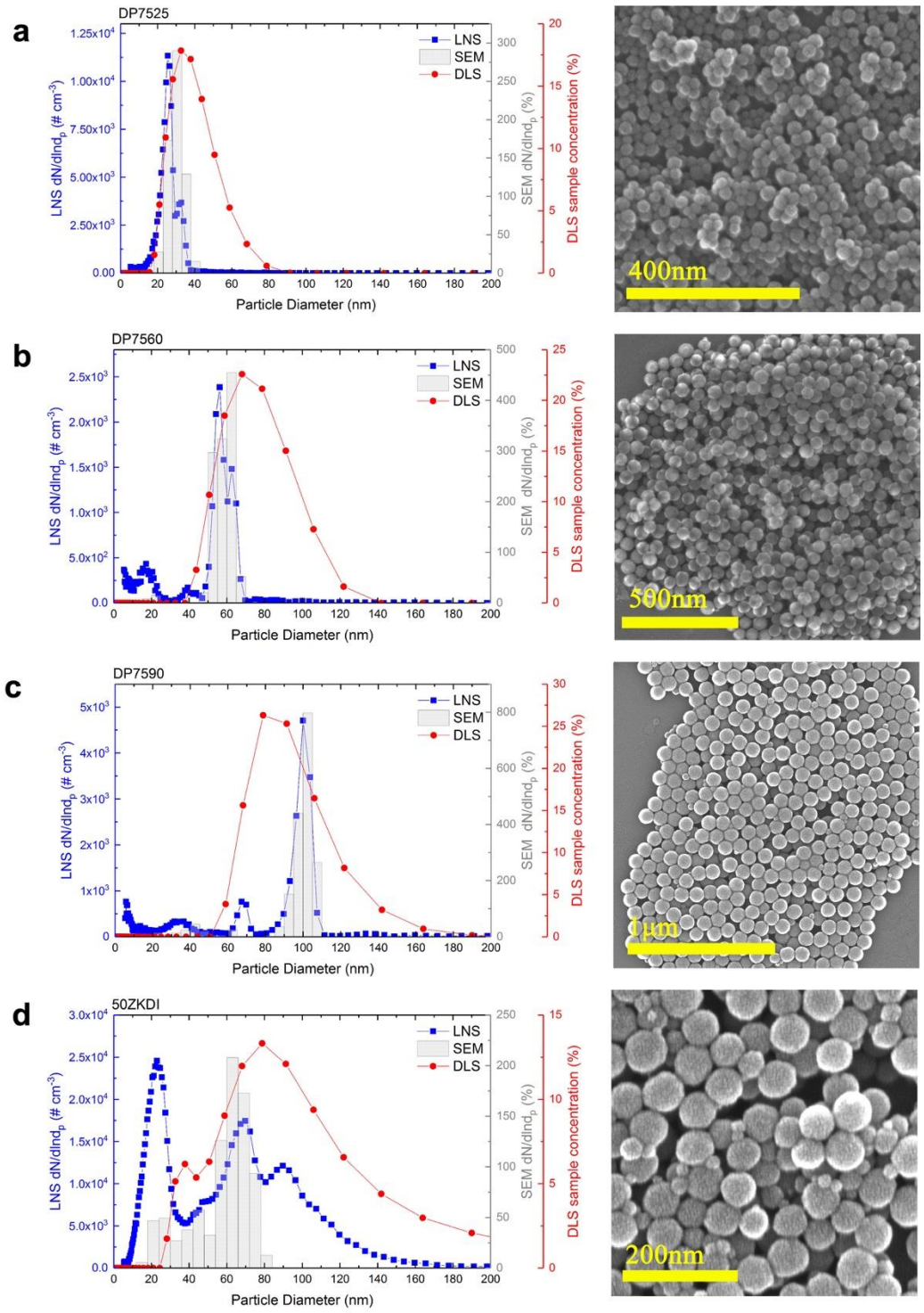

Figure 2.2 Size distributions of silica (SiO2) samples **(a)** DP7525, **(b)** DP7560, **(c)** DP7590, and **(d)** 50ZKDI by LNS (differential mobility analyzer), DLS, and SEM, respectively. SEM images are also displayed for collected particles from each sample.

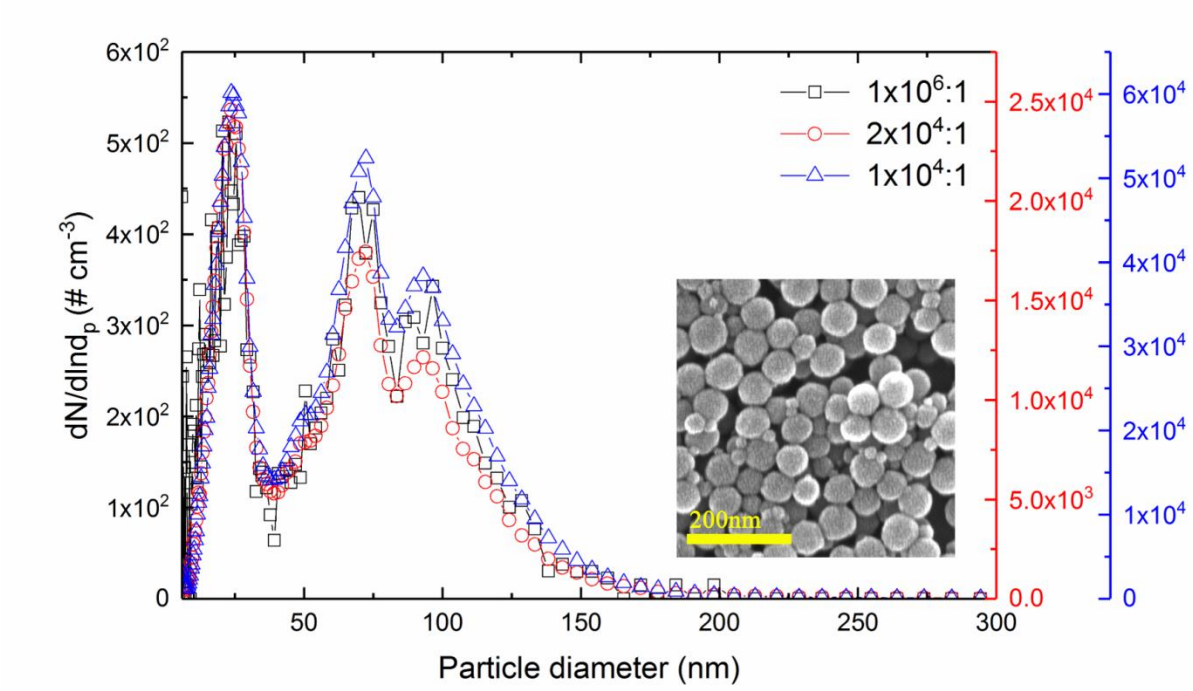

Figure 2.3 The size distribution of 50ZKDI at different dilution ratios and an SEM image of the particles. The dilution ratio in the legend is the product of the online dilution ratio and the offline dilution ratio.

To confirm the LNS ability to characterize multimodal distributions, we analyzed an intentionally mixed sample of DP7525, DP7560 and DP7590 by LNS and DLS. To prepare this sample, we mixed a 1:1000 dilution of DP 7525, a 4:1000 dilution of DP7560, and a 9:1000 dilution of DP7590. This mixture was diluted online by a factor of 2000 for LNS measurement and used as prepared for DLS. Evident in Figure 2.4, the LNS sample is able to accurately identify all three original distributions, with a fourth smaller mode below 10 nm arising from NVR (and hence excluded). Meanwhile, the DLS measurement again yields a single peak bridging the larger two particle modes, which is not an accurate characterization of this samples size distribution. This is consistent with the findings of Jeon et al. (2016c), who examined multimodal gold nanoparticle suspensions with sub- 30 nm particles via LNS and nanoparticle tracking analysis, showing that the gas phase

measurement approach was uniquely successful in identifying bimodal distributions and in correctly identifying mode sizes.

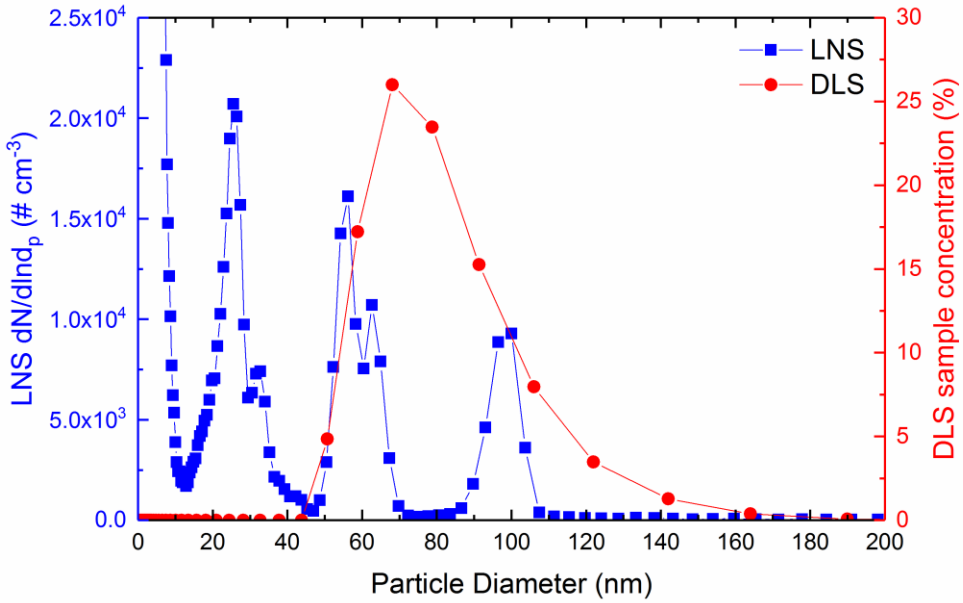

Figure 2.4 The size distribution of a mixture of 3 silica samples (DP7525, DP7560 and DP7590) as determined by LNS and DLS.

Overall, silica slurry sample characterization suggests that the LNS is able to more accurately characterize slurry size distributions than DLS in terms of mode diameter, distribution span (characterized by the geometric standard deviation), and in instances where distributions are multimodal. However, when analyzing slurry samples made of alternative material to silica and with clearly non-spherical particles, LNS and DLS measurements appear to become more complimentary to one another in describing the sample.

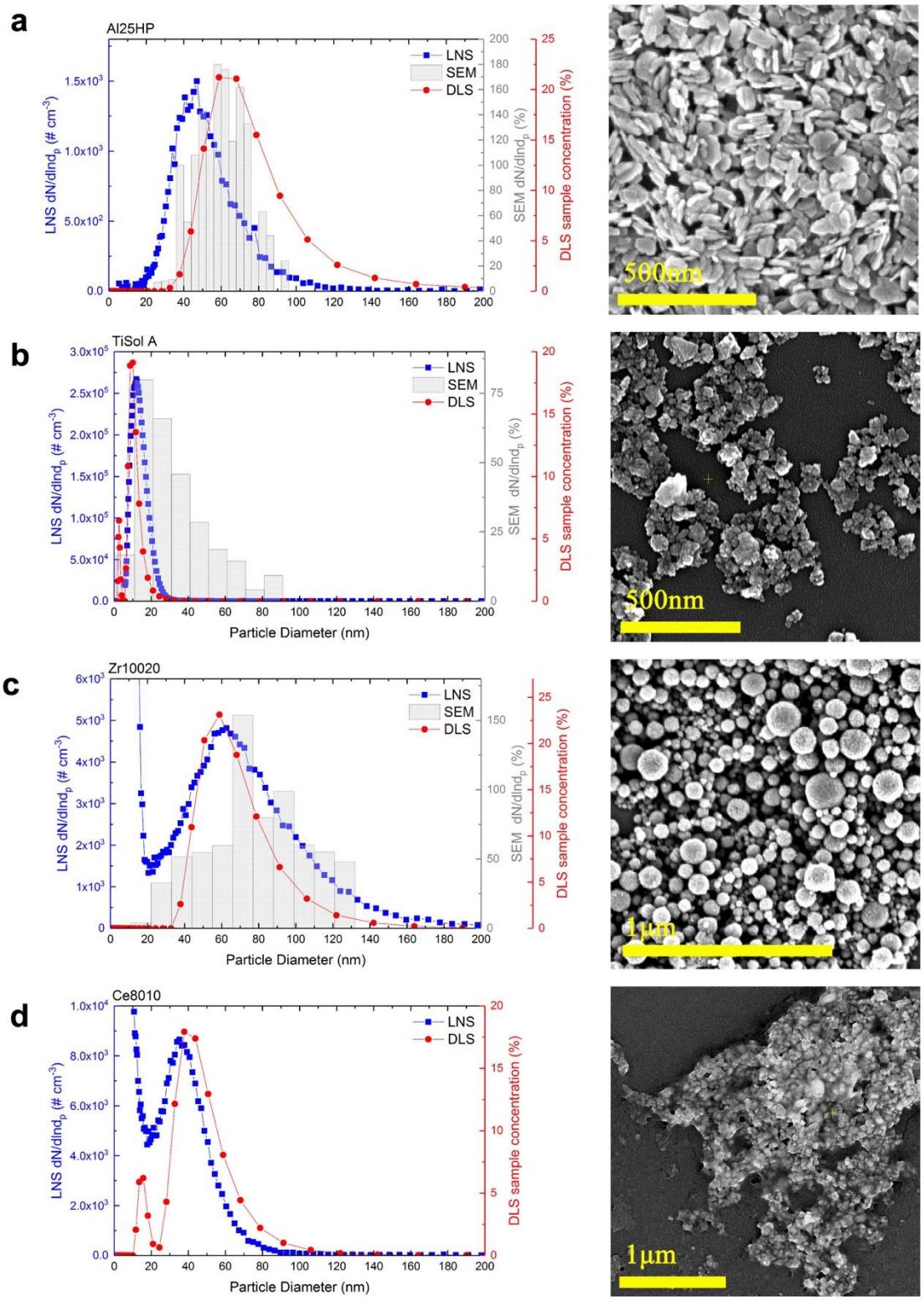

Figure 2.5 Size distributions of **(a)** alumina (Al_2O_3), **(b)** titania (TiO_2), **(c)** zirconia (ZrO_2), and **(d)** ceria (CeO_2) samples by LNS, DLS, and SEM. SEM images are also displayed for collected particles from each sample.

Figure 2.5 displays the size distributions of alumina, titania, zirconia, and ceria by LNS, DLS, and SEM measurements, respectively, including corresponding SEM images. Consistent with prior examinations of alumina CMP slurries, (Zhang et al., 2010, Krause et al., 2018) alumina slurry particles are found to be irregularly shaped and disk-like in structure, hence their diameters in SEM images were equated with projected-area equivalent diameters. The GMDs by LNS, DLS, and SEM analysis are 47.2 nm, 68.5 nm, and 55.6nm, respectively, and for alumina, neither LNS nor DLS distributions are in strong agreement with SEM analysis. While the precise reason for this discrepancy is not clear, a possible reason for the disagreement between LNS and SEM measurements is that the orientations of particles in SEM images are distinct from the average orientations during mobility measurements. For example, depending on its orientation, the projected-area equivalent diameter varied from 42 nm to 68 nm when we examined at two particles having at least one identical dimension. Conversely, disagreement between LNS and DLS measurements may arise because differential mobility analyzer measurements yield a transition regime mobility diameter (which depends upon both the projected area and hydrodynamic diameter; Gopalakrishnan et al., 2015b, Carbone and Larriba-Andaluz, 2021), while DLS measurements yield solely a hydrodynamic diameter. In general, the projected area equivalent diameter is smaller than the hydrodynamic diameter (Gopalakrishnan et al., 2011). However, for these two arguments to both hold simultaneously valid, the improved agreement between SEM and DLS over SEM and LNS would simply be a fortuitous coincidence.

The SEM image of titania particles displays irregular and aggregated particles. Difficulties in utilizing SEM for size distribution characterization of non-spherical particles

is highlighted in the intercomparison of size distributions for the titania sample shown in Figure 2.5b. The GMDs by LNS, DLS, and SEM are 12.4 nm and 10.3 nm and 19.3 nm, respectively. The size distribution by SEM analysis suggests that there are particles larger than 30 nm, but such particles are detected by neither LNS nor DLS. This discrepancy occurred because the primary particles of the titania sample cannot be clearly differentiated in the SEM image, suggesting that deposition of particles onto one another yields nearly indiscernible aggregates. Furthermore, as SEM data analysis relies on manual counting, the accuracy can be affected by the quality of the SEM images. This example serves as evidence that even SEM analysis cannot guarantee absolute accuracy of slurry particle size distributions.

For zirconia particles and ceria particles the LNS reveals an NVR peak below 10 nm, but the slurry particle distribution is still clearly evident. For zirconia, the GMDs by LNS, DLS, and SEM are 57.4 nm and 62.2 nm and 61.5 nm, respectively, with DLS showing a narrower distribution than LNS. For ceria particles, similar to titania, individual particles are not discernable in SEM, but to the point that it was not feasible to attempt recovery of the size distribution from SEM analysis. The ceria GMDs by LNS and DLS are 36.2 nm and 44.1 nm. Overall, for titania, zirconia, and ceria, we find modest, but reasonable agreement between LNS and DLS measurements, suggesting that both are presumably equally useful in CMP slurry size distribution measurements. We hence suggest that improved size distribution monitoring for such non-spherical particles would make use of both systems. This would allow for subtler changes in size distributions to be detected, e.g. a shift in the ratio of GMD or GSD as determined by LNS and DLS may

suggest small changes to the particle physical properties and ultimately changes in the performance of the CMP slurry that might not be clear using a single measurement method.

2.4.2 LNS System Characterization

While advocating for the examination of slurry particles by the combined implementation of LNS and DLS, here we also discuss the system capabilities of LNS, as its use is much less widespread than DLS. In many ways, LNS system application resembles to application of electrosprays with mass spectrometry (Davidson et al., 2017, Hogan and Biswas, 2008a) or ion mobility spectrometry/differential mobility analysis (Li et al., 2011, Li et al., 2020a, Hogan and Fernandez de la Mora, 2011) to introduce analytes into the gas phase for measurement; it is necessary to maintain the size and shape of the analytes during the hydrosol-to-aerosol transition. To assess aerosolization-induced agglomeration potential, we present a simulation approach, building upon Monte Carlo models utilized previously (Jeon et al., 2016c, Hogan Jr and Biswas, 2008) for a similar purpose. In a simulation, individual droplet diameters are sampled from a lognormal distribution function with input GMD and GSD values. The number of analyte particles in a droplet is then determined from a Poisson distribution with the average frequency λ calculated from equation (Lewis et al., 1994):

$$\lambda = \frac{\pi}{6} d_D^3 N_{sol} \tag{2.3}$$

where d_D is droplet diameter and N_{sol} is the colloidal concentration within the liquid sample. Constituent particle diameters are sampled from a lognormal distribution by preassigned GMD and GSD obtained from SEM analysis for the material in question. When more than 1 primary particle is present within a droplet, forming an agglomerate, a

volume equivalent diameter is then calculated for the aerosol particle, with additional volume added to account for non-volatile residue (at a prescribed volume fraction). Droplets containing no particles are considered as NVR and their resulting diameters are determined by preassigned non-volatile solute volume fraction and the sampled droplet diameter. We made a comparison between simulated size distributions and a measured size distribution of DP7590. For the purpose of the study, preassigned values are as follows: hydrosol concentration of 6.24×10^{15} # mL^{-1}, non-volatile solute concentration of 784 ppmv, droplet distribution GSD of 1.8, dilution factor varied from 10^3:1 to 10^6:1, and the droplet diameter GMD in the range of 0.5 μm to 5 μm. For particle size distributions, the local GMD and GSD of the main mode of DP7590 from SEM analysis were used; the values were 100 nm and 1.05, respectively. For comparison we also utilized a GSD of 1.20 with all other parameters held fixed. During investigation of dilution ratio, the GMD of droplets was held constant at 0.5 μm. Conversely, to examine varying droplet GMDs, the sampling process was repeated at a 10^6:1 dilution factor and the resulting particle diameters were counted into 2.5 nm bins to construct a normalized size distribution, $\frac{dN}{dlnd_p}$.

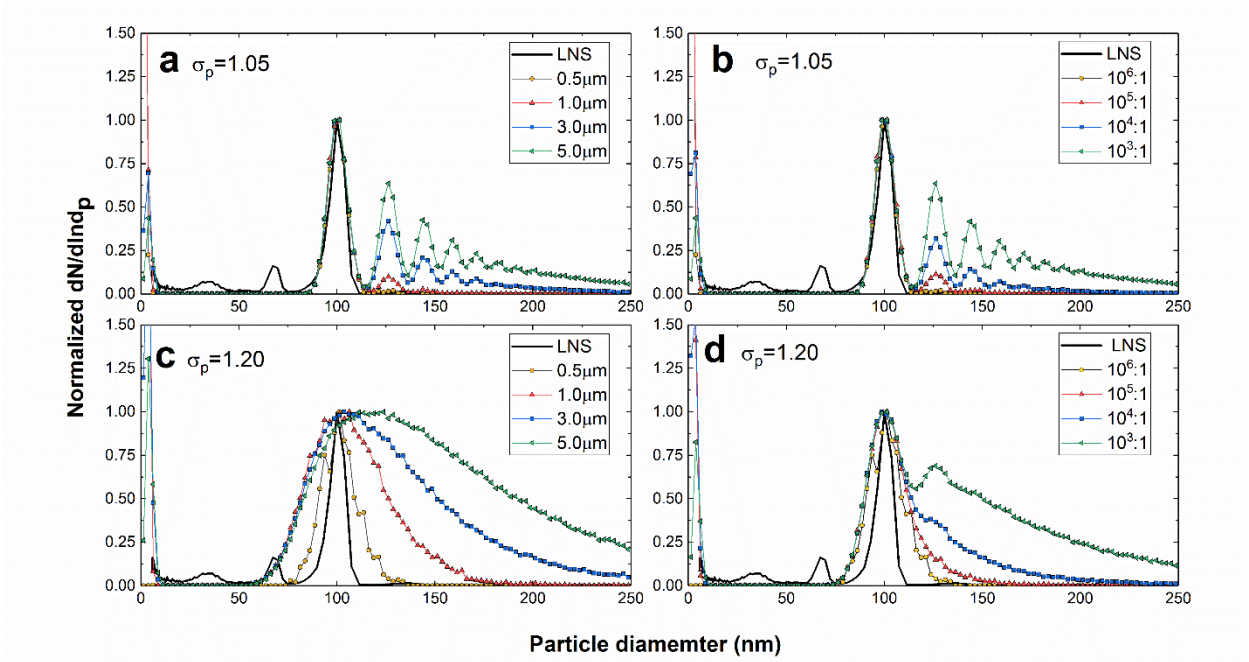

Figure 2.6 The simulated size distribution of DP7590 sample **(a)** at different droplet diameters and fixed dilution of 10^6:1 and **(b)** at different dilution ratios with a droplet geometric mean diameter of 0.5 μm. **(c)** and **(d)** display analogous plots in (a) and (b), but with the particle geometric standard deviation artificially inflated to 1.20. The measured size distribution by LNS is added for reference in all plots. The size distributions were normalized by the maximum value present above 10nm.

Figure 2.6a shows the expected size distributions with varying GMDs for the droplets against the measured size distribution in this study. We note that the LNS measurement contains two smaller modes of particles, which were not input into simulations and are hence disregarded in comparison. As expected, simulated larger droplet diameters increase the formation of agglomerates, magnify the effect of non-volatile residue, and broaden the distribution, even at a high dilution factor. Figure 2.6b shows the expected size distributions at different dilution ratios in comparison to the measured size distribution. At the lowest dilution factor, a secondary peak due to agglomerates is observed. By increasing the dilution factor, the number of larger agglomerate particles decreases, indicating a reduction in agglomeration. Again, this is an

expected behavior and further emphasizes the importance of droplet size and dilution factor on distribution fidelity. Compared to modeled size distributions, the actual distribution measured by LNS is narrower than smallest modeled droplet size and highest dilution factor. This indicates that LNS yields accurate size distribution of colloidal samples here and does so by generating small droplets and utilization of online dilution modules in the NPN. For comparison, Figures 2.6c and 2.6d display analogous results to Figure 2.6a and 2.6b, respectively. While the particle geometric standard deviation was artificially larger than in experiments, simulations reveal that with a higher GSD, using smaller droplets and larger dilution factors becomes even more important and size distributions become noticeable broader in these instances wherein dilution is insufficient.

Additionally, measured distribution repeatability was examined for both LNS and DLS. Figure 2.7 displays the distributions of 5 replicates of 3 samples (DP7590, Zr10020, CE8010) by both techniques. For all 3 samples, the distributions by LNS are consistent across each of the 5 replicates and no peak shift is observed. In contrast, the DLS replicates are inconsistent. The peak diameters of Zr10020 shifts from 50.7 to 68.1 nm and those of Ce8010 move from 15.7 to 43.8 nm. The clearer repeatability of the LNS measurements in comparison to DLS is attributable to the data inversion approach applied in both techniques. Because LNS utilizes a single particle sensitive CPC and mobility measurements in specific channels, measurements for different size particles are largely uncorrelated (with the exception of instances with multiply charged particles). Therefore, variations in large particle concentrations do not affect the distribution near the peak in LNS. Conversely, DLS does not enable independent measurements of particle

concentrations in different size channels and variability across the distribution measurement can affect the entire distribution.(Nickel et al., 2014)

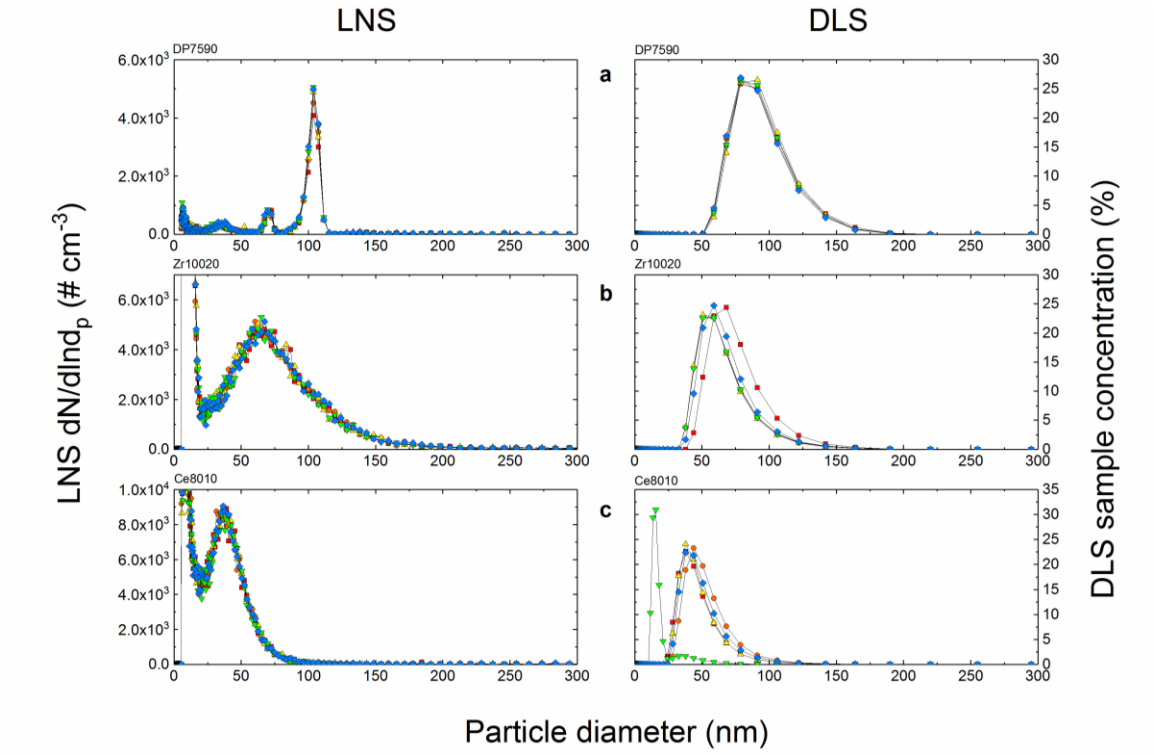

Figure 2.7 The size distributions of repeated measurements for **(a)** silica DP7590, **(b)** zirconia Zr10020, and **(c)** ceria CE8010 by LNS and DLS.

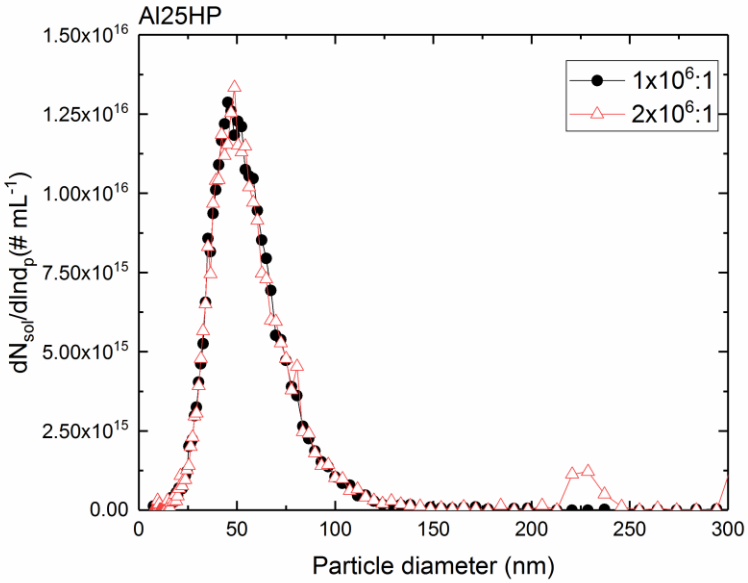

Figure 2.8 The slurry size distribution of Al25HP inferred using volume standard measurements for two different LNS dilution ratios.

Finally, measured distributions by LNS were utilized to calculate slurry sample original concentration, highlighting a key feature of LNS measurement. Figure 2.8 shows the slurry sample number distribution of Al_2O_3 as inverted by LNS. The aerosol size distribution was inverted to the hydrosol size distribution using equation (2.2). The agreement for different dilution ratios observed highlights that LNS results where a volume standard has been measured a priori can be used to estimate the actual colloidal sample concentration and size distribution. Importantly, the volume standard measured at each dilution factor employed helps to correct for any changes in the aerosolization process at different dilution factors. Accurate implementation of this analysis could greatly enhance the examination and quantification of slurry particle size distributions.

2.5 Conclusions

We examined the size distributions of 8 different CMP slurry particle types using DLS and LNS (an air-jet atomizer-DMA-CPC system), using SEM imaging as a reference for measurements. For silica slurry particles, LNS measurement was shown to produce repeatable distributions well matched to SEM inferred distributions, and was able to accurately identify multimodal distributions. In contrast, DLS was unable to identify multimodal size distributions, and measured distributions tended to drift between repeated trials. More irregularly shaped materials proved more difficult to characterize via both DLS and LNS measurement, but because both measurement techniques yield size distributions, we suggest that for broadly distributed, irregularly shaped CMP particles, regular use of both measurements in characterization would enable improved process control. In addition to intercomparison of measurement techniques, we analyzed LNS system characteristics that can contribute to comprehensive examination of slurry particles. The hydrosol-to-aerosol conversion process was simulated and compared to measured LNS distributions. Modeling indicated that LNS is able to prevent distribution distortions due to particle agglomeration by controlling the droplet size and utilizing online dilution. LNS was also utilized to estimate hydrosol concentration from aerosol concentration. This calculation is as yet imperfect due to the limitations of the transfer function used during the data inversion process, but nonetheless does demonstrate the promising LNS capability to directly quantify size distributions in the liquid phase.

Chapter 3. Condensable Vapor Sorption by Low Charge State Protein Ions

Adapted from: Jihyeon Lee, Brian H. Clowers, & Christopher J. Hogan Jr, Condensable Vapor Sorption by Low Charge State Protein Ions. Submitted to Analytical Chemistry.

ABSTRACT: Measurement of gas-phase ion mobility of protein ions provides a means to quantitatively assess the relative sizes of charged proteins. However, protein ion mobility measurements are typical singular values. Here we apply tandem mobility analysis to low charge state protein ions (+1 and +2 ions) introduced into the gas phase by nanodroplet nebulization. We first determine protein ion mobilities in dry air, and subsequently examine shifts in mobilities brought about by the clustering of vapor molecules. Tandem mobility analysis yields mobility-vapor concentration curves for each protein ion, expanding the information obtained from mobility analysis. This experimental procedure and analysis is extended to bovine serum albumin, transferrin, immunoglobulin G, and apoferritin with water, 1-butanol, and nonane. We find that all protein ions adsorb vapor molecules, with mobility "diameter" shifts of up to 6-7% at conditions just below vapor saturation. We parameterize results using κ- Köhler theory, where the term κ quantifies the extent of uptake beyond Köhler model expectations. For 1-butanol and nonane, κ decreases with increasing protein ion size, while it increases with increasing protein ion size for water. For the systems probed, the extent of vapor uptake for the organic vapors is unaffected by the nebulized solution pH, while water uptake is sensitive to pH.

3.1 Introduction

Ion mobility spectrometry (IMS; Revercomb and Mason, 1975b), either as a standalone technique or in conjunction with mass spectrometry, (Bohrer et al., 2008) facilitates characterization of the structures of protein ions; measured mobilities can be converted either to collision cross sections via the foundational relationships first noted by Langevin (i.e. Mason-Schamp equation; McDaniel and Mason, 1973) or to mobility diameters via the Stokes-Millikan equation. (Larriba et al., 2011a, Larriba-Andaluz and Carbone, 2021) A number of IMS studies in the past two decades have shown that structural features for a number of proteins and protein multimers are maintained when charged species transition from the solution to the gas-phase (Ruotolo et al., 2005, Ruotolo and Robinson, 2006) establishing the use of IMS as an essential characterization tool for protein structural biology. (Ruotolo et al., 2008, Ben-Nissan and Sharon, 2018) However, a major limitation of the standard, low-field strength IMS experiment is that for a given ion (chemical composition and charge state), the measurement yields a single mobility value which is largely dependent on three features of the ion: (1) the ion overall "size", often scaling with molecular mass for protein ions; (Bush et al., 2010) (2) the ion charge state, not only because mobility is proportional to charge but because high levels of charge lead to Coulombic stretching in protein and macromolecular ions; (Larriba and Fernandez de la Mora, 2012, González Flórez et al., 2016, Abramsson et al., 2021) and (3) the polarizability of bath gas in which the measurement is made. (Naylor et al., 2020, Asbury and Hill, 2000) This limits IMS largely to global size characterization, as separation is predominantly dependent on overall protein ion properties, namely, size and charge.

In field asymmetric waveform IMS and other variants of IMS where separation is not based purely upon mobility, but instead upon differences in low field and high field mobilities for an ion, limitations in chemical selectivity have been overcome by introducing condensable vapor molecules alongside the IMS bath gas (Waraksa et al., 2016, Rorrer and Yost, 2011, Schneider et al., 2013, Purves et al., 2014, Kafle et al., 2014, Rorrer and Yost, 2015; i.e. vapor molecules of compounds which would be in the liquid or solid state at the measurement conditions, hence the vapor molecules only comprise a small fraction of the bath gas). At these sub-saturated concentrations, condensable vapor molecules transiently and selectively bind to analyte ions. For low mass analytes in traditional low-field IMS measurements, theories describing the transient binding of condensable species have also been developed (Maisser and Hogan, 2017, Thomas et al., 2016, Kwantwi-Barima et al., 2017, Li and Hogan, 2017, Oberreit et al., 2015, Rawat et al., 2015, Ahonen et al., 2019, Kwantwi-Barima et al., 2019, Kwantwi-Barima et al., 2020) and compared to measurements; both theory and measurements show that the transient binding of condensable vapors shift experimental mobilities to smaller values. (Fernandez Maestre, 2017, Fernández-Maestre et al., 2016) Most importantly, the extent of the observed shift is dependent upon the binding free energy of the vapor to the ion and the vapor molecule size relative to the ion size. Several studies have also demonstrated that the presence of condensable organic vapor molecules in the bath gas during IMS measurements of protein ions (primarily cytochrome C as a model protein) yields shifts in ion mobilities which can be attributed to condensable vapor transient binding (Meyer et al., 2016, Butcher et al., 2019). However, these prior efforts focused largely on highly charged protein ions (i.e. the +7 charge state of cytochrome C or higher). Ignoring the impacts of solution ionization

conditions, sufficiently highly charged protein ions are Coulombically stretched in the gas phase and in examining mobility shifts due to vapor clustering for highly charged protein ions, vapor binding may simultaneously alter the extent of Coulombic stretching and the ion size, complicating the interpretation of results.

Here, we examine protein ion mobility shifts due to uptake of water, 1-butanol, and nonane at vapor concentrations up to saturation. As model systems we used bovine serum albumin (66kDa; Hirayama et al., 1990), transferrin (79.5kDa; Roberts et al., 1966), immunoglobulin G (150kDa; Lambin, 1978), and apoferritin (444kDa; Harrison, 1977), with measurements in air at atmospheric pressure and 295 K. These measurement conditions not only enable assessment of protein ion specific levels of vapor uptake, but in the case of water are also relevant to conditions downstream of commonly employed electrospray ionization sources for protein ions. Measurements were carried out via tandem differential mobility analysis (TDMA; Rader and McMurry, 1986, Park et al., 2008, Hämeri et al., 2000), an approach commonly used to examine vapor uptake and the hygroscopic behavior of aerosol nanoparticles. (Biskos et al., 2006) Unique from prior vapor uptake assessments for protein ions, protein ions were generated using a nanodroplet nebulizer (Jeon et al., 2016c, Jeon et al., 2016b, Jeon et al., 2016a, Lee et al., 2022) and atmospheric pressure chemical ionization, *in lieu* of an electrospray emitter, to produce only singly and doubly charged protein ions. This approach reduces Coulombic stretching for the protein ions examined. We quantify the extent of vapor uptake by evaluating experimental trends in vapor with κ- Köhler theory, (Petters and Kreidenweis, 2007, Chang et al., 2010) which is commonly used to describe the potential for water uptake and cloud condensation nucleus activity in aerosols.

3.2 Experimental Methods

Bovine serum albumin (A9647), transferrin (human, T8158), immunoglobulin G (human, 56834), and apoferritin (horse spleen, A3641) were purchased from Sigma Aldrich in powder form. 10-30 micrograms per milliliter of each protein were dissolved into ultra-pure water (UPW system, Smith Engineering, Inc.) and then diluted with UPW again dilution ratios from 23.3 – 140 prior to aerosolization and TDMA measurements (adjusted to ensure monomer proteins were detected in high abundance). To adjust pH levels, ammonium hydroxide solution (Arcros Organics) and formic acid solution (Honeywell) were added to the sample, and pH levels were confirmed by pH testing strips before measurements.

The mobility-based size distributions of protein ions were first measured in a manner similar to that described by a number of prior studies, (Kaufman et al., 1996, Bacher et al., 2001, Kaddis et al., 2007, Maiβer et al., 2011) i.e. using a single differential mobility analyzer (DMA; Knutson and Whitby, 1975b) coupled to a condensation particle counter (CPC; Stolzenburg and McMurry, 1991). A schematic diagram of the specific system employed for mobility-based size distributions is shown in Figure 3.1a and Figure 3.1b provides a schematic diagram of the system used for TDMA vapor uptake experiments. Traditionally DMA-CPC measurements of protein ions are performed using a charge reduction electrospray source (Scalf et al., 1999, Scalf et al., 2000, Tamadate et al., 2020) to introduce singly and doubly charged protein ions into the gas phase. Here, a nanoaerosol generator (NAG, Kanomax FMT), which is a nebulizer designed to produce submicrometer droplets, (Jeon et al., 2016c, Jeon et al., 2016b, Jeon et al., 2016a, Lee et al., 2022) was instead employed to aerosolize proteins into the gas phase. In the NAG, the prepared

sample solution of proteins was introduced to a pneumatic nebulizer, held at 35 psi backing pressure, with the solution dispersed into droplets at a liquid flow rate less than 1.0 mL min^{-1} (though varied for different proteins). After evaporation of the droplets, facilitated by passing them through an evaporator at 80 °C, solvent-free proteins were carried out of the NAG with a clean gas flow of 1.0 L min^{-1}. A diffusion dryer installed downstream of the NAG further reduced humidity down to ~10%, measured previously using a chilled-mirror hygrometer (General eastern, Hygro M4). The gas phase proteins are largely neutral in charge upon generation via the NAG. They were hence ionized by a Kr-85 radioactive source emitting beta rays which ionize gas molecules bipolarly. (Maisser et al., 2015) Passage of proteins through such radioactive sources facilitates their interaction with smaller mass ions. Through ion-protein collisions and subsequent charge transfer from ions to proteins, protein ions are generated. However, a distribution of charge states exists, wherein the majority of proteins are still neutral, but a detectable fraction is singly or doubly charged across both polarities (i.e. positively and negatively charged species). Although not directly measured for proteins, measurements for smaller polymer ions suggest the resulting species are ionized by protonation and deprotonated reactions. (Maisser et al., 2015) After ionization, protein ions were separated by a nano-differential mobility analyzer (nano-DMA, TSI) based upon their ion mobilities. For separation, the nano-DMA was operated with a circulating sheath flowrate of 6 L min^{-1}, with 0.6 L min^{-1} of the gas phase protein-laden flow entering the DMA. The DMA applied voltage was stepped from 0 to 150 V over 40 measurement points for all protein except apoferritin, where a voltage range from 0 to 300 V over 60 measurement points was applied.

To realize tandem ion mobility measurements the flow existing the first DMA was then transmitted into a second DMA, which was operated with a non-recirculating sheath flow of air, with its flow diagram shown in Figure 3.1c. The incoming sheath flow was clean air of 5.5 L min $^{-1}$, controlled by a mass flow controller. The clean air flow, along with and a volumetric flow of liquid (water, nonane, or 1-butanol) in the range of 50-200 μL min $^{-1}$ (liquid, controlled by a syringe pump) was supplied to a T-junction held at 50 °C. The liquid was introduced continuously as droplets by a fused silica capillary tubing with a 250 μm ID. For all liquids, the droplets rapidly evaporated in the heated T-junction, and vaporized molecules were then carried within the air flow into the second DMA. To validate this vapor introduction system, we measured dew points with the chilled-mirror hygrometer; the measured dew points agreed with the calculated dew points within $\pm$0.5 K. The variations of the resulting sheath flow rate due to the addition of vapor molecules are not negligible in such TDMA systems. Therefore, the flow was continuously monitored with laminar flow elements (i.e. via pressure drop measurements) both upstream and downstream of the DMA (sheath flow path). These measurements were used to adjust the mass flow controller rate of clean air to maintain the total sheath flow rate of 5.5 L min $^{-1}$ through the second DMA for all vapor introduction conditions. At the downstream of the DMA, after the laminar flow element, a second mass flow controller was connected to a vacuum source to maintain 5.5 L min $^{-1}$ sheath flow rate. Downstream of the T-junction, the temperature of the whole system was held at 22 °C (room temperature). With the first DMA operating at fixed voltage to select protein ions of a given charge state (singly or doubly charged and positively charged) and cluster number (typically monomers, but also dimers and trimers for bovine serum albumin), the mobility distributions of the selected

protein ions were first measured without vapor introduction in the second DMA to establish a baseline for vapor uptake comparison. The second DMA was operated by stepping the voltage in the range corresponding to ±20% of the mobility diameter of selected protein ions with 12-16 measurement stages. Downstream of the second DMA, transmitted protein ions were detected via a fast time response condensation particle counter (FCPC, Kanomax FMT; Liu et al., 2021). The vapor concentration was systematically varied in the second DMA sheath flow, with mobility distributions remeasured and compared to one another. In total, measurements were conducted for 4 different proteins, 3 different vapors, and 3 different pH levels over the course of 9 days. On each day, measurements were limited to one vapor type and one pH level to minimize system contamination and the effects of any day-to-day variation on flow and vapor concentrations. The second DMA was flushed with clean, dry, air continuously overnight between measurement days.

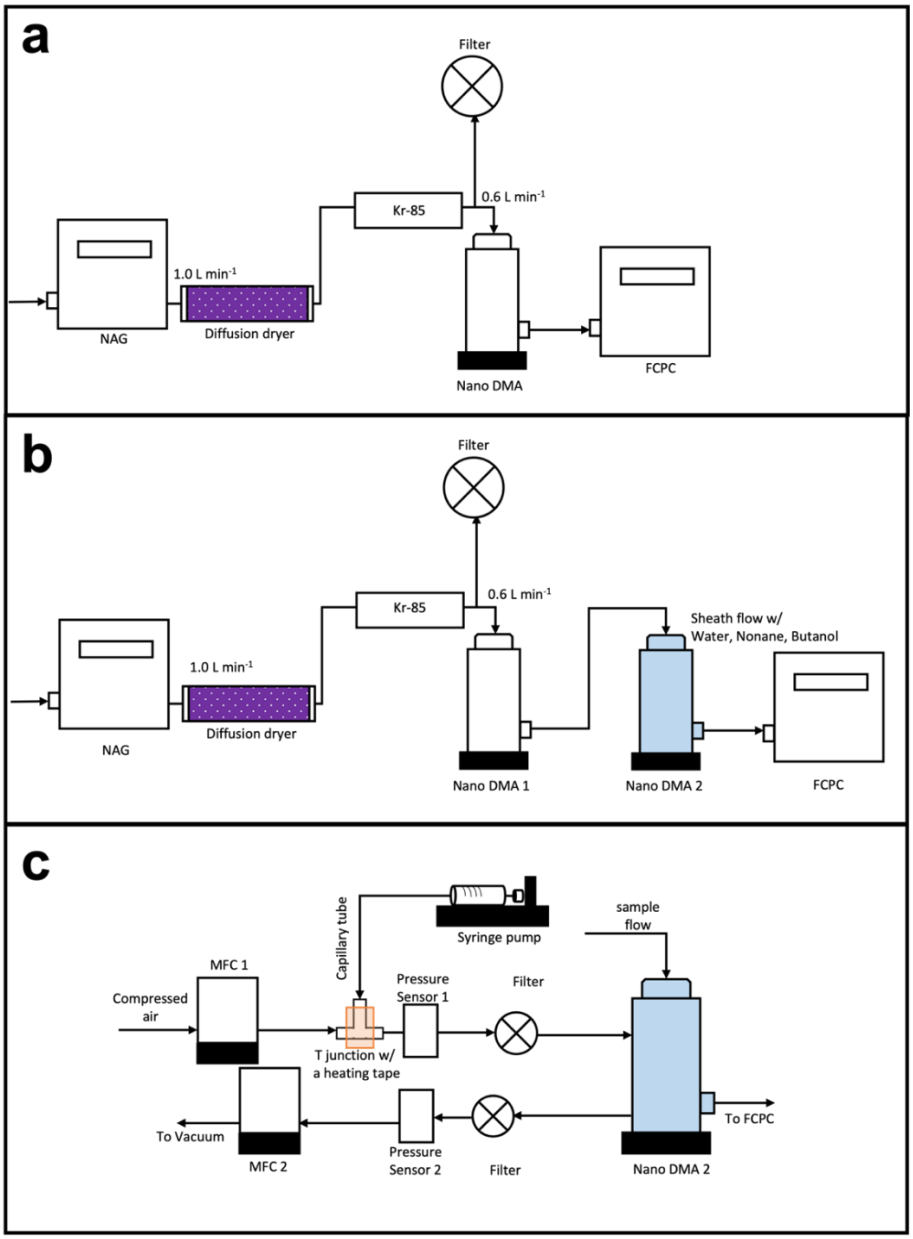

Figure 3.1 Schematic diagrams of the measurement systems utilized. **(a)** Single DMA-CPC system used for size distribution measurements of protein ions. **(b)** Tandem DMA measurement system for protein ions including vapor introduction at the second DMA. **(c)** The sheath flow control system of the second DMA with vapor introduction.

The data obtained from the measurements are the counts by FCPC, converted directly to a number concentration, as a function of DMA voltage. The voltage, V can be converted into the mobility, Z_p using geometries of the DMA by equation (3.1),

$$Z_p = \frac{q_{sh}}{2\pi VL} \ln\left(\frac{r_2}{r_1}\right) \quad (3.1)$$

where q_{sh} is sheath flow rate, L is the length of the DMA, r_1 is inner radius, and r_2 is outer radius. To convert ion mobility in the transition (Knudsen number dependent; Zhang et al., 2012a, Larriba-Andaluz and Carbone, 2021) regime to a measure of protein ion "size", we apply the Stokes-Millikan equation:

$$Z_p = \frac{neC_c}{3\pi\mu(d_p + d_g)} \quad (3.2)$$

where n is charge state, e is charge of electron, C_c is slip correction factor , μ is viscosity, d_p is the mobility diameter (i.e. the spherical equivalent diameter for the protein ion under the measurement conditions), and d_g is the effective gas molecule diameter (approximately 0.3 nm in air; Larriba et al., 2011a, Fernández-García and Fernández de la Mora, 2013). The slip correction factor is expressed as follows:(Davies, 1945b)

$$C_c = 1 + \frac{2\lambda}{(d_p + d_g)}\left(1.257 + 0.4e^{-0.55\frac{(d_p + d_g)}{\lambda}}\right) \quad (3.3)$$

where λ is mean free path of the gas. Mobility diameter spectra were used to compute a volume-weighted mean diameter ($\bar{d}_p$) at each vapor saturation ratio. We then calculated the growth factor by normalizing the volume-weighted mean diameter at each saturation ratio by the mean diameter without vapor introduction. Remark that this analysis approach is much simpler than that commonly used in inverting TDMA data (Gysel et al., 2009) wherein DMA transfer functions are accounted for and distributions in the extent of vapor uptake are determined. The simplified approach is employed here because (1) protein ions are single molecule ions, as opposed to the highly heterogeneous particles commonly examined via TDMA measurements, (2) the protein ion mobility distributions are arguably as narrow or more narrow than the transmission function of the DMA (You et al., 2014),

(3) as shown in the Results & Discussion section, vapor uptake does not appear to substantially broaden mobility distributions, as would be the case if the growth factor had a broad distribution. To parameterize results, we applied κ-Köhler theory to our data; based on κ-Köhler theory, the saturation ratio, S, over a droplet in equilibrium with its surroundings can be described as follows:(Petters and Kreidenweis, 2007)

$$S = a_w \exp\left(\frac{4\sigma M_w}{RT\rho \bar{d}_p}\right) \tag{3.4}$$

where a_w is the activity of the liquid in the droplet, σ is surface tension, M_w is molecular weight of the liquid, R is universal gas constant, T is temperature, ρ is density of the liquid. The parameter κ is determined from:

$$\frac{1}{a_w} = 1 + \kappa \frac{V_s}{V_w} \tag{3.5}$$

where V_s is the volume of the dry ion and V_w is the volume of liquid condensed. With the conversion from volumes to diameters, the saturation ratio can be expressed with κ as follows,

$$S = \frac{\bar{d}_p{}^3 - \bar{d}_{p,d}{}^3}{\bar{d}_p{}^3 - \bar{d}_{p,d}{}^3(1-\kappa)} \exp\left(\frac{4\sigma M_w}{RT\rho \bar{d}_p}\right) \tag{3.6a}$$

where $\bar{d}_p$ is the volume-weighted mobility diameter at the saturation ratio in question, and $\bar{d}_{p,d}$ is the volume weighted mobility diameter in the absence of condensable vapor. We found κ for each protein ion with each vapor type via a linear regression shown in figure 3.2. We rearranged equation (3.6a) as shown in (3.6b),

$$\frac{\bar{d}_p{}^3}{\exp\left(\frac{4\sigma M_w}{RT\rho \bar{d}_p}\right)} - \frac{\bar{d}_p{}^3 - \bar{d}_{p,d}{}^3}{\mathrm{S}} = \frac{\bar{d}_{p,d}{}^3(1-\kappa)}{\exp\left(\frac{4\sigma M_w}{RT\rho \bar{d}_p}\right)} \tag{3.6b}$$

and plotted $\frac{\bar{d}_{p,d}{}^3}{\exp\left(\frac{4\sigma M_w}{RT\rho\bar{d}_p}\right)}$ versus $\frac{\bar{d}_p{}^3}{\exp\left(\frac{4\sigma M_w}{RT\rho\bar{d}_p}\right)} - \frac{\bar{d}_p{}^3 - \bar{d}_{p,d}{}^3}{S}$ where $(1-\kappa)$ can be found as the slope of the line.

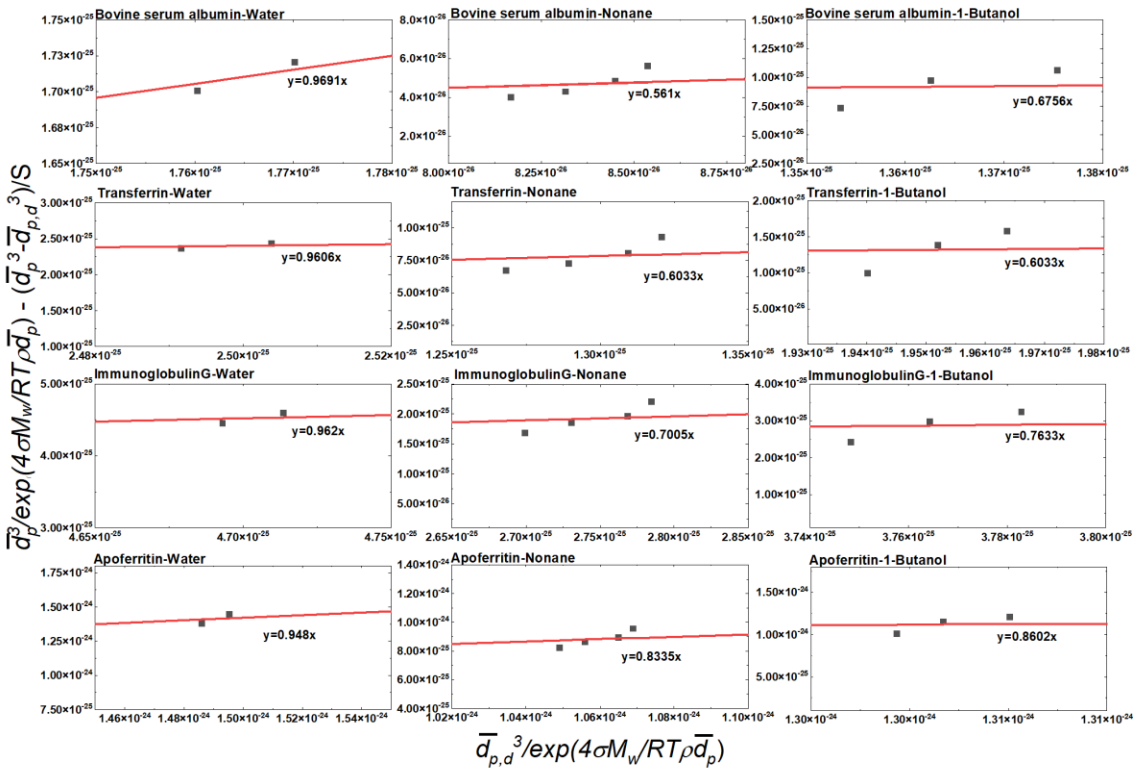

Figure 3.2 Regression plots used to infer the κ parameter for 4 proteins with water, nonane, and 1-butanol. The slope written in the figure is equal to $(1-\kappa)$.

3.3 Results and Discussion

Figure 3.3 displays the mobility diameter distributions of 4 protein ions, generated from pH 7 solution in the absence of condensable vapor. For each protein, the major peak corresponds to monomer ions except for bovine serum albumin, where the highest peak corresponds to dimer ions and the second highest peak corresponds to monomer ions. The mobility diameters of bovine serum albumin, transferrin, immunoglobulin G, and apoferritin were 6.2 nm, 7.0 nm, 8.2 nm and 12.0 nm respectively, in reasonable agreement

with original measurements of Kaufman et al. (1996) for bovine serum albumin (6.04 nm) and immunoglobulin G (8.13 nm). Measurements are further in good agreement with crystal structure measurements. Luzzati et al. (1961) observed the radius of gyration of 3.06 nm for bovine serum albumin at pH 5.3 using small angle X-ray scattering. Martel et al. (1980) investigated the structure of human transferrin with small angle neutron scattering and the radius of the gyration of transferrin is 3.025 nm. KILÁR et al. (1985) measured the radii of immunoglobulin G1 (6 nm) and G3 (4.9 nm) using small angle X-ray scattering. Fischbach and Anderegg investigated the structure of apoferritin using X-ray scattering and showed apoferritin has a hollow sphere with an outer radius of 6.1 nm. (Fischbach and Anderegg, 1965) Peaks corresponding to doubly charged monomers were also identified, as they have twice the mobility of singly charged monomers (leading to a smaller inferred mobility diameter with a singly charged assumption). The charge assignment of different peaks and cluster state (M: monomer, D: dimer, and T: Trimer) are labelled in the figure. Peaks corresponding to multimeric ions were also observed due to the possibility of that single droplet contains proteins more than one during the nebulization process within NAG. The simulation by Lee et al. (2022) suggest that similar mobility diameter distributions to figure 3.3 a-b are obtained when highly concentrated monodisperse particles are generated by a NAG. The bovine serum albumin and transferrin protein ions formed dimers and trimers concentrations approaching the monomer concentration. Overall, the NAG and atmospheric pressure chemical ionization approach appears to yield protein ions similar to that produced by charge reduction electrospray sources. (Bacher et al., 2001, Kaufman et al., 1996, Kaddis et al., 2007, Maiβer et al., 2011) Figures 3.4-3.7 display mobility diameter spectra (normalized) of the singly charged

monomers from pH 7 solutions, with the introduction of 3 different condensable vapors. The saturation ratio on a percent basis, at 295 K, is noted for each displayed spectrum. Prior to discussing results for each protein and vapor examined, we remark that in all instances, we observe an increase in mobility diameter (i.e. a decrease in ion mobility) in the presence of introduced condensable vapor. Detectable shifts with the modest resolving power (<10) mobility analyzers utilized in our measurements is indicative of vapor sorption (transiently, with vapor molecules adsorbing and desorbing from proteins as they traverse the DMA) during measurement. This can be contrasted with observed mobility shifts for higher charge state protein ions in the presence of condensable vapor molecules; for example Butcher et al. (2019), using higher resolution instrumentation, found that in the mobility distributions of higher charge state (+5 and higher) cytochrome C and myoglobin ions specific peaks appear upon introduction of vapor molecules, and such peaks do not always appear at smaller mobilities. As Coulombic stretching likely plays some role in protein ion structure, changes in the mobilities of higher charge state protein ions are presumably due to a combination of conformational changes and vapor sorption, while for singly charged ions, where there is no Coulombic repulsion, more pronounced mobility shifts observed here are most likely due to vapor uptake.

With water vapor, bovine serum albumin ions displayed minimal growth via vapor uptake; however, immunoglobulin G, and apoferritin grew much more noticeably. Conversely, with nonane and 1-butanol introduced as condensable vapors, all protein ions displayed clear size shifts, indicative of vapor uptake.

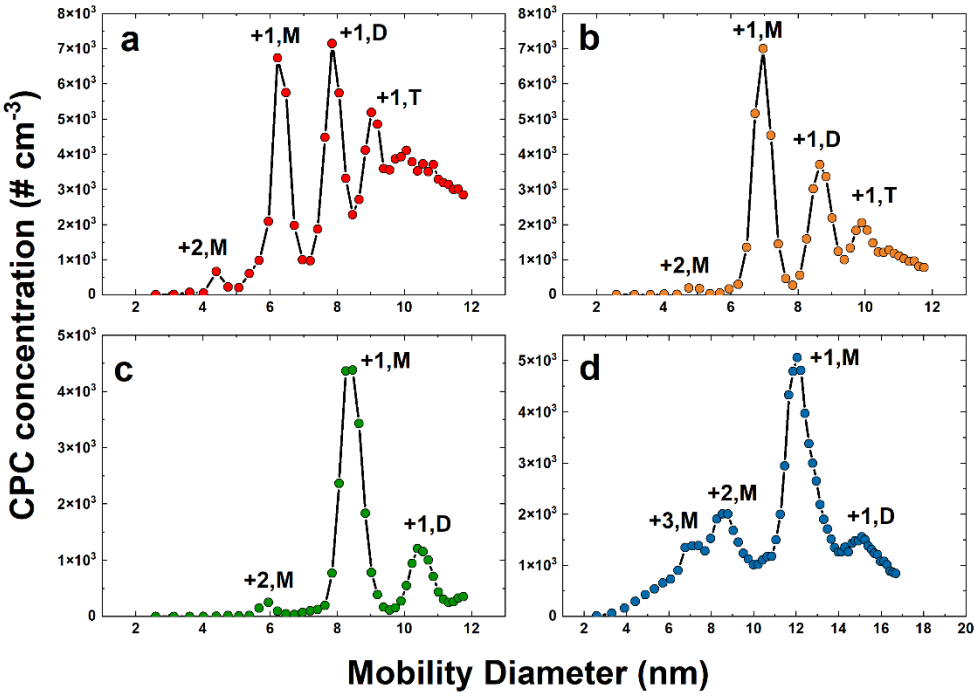

Figure 3.3 Mobility diameter distributions of all proteins in air nebulized at a pH of 7. **(a)** Bovine serum albumin. **(b)** Transferrin. **(c)** Immunoglobulin G. **(d)** Apoferritin. +1 and +2 indicate the charge state, while M, D, and T indicate monomers, dimers, and trimers respectively.

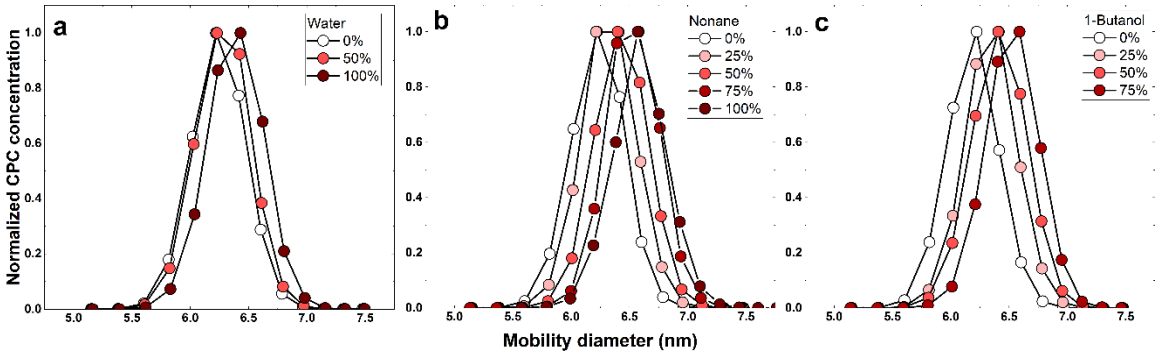

Figure 3.4 Mobility diameter distributions of singly charged bovine serum albumin monomers with **(a)** water introduction, **(b)** nonane introduction, and **(c)** 1-butanol introduction.

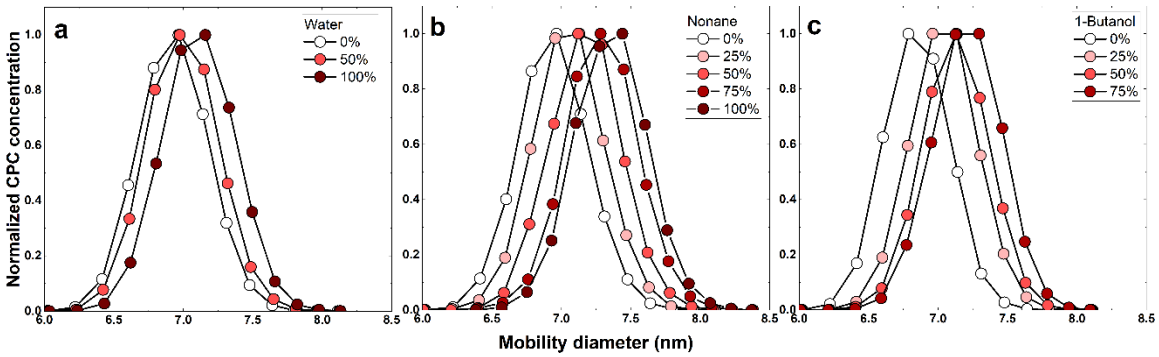

Figure 3.5 Mobility diameter distributions of singly charged transferrin monomers with **(a)** water introduction, **(b)** nonane introduction, and **(c)** 1-butanol introduction.

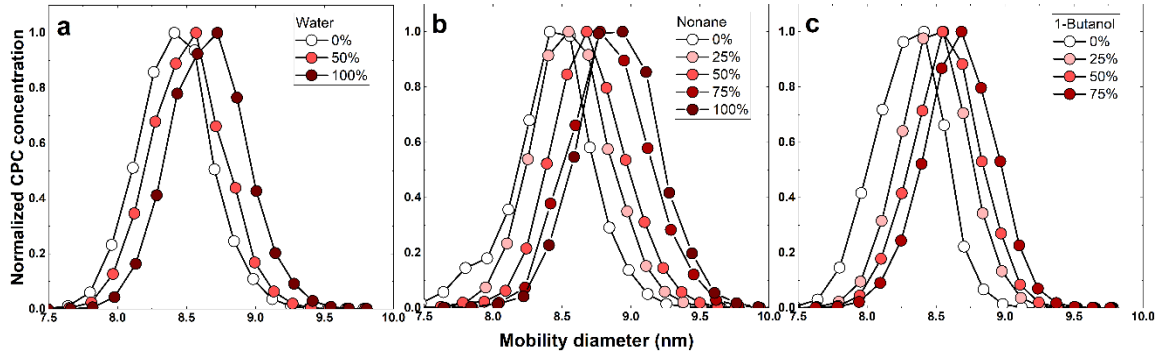

Figure 3.6 Mobility diameter distributions of singly charged immunoglobulin G monomers with **(a)** water vapor introduction, **(b)** nonane introduction, and **(c)** 1-butanol introduction.

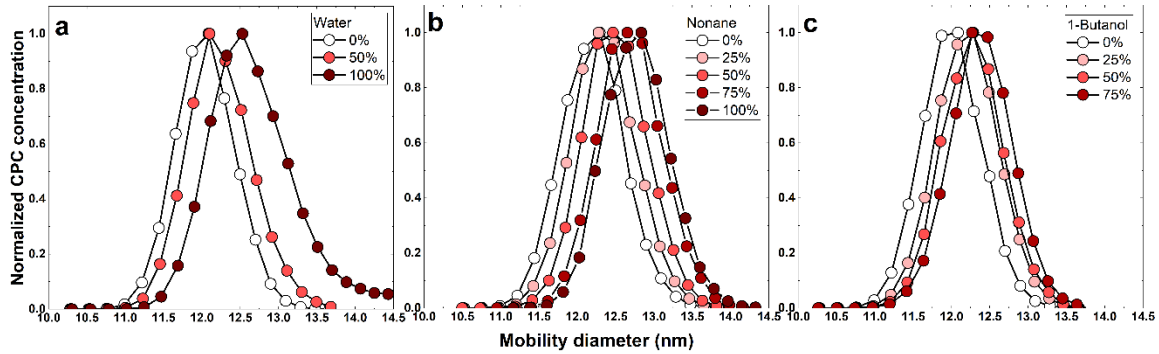

Figure 3.7 Mobility diameter distributions of singly charged apoferritin monomers with **(a)** water introduction, **(b)** nonane introduction, and **(c)** 1-butanol introduction.

Figure 3.8 provides the growth factors of protein ions with different condensable vapors introduced as a function of the saturation ratio. Measurement error was minimized by monitoring the sheath flow rates with pressure sensors and injecting vapors with gas

tight syringes. In general, the highest growth factor was observed with nonane vapor introduction followed by 1-butanol and water. Exceptionally, apoferritin showed the highest growth factors with water vapor introduction followed by nonane and 1-butanol. With water vapor, the growth ratios of larger protein ions (i.e. those with larger monomer mobility diameters) were higher than the growth factors of smaller protein ions. However, with nonane and 1-butanol, the opposite tendency was observed; smaller protein ions presented higher growth factors. In addition to growth factors, the average of number of vapor molecules adsorbed onto protein monomer ions were calculated, based on the shift in mean protein ion volume at each saturation ratio. Results are summarized in table 3.1. At a saturation ratio of 100% of water vapor, 304.8 molecules, 475.2 molecules, 932.9 molecules, and 5418.7 molecules were condensed on a bovine serum albumin monomer, a transferrin monomer, an immunoglobulin G monomer, and an apoferritin monomer, respectively. At a saturation ratio of 100% of nonane vapor, 79.2 molecules, 113.5 molecules, 190.4 molecules, and 478.4 molecules were condensed on a bovine serum albumin monomer, a transferrin monomer, an immunoglobulin G monomer, and an apoferritin monomer, respectively. Lastly, at a saturation ratio of 75% of 1-butanol, 141.7 molecules, 185.0 molecules, 279.5 molecules, and 595.7 molecules were condensed on a bovine serum albumin monomer, a transferrin monomer, an immunoglobulin G monomer, and an apoferritin monomer, respectively.

Table 3.1 Nominal number of vapor molecules condensed on protein monomer ions generated from pH 7 solution at each saturation ratio.

Vapor	**Water**		**Nonane**				**1-Butanol**		
Saturation ratio (%)	**50%**	**100%**	**25%**	**50%**	**75%**	**100%**	**25%**	**50%**	**75%**
Bovine serum albumin	80.7	304.8	20.1	42.8	64.6	79.2	62.5	94.5	141.7
Transferrin	174.8	475.2	29.0	61.8	94.5	113.5	95.8	139.9	185.0
Immunoglobulin G	343.8	932.9	50.8	100.1	163.1	190.4	137.6	202.1	279.5
Apoferritin	1614.1	5418.7	117.1	239.1	404.2	478.4	306.7	423.5	595.7

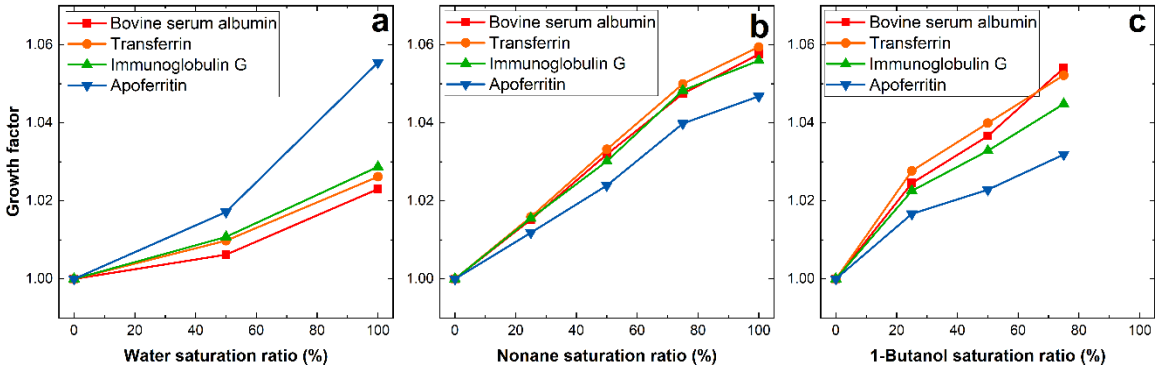

Figure 3.8 Growth factors of monomers with **(a)** water introduction, **(b)** nonane introduction, and **(c)** 1-butanol introduction.

In κ-Köhler theory, an ion size effect is naturally present via the Kelvin-capillarity term, i.e. the increase in saturation ratio by a factor exp $\left(\frac{4\sigma M_w}{RT\rho\bar{d}_p}\right)$. A consequence of this term is that based on the capillarity model, higher saturation ratios should be required to drive vapor uptake for smaller ions. However, this is only observed for water (the highest surface tension condensable vapor) in the present study. This suggests that there are protein-specific activity coefficients for the condensable vapors examined, parameterized by κ. Figure 3.9 displays κ from regression to measurements with singly charged monomer ions from pH 7 solution.

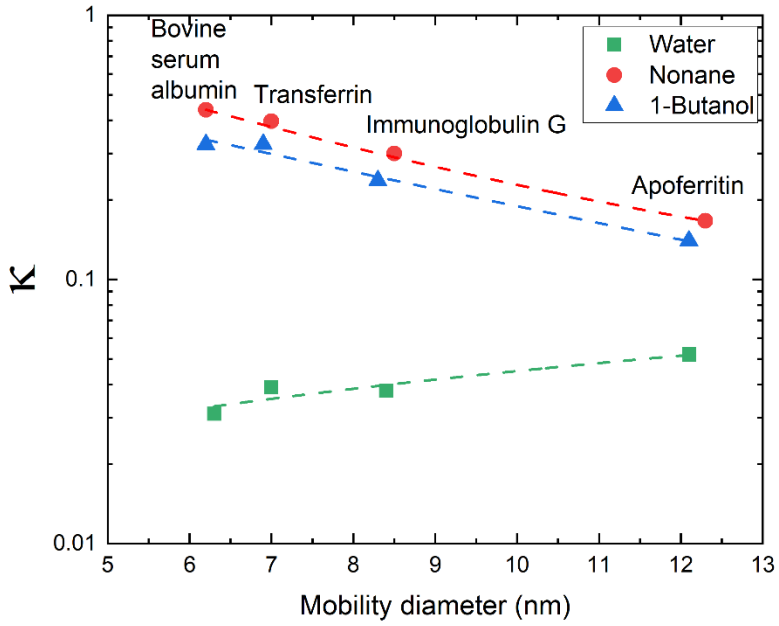

Figure 3.9 Inferred κ of protein monomers for water, nonane, and 1-butanol.

We remark that as shown in figure 3.2, fits to determine κ are not highly linear as they commonly are when examining vapor uptake by salt or other solvent-soluble molecule-containing aerosol particles. Therefore, the inferred κ are best utilized qualitatively to examine differences in uptake between the Köhler model (incorporated the Kelvin effect and Raoult's law, but with $\kappa = 1$). Larger κ reflects greater affinity for the condensable vapor introduced. As expected based upon mobility spectra shifts, κ values for nonane are higher than those for the other two vapor types. κ for nonane and 1-butanol decreases with protein ion size, and κ for water increases as the size of protein increases, indicating even for water there is a size effect beyond that predicted by the capillarity model.

We therefore conclude that condensable vapor uptake by low charge state protein ions displays additional information beyond that from mobility measurements in the absence of condensable vapor; however, we still observe correlations between the extent

of uptake and protein ion size (though with different trends in κ with size for different condensable vapor molecules). A subsequent question is then whether the extent of uptake changes with original solution pH and protein ion extent of clustering. Figure 3.9 displays the growth factors of protein monomers at different pH levels. The isoelectric points of bovine serum albumin, transferrin, immunoglobulin G, and apoferritin are pH 4.5-5.0, 6, 6.6-7.2 and, 4.8, respectively, indicating all examined proteins are positively charged at pH 3 and negatively charged at pH 10. While the solution pH and charge state in solution has no apparent bearing on protein ion charge state based on the aerosolization and ionization mechanism employed in the present study, it may have an influence on the gas phase structure of each ion. It is worthy to note that we did not observe apoferritin in the high and low pH solutions examined, though these pHs are close to the apoferritin stability limits. In figure 3.10, larger standard deviations and variations of the growth factors were observed with water vapor introduction only, with differences with nonane and 1-butanol introduction undetectable. This indicates that water vapor uptake in the gas phase is altered by changes in protein solution phase structure, with some of these changes presumably maintained in the gas phase; however, the overall influence is small, and solution pH does not appear to greatly affect the vapor uptake by protein ions in the gas phase.

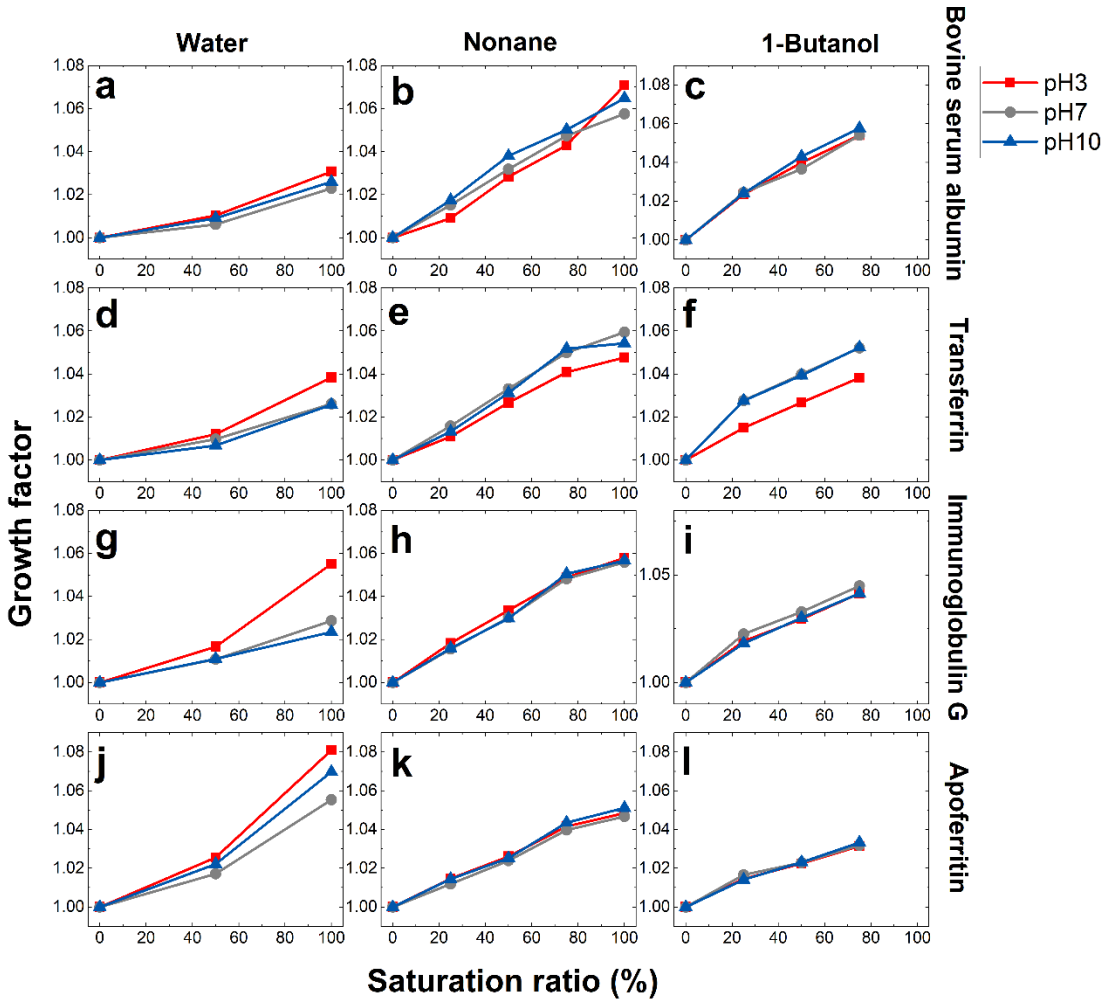

Figure 3.10 The growth factors of proteins exposed to condensable vapors nebulized at different pH levels. **a)** bovine serum albumin – water, **b)** bovine serum albumin – nonane, **c)** bovine serum albumin – 1-butanol, **d)** transferrin – water, **e)** transferrin – nonane, **f)** transferrin – 1-butanol, **g)** immunoglobulin G – water, **h)** immunoglobulin G -nonane, **i)** immunoglobulin G – 1-butanol, **j)** apoferritin – water, **k)** apoferritin – nonane and **l)** apoferritin – 1-butanol

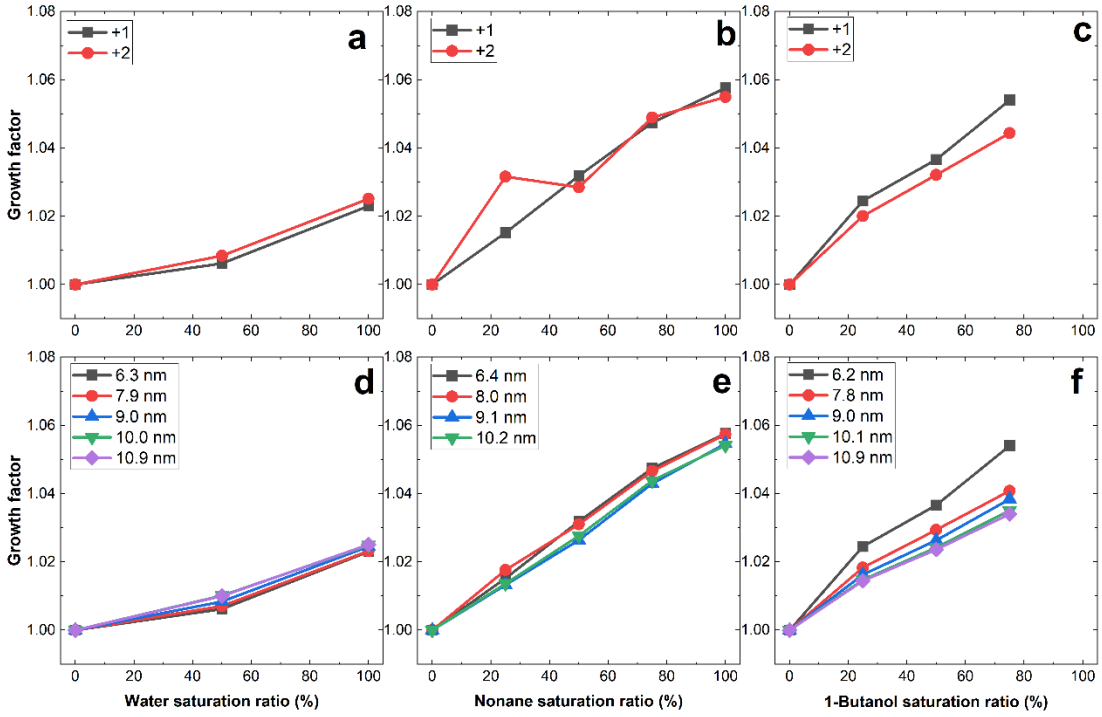

Figure 3.11 Growth factors of doubly and singly charged bovine serum albumin monomers with **(a)** water introduction, **(b)** nonane introduction, and **(c)** 1-butanol introduction. Growth factors of bovine serum albumin multimers with **(d)** water introduction **(e)** nonane introduction **(f)** 1-butanol introduction

The growth factors of singly charged monomers and doubly charged monomers of bovine serum albumin are plotted as a function of saturation ratio for test 3 condensable vapors in Figure 3.11a-c. Importantly, we recover the same growth factors for both charge states. We note that in calculating these growth ratios, n = 2 (doubly charged) is input into the Stokes-Millikan equation. Different growth factors for different charge states would likely suggest issues with calibration or in the data analysis approach employed as Coulombic influences in both singly and doubly charged protein ions in the size range are not significant enough to influence vapor uptake (though it can have a substantial effect at higher charge levels, or the single nanometer scale; Nasibulin et al., 2008, Gamero-Castaño and de la Mora, 2002, Kuldinow et al., 2021) Figure 3.11d-f displays the growth factors of

multimers of bovine serum albumin. Multimer ion growth factors show the same tendency as monomer ions; larger proteins grew more with water vapor and smaller proteins grew more with nonane and 1-butanol vapor, the effect is small with bovine serum albumin. With water vapor, the multimer growth factor observed here are slightly below those observed for similar saturation ratios by Wang et al. (2019), who examine 40 nm -100 nm larger protein particles. However, because of the observed size dependency of water uptake, we find our results are consistent with this prior study.

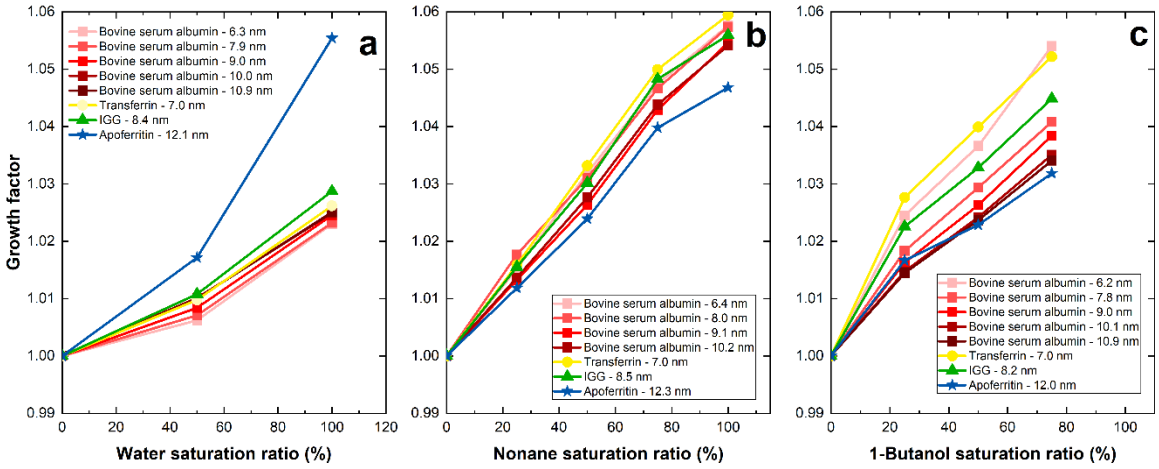

Figure 3.12 Growth factors of different protein ions including multimers of bovine serum albumin protein ions with **(a)** water introduction, **(b)** nonane introduction, and **(c)** 1-butanol introduction.

By examining bovine serum albumin multimer growth factors alongside other proteins, we find that the water growth factor is not solely determined by protein ion mobility diameter, but does also depend on the protein itself. As shown in Figure 3.12, for different water vapor saturation ratios, the growth factors of multimers of albumin protein ions are smaller than growth ratios of transferrin and immunoglobulin G, even when mobility diameters of multimers are larger than those of transferrin and immunoglobulin

G monomers. Meanwhile, with nonane vapor and 1-butanol vapor, the size of the protein ion likely plays a more dominant role in determining extent of vapor uptake, as the growth ratios mostly agree well with the order of mobility diameters of protein ions, irrespectively of exact protein composition.

3.4 Conclusions

We examined the gas phase vapor uptake by 4 protein ions in the mass range of 66-444 kDa by tandem DMA measurements, using 3 different condensable vapors with protein ions produced from 3 different pH level solutions. To avoid Coulombic stretching of resulting protein ions which occurs at sufficiently high charge state, ions were instead generated first using pneumatic nebulizer for aerosolization and second using Kr-85 radioactive source for atmospheric pressure chemical ionization, yielding only singly and doubly charged protein ions. The mobility diameters of protein ions, determined using the Stokes-Millikan equation, are comparable to those produced by charge reduction electrospray sources. For monomers generated from pH 7 solution, the growth factors with water vapor increased as the size of protein increases. This trend with size however is reversed with nonane and 1-butanol; for these condensable vapors the growth factor decreased with increasing ion mobility diameter. The introduction of nonane vapor yielded the highest growth factors, around 1.06 at saturation, for bovine serum albumin, transferrin, and immunoglobulin G ions, whereas apoferritin ions grew most noticeably with water vapor. Fitting to κ – Köhler theory, κ values for nonane were higher than 1-butanol and water. Changes in pH of the original protein solution did not lead to appreciable impacts on growth factors other than slightly larger standard deviations, and increased variations in

growth factors with water vapor introduction. Additionally, we observed that the growth factors of singly and doubly charged bovine serum albumin ions are identical. Multimer ion growth factors show the same tendency as monomer ions.

In total, measurements demonstrate how controlled condensable vapor uptake yields additional information from mobility measurements beyond traditional low-field IMS experiments. At the same time, much of the observed uptake behavior can be correlated with mobility diameter, suggesting vapor uptake for protein ions is not completely orthogonal as a separation or characterization tool to mobility. Nonetheless, we argue that modulation of condensable vapor concentrations may be a useful tool in optimizing mobility based measurement schemes, not only for small ions as examined in previous work (Kwantwi-Barima et al., 2019, Kwantwi-Barima et al., 2020, Kwantwi-Barima et al., 2017), but also macromolecular ions. Controlled condensation of vapors onto ions likely also affects ion reactivity in the vapor phase, e.g. products of collision induced dissociation for multiprotein complexes (Bornschein et al., 2016), and may further be exploited in the development of tandem mobility-mass spectrometry measurement schemes.

Chapter 4. IMS-DMS analysis for MS free multi-dimensional analysis

4.1 Introduction

The behavior of ions at high electric field within carrier gas molecules have been of interest in physical chemistry for several decades (Mason and McDaniel, 1988a, Ellis et al., 1976, Ellis et al., 1978, Mason, 1984, Viehland and Mason, 1995). At higher electric fields, ions are further accelerated by electrical force leading to highly energetic collisions between ions and ambient gas molecules. Therefore, the ion mobility cannot be considered as a constant coefficient, but it is defined as a function of field strength (E) and carrier gas density (N) where E determines the acceleration magnitude and N affects the duration of acceleration before each collision. The dependence on E/N is ion specific and there are three general types of tendency; for type A ions, mobility increases, for type B ions, mobility first increases and at higher fields it begins to decrease, and for type C ions mobility decreases as E/N increases (Guevremont and Purves, 1999). Some research has also indicated that this tendency can be changed for a given ion by the introduction of different carrier gas (Barnett et al., 2000).

In 1993, a new mobility spectrometer to separate ions based on the dependence of ion mobility on E/N was developed (Buryakov et al., 1993), called different mobility spectrometers (DMSs) or high field asymmetric ion mobility spectrometers (FAIMSs). It applies a time-dependent asymmetric voltage waveform to electrodes to form a bidirectional electric field between high field limit and low field limit perpendicular to carrier gas flow. While the integral of applied waveform during a single period is equal to zero (the high electric field is applied for a shorter amount of time and low electric field is applied for a longer amount of time), the distance an ion drifts due to electrical force during

a period is not equal to zero unless their mobility is identical at high field and low field. Therefore, ions drift toward one electrode and eventually deposit on one side as shown in figure 4.1. Ions can be transmitted through the asymmetric electric field by applying a small dc voltage called compensation voltage (CV) to correct the displacement caused by mobility difference which is ion specific. FAIMSs filter ions based on CVs at an assigned high field called a dispersion field.

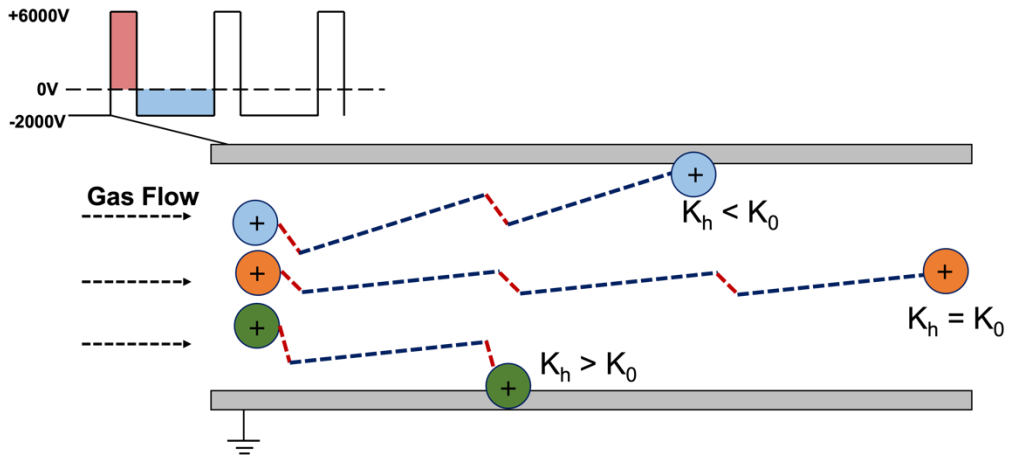

Figure 4.1 Ion trajectory during transmission through an asymmetric electric field.

Since its development in the 1990s, numerous experimental and numerical studies have been conducted for the implementation of this technology and several versions of FAIMSs were commercialized by different companies (Guevremont, 2004). Recently, microchip based FAIMSs called ultra FAIMS or μ FAIMS were developed benefiting from advances in microfabrication processes (Miller et al., 2001, Buryakov et al., 2001, Shvartsburg et al., 2009). Its micro dimensions provide ultra-high field strength with low power consumption, short measurements time (100 times faster than conventional FAIMSs), reduced product size, and operation under atmospheric pressure. FAIMS can be

an independent analysis tool for detection of explosives, chemical warfare agents, and drugs, and for breath analysis (Eiceman and Stone, 2004, Guddat et al., 2009, Covington et al., 2015). In the meantime, it has also been widely used as a hyphenated system with mass spectrometers (MS) for multi-dimensional analysis of peptides and proteins (Shvartsburg et al., 2006, Purves et al., 2000, Robinson and Williams, 2005, Kolakowski and Mester, 2007).

However, the use of FAIMS as a hyphenated system with differential mobility analyzers (DMAs), which can function as a continuous source of monomobile ions, has not been explored. While DMAs in aerosol science have been used for larger particle ions (3-1000 nm) compared to the ions analyzed by drift tube ion mobility spectrometers (DTIMSs) and FAIMSs, in recent decades novel high resolution DMAs (HRDMAs) have been developed (de la Mora and Kozlowski, 2013, Rus et al., 2010, Rosser and De La Mora, 2005, Rus et al., 2008) which can separate sub 2nm ions which allows some overlap of the measurement range of ultra FAIMSs and HRDMAs. The unique combination of a DMA and a FAIMS could allow for the identification of the actual K_h as a function of *E/N* for numerous ions which has not yet been fully determined. The hyphenated system yields two dimensional data based on orthogonal properties in a solely mobility based configuration and maintaining a short measurement time, effectively expanding the measurement capability of ion mobility spectrometry.

In this study, a DMA-FAIMS system was newly implemented to conduct multi-dimensional analysis by separating ions based on low field mobility and mobility dependence on E/N. Tetraalkylammonium salts were selected to test this setup because their low field mobility has been precisely determined by DMA measurements in previous

studies (Ude and De La Mora, 2005). Additionally, they are highly monodisperse which is preferred for mobility standards. Previous studies have investigated the general behavior of tetraalkylammonium ions at high field strengths (Aksenov and Kapron, 2010) using a FAIMS-MS system but analysis on compensation voltages is only applicable to the unique FAIMS instrument used in the measurements (Aksenov et al., 2012). Also, ion-molecululular clustering of tetraaklyammonium ions with different configurations of carrier gas has been investigated by a FAIMS-MS (Campbell et al., 2014). In this work, the general behavior of tetraalkylammonium ions was examined using a DMA-FAIMS system and actual K_h values as a function of *E/N* was obtained for the tested ions. This additional analysis allows for the data to be applied and compared universally to data obtained from other systems.

4.2 Methods

4.2.1 Experimental Methods

Tetrabutylammonium iodide (TBAI), Tetraheptylammonium bromide (THAB), Tetradecylammonium bromide (TDAB), and Tetra dodecylammonium bromide (TDDAB) were purchased from Sigma-Aldrich. 2mM of each sample was dissolved into methanol. Samples were aerosolized and ionized by electrospray ionization (ESI) for IMS-DMS measurements and details on ESI are described in elsewhere (Fenn et al., 1989, Hogan and de la Mora, 2011). The mobility distribution of tetraalkylammonium ions in low field limits were obtained by an ESI-DMA-electrometer system and CV:DV contour maps of ions were obtained by an ESI-DMA-FAIMS system shown in figure 4.2.

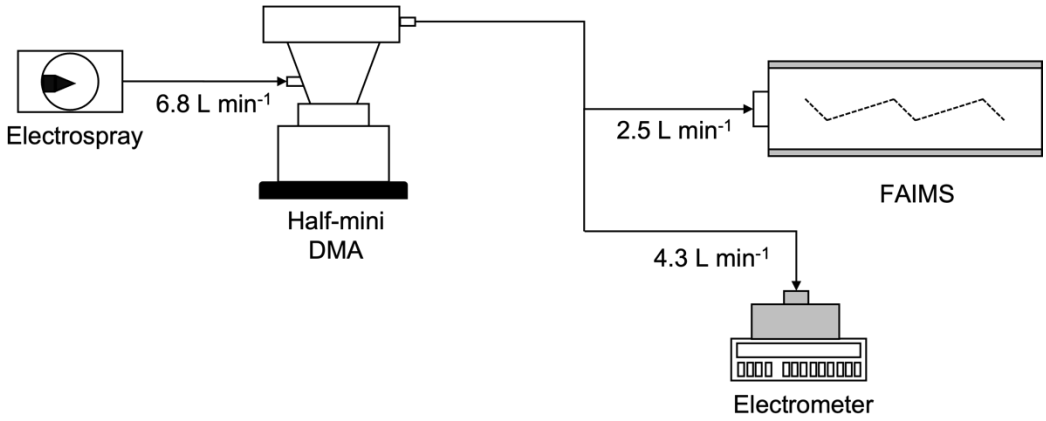

Figure 4.2 The schematic of mobility measurements with an ESI-DMA-FAIMS and an ESI-DMA-FAIMS.

Before measurements, each solution was diluted with the ratio of 500:1 with methanol and it was introduced to a 1mL vial. A fused silica capillary tube with inner diameter of 40μm was immersed in the suspension in the vial and high voltage of 2-3 kV was applied to the sample by an inserted electrode connected to the voltage power supply. The sample vial was pressurized by a syringe to push the flow through the capillary tube and the other end of the capillary tube was located inside a chamber having inlet and outlet gas sampling ports. At the inlet of the chamber, a filter and a diffusion dryer were installed, and the outlet was directly connected to the inlet of a half mini DMA. There were glass panes on each side of the chamber which enable monitoring a Taylor cone formed at the end of the capillary. To maintain electrospray stability through measurements, the current is monitored and maintained to be 100-200 nA.

First mobility spectra for each sample were obtained using a half mini DMA and an electrometer. The detailed specifications of half mini DMAs are described in detail (de la Mora and Kozlowski, 2013). The DMA was operated with a circulating sheath flow of air by a vacuum blower and a heat exchanger was used to maintain the temperature of the

sheath flowrate at the room temperature by preventing it affected by the temperature of the blower. Since the sheath flow is in the order of 100 L min^{-1}, it was calculated from the peak voltage of tetraheptylammonium $(THA)^+$ ion and its mobility determined by previous measurements instead of direct measurements.

$$Q_{sh} = \frac{2\pi KLV}{\ln(r_{out}/r_{in})} \quad (4.1)$$

Where Q_{sh} is sheath flowrate, K is mobility, L is length of the DMA (20 mm), V is the DMA voltage, r_{out} is outer radius of the DMA (6 mm), and r_{in} is the inner radius of the DMA (4 mm). In this study, the voltage corresponding to THA^+ ion whose mobility is 0.97 $cm^2\ V^{-1}\ S^{-1}$ in the air was 142.5 V and the equation (4.1) yields $Q_{sh} = 257$ L min^{-1}. The sample flowrate of ions entering and exiting the DMA was determined by the flow rates of a FAIMS and an electrometer at the downstream which was 6.8 L min^{-1}. The high voltage of the DMA was controlled by an external voltage supply and a negative voltage was applied to the inner electrode of the DMA and the outer electrode was grounded. With assigned DMA voltage and sheath flowrate, positively charged ions travel toward the inner electrode and ions with the selected mobility exit through the outlet. For the mobility spectra measurements in low field limit, we measured the concentration of ions coming out of the DMA at each voltage while stepping the voltage sequentially within the range of 0-500 V. In this study, between each voltage step there was a 5 second delay to allow transitional particles to fully travel through the system while the voltage was adjusted. Following this delay, measurements were taken for 3 seconds. Currents were recorded as the average over this 3 second measurement period and converted to concentrations using the equation (4.2).

$$I = QNe \quad (4.2)$$

where I is measured current, N is the number concentration of ions, e is charge of an electron, Q is the flowrate which was 4.3 L min $^{-1}$ in this study. The outlet of the electrometer was connected to vacuum line of the building and the flowrate was determined by the critical orifice used in this study. Mobility spectra were obtained after converting each applied DMA voltage to corresponding mobility based on equation (4.1).

To investigate mobility dependence of tetraalkylammonium ions on high electric field, ions were analyzed further using an ESI-DMA-FAIMS (Lonestar, Owlstone Inc). In DMA-FAIMS measurements, the DMA voltage was held at a constant value of our interest (voltages corresponding to monomer ions) and ions with a certain mobility were introduced to the FAIMS (Before FAIMS measurements, a built-in Ni-63 radioactive source was removed inside the FAIMS to avoid another charging event of selected ions.). The flowrate through the FAIMS system was 2.5 L min $^{-1}$ and it was controlled by an attached pump at the downstream of the FAIMS. The separation in the FAIMS occurs in a channel with 35 μm gap and 300 μm length with an asymmetric voltage applied having an asymmetric waveform generated by a RF oscillator with 25MHz. While ions are traveling through FAIMS, the dispersion voltage (DV) is increased from 0 % intensity to 100% intensity (214 V) with an increment of 2 %. At each DV, the system applies varying compensation voltage (CV) to the channel from -6 V to 6 V with 512 steps. After ions are introduced to a channel, they experience perpendicular oscillations between two electrodes being exposed to electric fields with alternating directions. If an ion mobility is a constant value through varying field strength, average drifting distance over a period will be zero. However, over each period, a displacement toward one electrode is added and ions will end up depositing on to one electrode unless they are compensated by an assigned CV.

Therefore, only ions with a mobility dependence which can be canceled by an applied CV can transmit through the channel. Ion signal intensities as a function of CV result from sweeping CV for a given dispersion voltage and waveform shape. Filtered ions are detected using a charge collector biased at +55 V for negative ions and at – 55 V for positive ions. The maximum dispersion voltage and dimensions of a channel are found in a study by Shvartsburg et al. (2009) and further details are described in the study by Shvartsburg et al. (2009). As results, ion current intensity maps are reported for four ions with 26,112 data points (512 CVs at 51 DVs).

4.2.2 Mathematical description on data analysis

Unfortunately, data interpretation in FAIMS is not as straightforward as a traditional low-field mobility measurement. At high electric fields (for example, greater than 2.5kV/cm), *K* is a function of the ratio of electric field strength to the gas number density (*N*), *E/N*. Not only do small ions have variable field strength mobilities, all ion and charged particle mobilities are functions of *E/N* and the mobility at high electric field, K_h can be described as (Mason and McDaniel, 1988a):

$$K_h\left(\frac{E}{N}\right) = K_0\left(1 + \alpha_2\left(\frac{E}{N}\right)^2 + \alpha_4\left(\frac{E}{N}\right)^4 + \cdots\right) = K_0\left(1 + \sum_{n=1}^{\infty}\alpha_{2n}\left(\frac{E}{N}\right)^{2n}\right)$$

$$= K_0(1 + \alpha) \qquad (4.3)$$

where α is a function of ion specific mobility dependence on electric field strength and gas density. The α function is approximated as an even power series of $\left(\frac{E}{N}\right)$ considering symmetry factors like electric field directions and is a mathematical approach to interpret data collected by different instruments. Therefore, it is known that the use of this format of

α function should be applied carefully and it is not recommended to extrapolate values beyond original measurement ranges. A FAIMS utilizes this dependency of mobility on *E/N* to separate gas-phase ions by applying an asymmetric electric field. While the ideal waveform for the asymmetric voltages (V) applied to FAIMSs are perfect square waveforms, a bisinusoidal waveform is used for practical and safety purposes which is described (Purves et al., 1998, Carnahan and Tarassov, 1995, Shvartsburg et al., 2009):

$$V = \frac{2V_d sin(\omega t) + V_d sin(2\omega t - \frac{\pi}{2})}{3} \tag{4.4}$$

where V_d is dispersion voltage, ω is angular velocity, and t is time. Since voltages are not constant values at both low field and high field limits, measured compensation voltages need to be processed properly to obtain mobility (K_h) at high field strengths which is analyzed and described in previous studies (Buryakov et al., 1993, Buryakov, 2002, Krylov et al., 2002). Details are as follows. Under standard pressure conditions, equation (4.3) can be modified into:

$$K_h(E) = K_0(1 + \alpha_2(E)^2 + \alpha_4(E)^4 + \cdots) \tag{4.5}$$

where α is approximated as an even power series of E, $\alpha = \sum_{n=1}^{\infty} \alpha_{2n}(E)^{2n}$. The dispersion field in a FAIMS follows these conditions:

$$\frac{1}{T} * \int_0^T E_D(t)dt = \langle E_D(t) \rangle = E_D \langle f(t) \rangle = 0 \tag{4.6}$$

$$\langle f^{2n+1}(t) \rangle \neq 0 \tag{4.7}$$

where T is the period of the applied wave form, t is time, E_D is the maximum field strength of the waveform, f is the waveform function, and $\langle f^{2n+1}(t)\rangle = \frac{1}{T}\int_0^T f^{2n+1}(t)$. Once the compensation voltage is applied, the electric field can be expressed:

$$E(t) = E_D(t) + E_c = E_D f(t) + E_c \tag{4.8}$$

where E_c is the electric field strength generated by the compensation voltage. Ions with an average velocity of 0 as shown in equation (4.9) will transmit through the plates and approach the detector of the FAIMS.

$$\langle v(t)\rangle = \langle K(E)E(t)\rangle =$$

$$\langle K_0\big(1 + \alpha(E)\big)(E_D(t) + E_c\rangle =$$

$$\langle K_0(1 + \alpha(E_D(t) + E_c))(E_D(t) + E_c\rangle = 0 \tag{4.9}$$

Power series expansion by Taylor's theorem is used under the condition $E_c \ll E_D$.

$$(E_D(t) + E_c)^n \approx \big(E_D f(t)\big)^n + n\big(E_D f(t)\big)^{n-1} E_c \tag{4.10}$$

Then $\alpha(E_D(t) + E_c))$ can be approximated as:

$$\alpha(E_D(t) + E_c) = \textstyle\sum_{n=1}^{\infty} \alpha_{2n}(E_D(t) + E_c)^{2n}$$

$$\approx \sum_{n=1}^{\infty} \alpha_{2n}\big(E_D(t)\big)^{2n} + \sum_{n=1}^{\infty} 2n\alpha_{2n}\big(E_D(t)\big)^{2n-1} E_c$$

$$= \alpha\big(E_D(t)\big) + E_c \frac{d\alpha\big(E_D(t)\big)}{dE_D(t)} \tag{4.11}$$

If $\alpha(E_D(t)+E_c))$ is substituted with the approximated form shown in equation (4.11), the condition can be expressed and expanded after dividing it by K_0 :

$$\langle(1+\alpha\big(E_D(t)\big)+E_c\frac{d\alpha\big(E_D(t)\big)}{dE_D(t)})(E_D(t)+E_c\rangle=0 \quad \text{(4.12-a)}$$

$$\langle E_D(t)+E_c+\alpha\big(E_D(t)\big)E_D(t)+\alpha\big(E_D(t)\big)E_c+E_c\frac{d\alpha\big(E_D(t)\big)}{dE_D(t)}E_D(t)+{E_c}^2\frac{d\alpha\big(E_D(t)\big)}{dE_D(t)}\rangle=0 \quad \text{(4.12-b)}$$

$$E_c+\langle\alpha\big(E_D(t)\big)E_D(t)\rangle+E_c\langle\alpha\big(E_D(t)\big)\rangle+E_c\langle\frac{d\alpha\big(E_D(t)\big)}{dE_D(t)}E_D(t)\rangle=0 \quad \text{(4.12-c)}$$

Equation (4.12-b) can be rearranged into (4.12-c) since $\langle E_D(t)\rangle = 0$ according to the equation (4.6) which is a requirement for an asymmetric wave from used in a FAIMS and ${E_c}^2\frac{d\alpha\big(E_D(t)\big)}{dE_D(t)}$ can be eliminated based on the condition $E_c \ll E_D$. Then, by arranging (4.12-c), E_c can be expressed as function of α and $E_D(t)$:

$$-E_c=\frac{\langle\alpha\big(E_D(t)\big)E_D(t)\rangle}{1+\langle\alpha\big(E_D(t)\big)\rangle+E_c\langle\frac{d\alpha\big(E_D(t)\big)}{dE_D(t)}E_D(t)\rangle} \quad \text{(4.13-a)}$$

Equation (4.13-a) can be simplified as (4.13-b) by using $E_D(t)=E_Df(t)$ and putting $\alpha\big(E_D(t)\big)$ just as α.

$$-E_c=\frac{E_D\langle\alpha f(t)\rangle}{1+\langle\alpha\rangle+E_D\langle\frac{d\alpha}{d\big(E_D(t)\big)}f(t)\rangle} \quad \text{(4.13-b)}$$

Then, it can be rearranged as (4.13-b) after substituting α with $\sum_{n=1}^{\infty}\alpha_{2n}(E_Df(t))^{2n}$ and can be expressed as:

$$-E_c = \frac{\sum_{n=1}^{\infty} \alpha_{2n} {E_D}^{2n+1} \langle f^{2n+1}(t) \rangle}{1+\sum_{n=1}^{\infty} (2n+1) \alpha_{2n} {E_D}^{2n} \langle f^{2n}(t) \rangle} \quad (4.13\text{-c})$$

E_c can be expressed as an odd power series of E_D:

$$-E_c = \sum_{n=1}^{\infty} c_{2n+1} {E_D}^{2n+1} = c_3 {E_D}^3 + c_5 {E_D}^5 + \cdots \quad (4.13\text{-d})$$

where $c_{2n+1} = \alpha_{2n} \langle f^{2n+1} \rangle - \sum_{k=1}^{n-1} (2(n-k)+1) c_{2k+1} \alpha_{2(n-k)} \langle f^{2(n-k)} \rangle$. If n is considered up to 2,

$$-E_c = c_3 {E_D}^3 + c_5 {E_D}^5 \quad (4.14)$$

a polynomial version of E_c can be obtained where $c_3 = \alpha_2 \langle f^3 \rangle$ and $c_5 = \alpha_4 \langle f^5 \rangle - 3 c_3 \alpha_2 \langle f^2 \rangle$. $\langle f^2 \rangle$, $\langle f^3 \rangle$, and $\langle f^5 \rangle$ can be calculated analytically and numerically or can be measured. Experimental data of E_c: E_D can be used to fit this polynomial model. (Krylov et al., 2002) used a standard least-squares method to approximate the experimental findings. Equation (4.14) can be shown as a linear form:

$$y = c_3 + c_5 x \quad (4.15)$$

where $y = \frac{-E_c}{{E_D}^3}$ and $x = {E_D}^2$. c_3 and c_5 can be approximated from experimental data,

$$c_5 = \frac{\sum_{i=1}^{N_{exp}} x_i \sum_{i=1}^{N_{exp}} y - N_{exp} \sum_{i=1}^{N_{exp}} x_i y_i}{\left(\sum_{i=1}^{N_{exp}} x_i\right)^2 - N_{exp} \sum_{i=1}^{N} {x_i}^2} \quad (4.16)$$

$$c_3 = \frac{1}{N_{exp}} \left(\sum_{i=1}^{N_{exp}} y - c_5 \sum_{i=1}^{N_{exp}} x_i \right) \quad (4.17)$$

where N_{exp} is the number of experimental data points. In this study, 10 data points were for TBA^+ ions and 12 data points for THA^+, TDA^+, and $TDDA^+$ ions. The used data points of DV and EV are summarized in Table 4.1.

Table 4.1 Measured compensation voltages (CVs) and dispersion field strengths of monomers of tetraalkylammonium ions at 295 K, 1 atm. The maximum dispersion voltage applied was 214 V and the gap distance of the channel is 35 μm.

TBA		THA		TDA		TDAA	
E_D/N (Td)	CV(V)	E_D/N (Td)	CV(V)	E_D/N (Td)	CV(V)	E_D/N (Td)	CV(V)
59.0	0.036	59.0	0.077	59.0	0.009	59.0	0.036
73.7	0.023	73.7	0.171	73.7	0.036	73.7	0.090
88.5	0.224	88.5	0.240	88.5	0.076	88.5	0.184
98.3	0.292	98.3	0.198	98.3	0.198	98.3	0.211
113.1	0.467	113.1	0.319	113.1	0.346	113.1	0.440
122.9	0.620	122.9	0.521	122.9	0.494	122.9	0.494
137.6	0.899	137.6	0.764	137.6	0.723	137.6	0.696
147.5	1.330	147.5	0.980	147.5	0.872	147.5	0.939
177.0	2.297	172.0	1.596	172.0	1.411	172.0	1.505
206.5	3.939	196.6	2.297	196.6	2.071	196.6	2.112
		221.2	3.354	221.2	2.799	221.2	2.920
		245.8	4.281	245.8	3.675	245.8	3.864

4.3 Results and Discussion

Figure 4.3 displays mobility spectra of TBAI, THAB, TDAB, and TDDAB ions generated and ionized by an ESI. Before the conversion of DMA voltages to ion mobilities, calibration of the DMA was conducted by comparison of mobility spectra of THAB obtained from ESI-DMA-electrometer measurements to mobility spectra determined by (Ude and De La Mora, 2005). Ude and De La Mora reported 0.97 $cm^2\ V^{-1}\ S^{-1}$ for monomer ions and 0.65 $cm^2\ V^{-1}\ S^{-1}$ for dimer ions and the ratio of the monomer mobility to dimer mobility was 1.48. In this study, the ratio of 1.50 was observed which agrees reasonable enough to identify monomer ions and dimer ions of THAB. Then, DMA voltages were converted to mobilities using equation (4.1) and the sheath flowrate of 257 L min^{-1}. Ion mobilities for TBA^+, THA^+, TDA^+, and $TDDA^+$ were 1.42 $cm^2\ V^{-1}\ S^{-1}$, 0.97 $cm^2\ V^{-1}\ S^{-1}$,

0.78 $cm^2\ V^{-1}\ S^{-1}$ and 0.72 $cm^2\ V^{-1}\ S^{-1}$ respectively and they were identified as major peak in figure 4.3. These values are consistent with the mobilities determined by Ude and De La Mora within 2 % difference. In addition to monomer ions, dimer ions and doubly charged clusters were labeled in the figure when they were able to be identified by mobilities reported by by Ude and De La Mora. For the concentration of each major peak was near 10^5 # cm^{-3} except TBAI of which concentration was 2×10^4 # cm^{-3}. It is necessarily required to secure high enough ion concentration for DMA-FAIMS measurements since the transmission efficiency of ions further decrease through a high electric field of a FAIMS especially for ions with higher mobility.

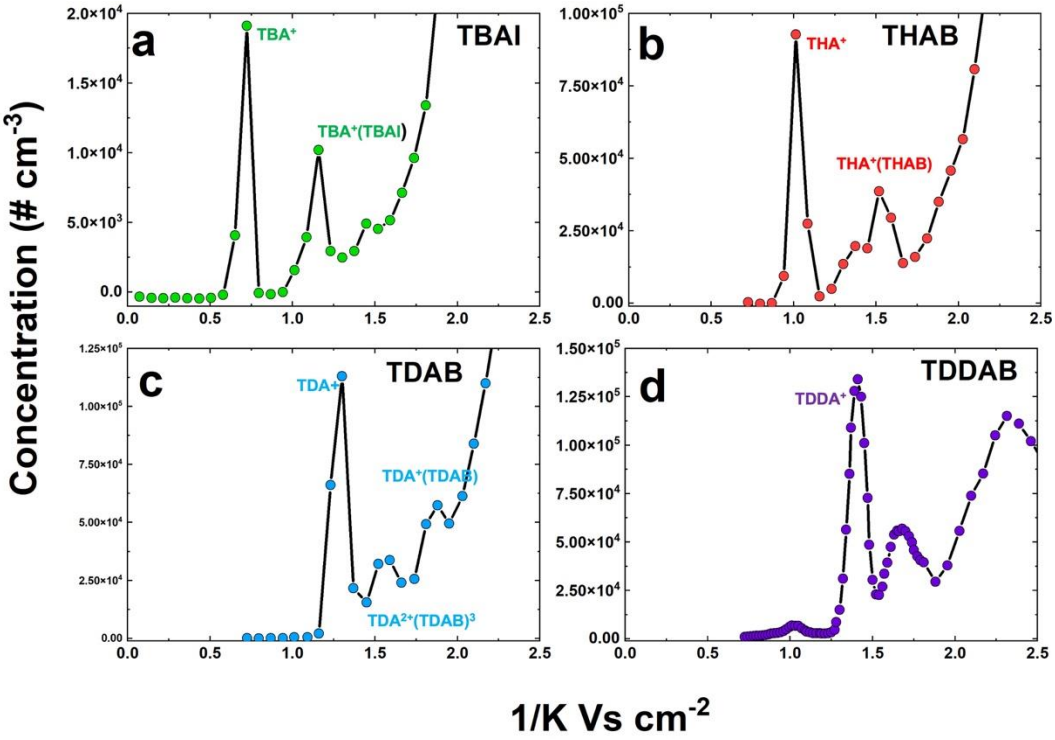

Figure 4.3 Mobility spectra of **(a)** tetrabutylammonium iodide (TBAI), **(b)** tetraheptylammonium bromide (THAB), **(c)** tetradecylammonium bromide (TDAB), and **(d)** tetradodecylammonium bromide (TDDAB).

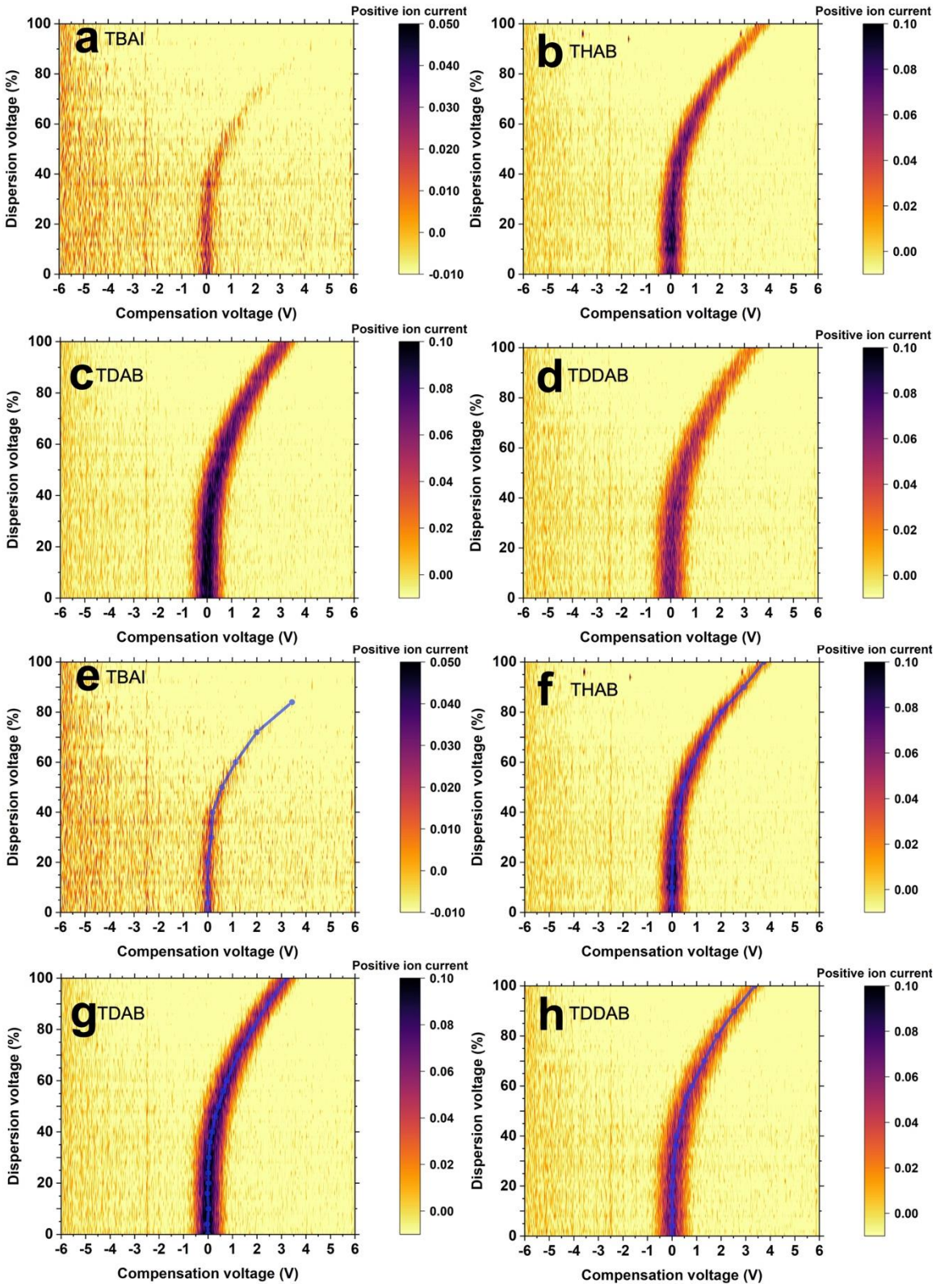

Figure 4.4 CV:DV color map by ESI-DMA-FAIMS measurements of monomer ions of **(a)** tetrabutylammonium iodide (TBAI), **(b)** tetraheptylammonium bromide (THAB), **(c)**

tetradecylammonium bromide (TDAB), and **(d)** tetradodecylammonium bromide (TDDAB). **(e-g)** are same color maps with the center guide lines.

Figure 4.4 (a-d) show the color maps of CV:DV obtained by ESI-DMA-FAIMS measurements of monomer ions of 4 samples and (e-h) show the identical maps with added center lines. The centerline was obtained by finding the center of the mode at each dispersion voltage and center values were not necessarily peak maximum. Low signal intensity of TBA+ ions shown in mobility spectra yielded noisy CV maps compared to CV maps of other ions and ion current was barely detected when the dispersion voltage was 80% or higher. It is explained by the known tendency that ion transmission efficiency in a planar FAIMS decreases as its dispersion field increases while the resolution increases and the loss rate is higher with ions with higher mobility (higher diffusion coefficient). Therefore, widths of signals appear to be narrower, and intensity of signals gets lower at higher DVs for all ions. Centerlines of CV maps were plotted in figure 4.5 for more clear comparisons of compensation voltages of different ions and each data point is put together

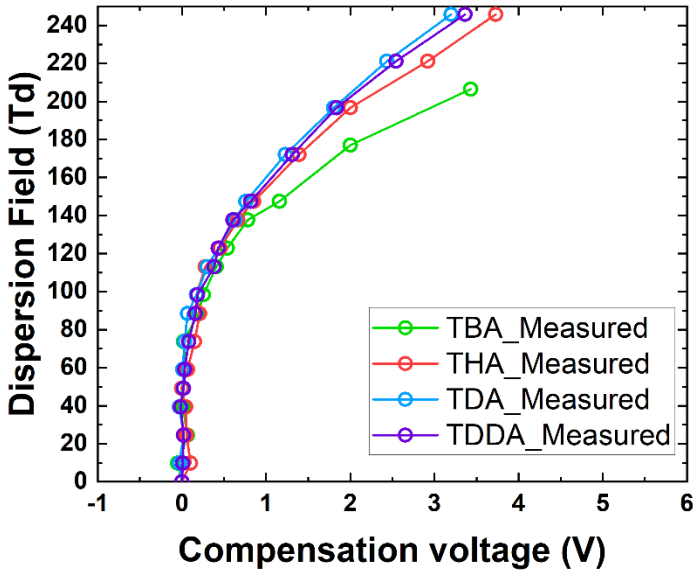

Figure 4.5 The extracted CV:DV spectra of monomer ions of TBAI, THAB, TDAB, and TDDAB.

in Table 4.1. All types of positively charged monomer ions transmitted through the FAIMS at positive compensation voltages with positive dispersion voltages. The raw data reported relative intensities of dispersion voltage and they were converted to actual field strength values (Townsend, 1 Td = 10^{-21}V m^{-2}) using maximum dispersion voltage of 214 V, gap distance of 35 μm, temperature of 295 K, and pressure of 1 atm. Under these measurement conditions, 100% dispersion voltage corresponded to 245.8 Td. Positive CVs contributed to increment of dispersion field strengths which compensated displacements caused by lower mobility at high field. According to these results, mobilities of tetraalkylammonium ions are confirmed to decrease at high electric field strengths. The same tendency was reported by previous studies (Aksenov et al., 2012, Aksenov and Kapron, 2010, Campbell et al., 2014) that tetraalkylammonium ions were detected at negative compensation voltages when negative dispersion voltages were used. The higher the mobility of ions at low field, the smaller dispersion voltage was required to observe the change of mobilities, and the larger compensation voltage was required to let ions drift through the FAIMS except tetra dodecyl ammonium ions. While $TDDA^+$ ion mobility is lower TDA^+ ion mobility, compensation voltages of $TDDA^+$ were larger than those of TDA^+.

Table 4.2 Estimated α values of TBA^+, THA^+, TDA^+, and $TDDA^+$ at 295 K and 1 atm. The maximum dispersion voltage applied was 214 V and the gap distance of the channel is 35 μm. The dimension of α_2 and α_4 is Td^{-2} and Td^{-4} respectively.

TBA		**THA**		**TDA**		**TDAA**	
$\boldsymbol{\alpha_2}$	$\boldsymbol{\alpha_4}$	$\boldsymbol{\alpha_2}$	$\boldsymbol{\alpha_4}$	$\boldsymbol{\alpha_2}$	$\boldsymbol{\alpha_4}$	$\boldsymbol{\alpha_2}$	$\boldsymbol{\alpha_4}$
-1.75E-06	-6.87E-11	-2.96E-06	1.17E-11	-1.40E-06	-2.45E-11	-2.24E-06	-4.06E-12

Each data point in table 4.1 was used for calculation of α_2 and α_4 using equation (4.14-17) and results are reported in table 4.2. For information on the waveform required for calculations, $\langle f_2 \rangle = 0.224$, $\langle f_3 \rangle = 0.108$, and $\langle f_5 \rangle = 0.105$ were used which were reported by (Shvartsburg et al., 2009). As expected from positive compensation voltages, most of α values are negative. The K_h can be calculated based on estimated α (truncated form with n=2) based on measured ion mobility (K_0) with the DMA directly before FAIMS measurements. Expected ion mobility in high field limit was plotted in figure 4.6. As expected, ion mobilities of tetraalkylammonium ions are decreasing as the field strength increases and TBA^+ shows most noticeable dependency followed by larger ions.

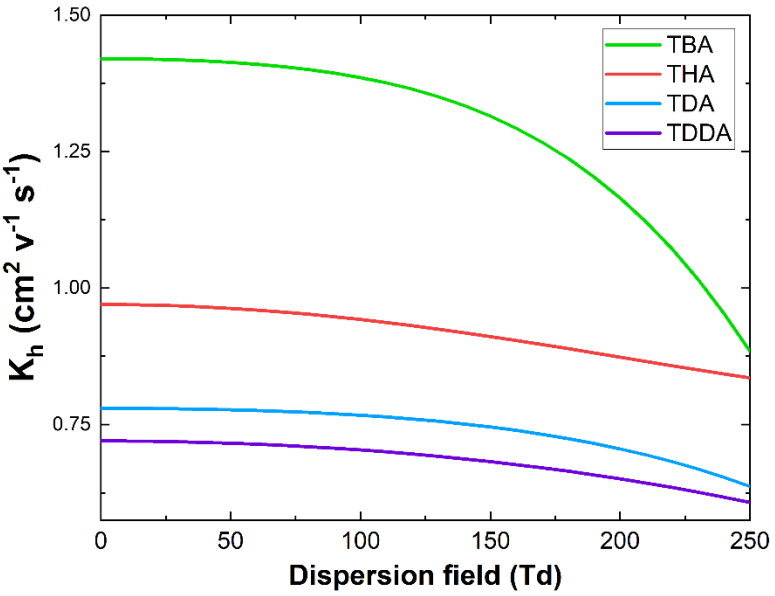

Figure 4.6 Expected K_h of TBA^+, THA^+, TDA^+, and $TDDA^+$ as function of dispersion field strength using the truncated form of α. $K_h = K_0(1 + \alpha_2(E/N)^2 + \alpha_4(E/N)^4))$

The inverse calculation is also available using equation (4.14) for compensation voltages from α and dispersion field strengths. The estimated compensation voltages from α

functions were plotted in figure 4.7 with measured compensation voltages. Calculations provided generous agreement with measured values when dispersion field strength is around 150 Td but with higher field strengths it deviated from measured data. This limitation has been discussed from previous studies (Wilks et al., 2012) that truncated form of α function is not sufficient to represent the mobility dependence at higher fields (>150 Td) and the higher order α terms are required for more accurate predictions at higher fields even for larger and stable ions which do not dissociate at high temperature.

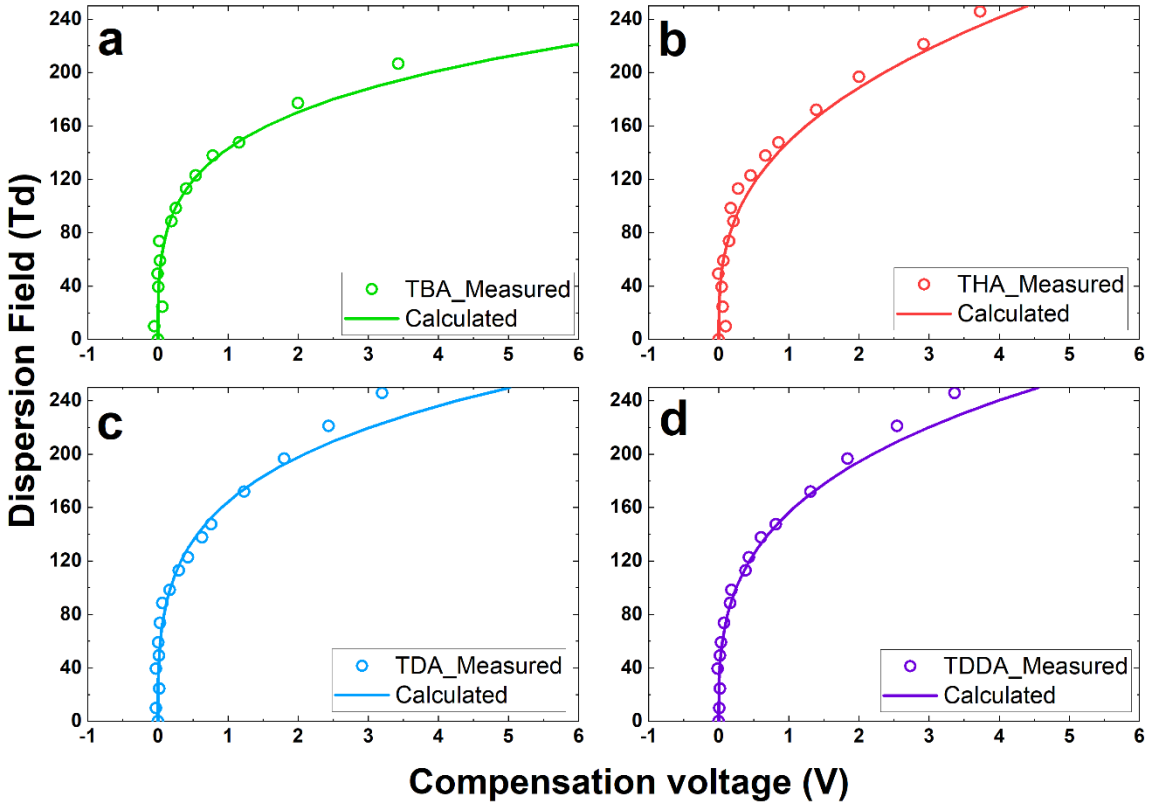

Figure 4.7 The measured compensation voltages and calculated compensation voltages using truncated from of α function of **(a)** TBA^+, **(b)** THA^+, **(c)**TDA^+, and **(d)** $TDDA^+$.

4.4 Conclusions

In this study, an ESI-DMA-FAIMS system was newly implemented to separate ions based on their constant ion mobility at low field strengths and their mobility dependence on the field strength at high field strengths. Monomer ions of tetraalkylammonium salts (from butyl to dodecyl) were successfully analyzed by an ESI-DMA-FAIMS system. The truncated α functions of TBA^+, THA^+, TDA^+, and $TDDA^+$ were calculated based on dispersion field strengths and compensation voltages. However, the resulting α functions with limited orders were not effective at higher field strengths than 150 Td. Since noticeable separation of CV spectra between 4 types of ions appears to require higher fields than 150 Td, the need for accurate α functions at higher fields was reassured. It has been known that higher order of α terms from equation (4.13-17) yields more precise prediction of ion mobility dependence. Different approaches solving equation (4.9) such as Twomey's algorithm (commonly used for inversion of aerosol measurement data) will provide a new path to higher order of α terms.

This study suggests that a DMA-FAIMS system can be a powerful tool for ion analysis utilizing separation based on two orthogonal properties and can expand the application area of low field IMSs. However, the resolution observed in this study due to the short channel lengths of ultra FAIMSs leaves space for improvement. The ion separation by FAIMS can be enhanced by modification of the carrier gas composition (addition of water, alkanes, alcohols, etc.) as shown in previous studies (Waraksa et al., 2016, Campbell et al., 2014, Wei et al., 2019, Rorrer and Yost, 2015, Rorrer and Yost, 2011) which utilized transient bindings between vapor molecules and ions. Therefore, the introduction of vapors to a

DMA-FAIMS system will not only improve the resolution of measurements but also enable higher dimensional analysis using only ion mobility based techniques.

Chapter 5. Computational Predictions of Porosities, Pore Size Distributions, and Conductivities of Aerosol Deposited Particulate Films

Adapted from: Jihyeon Lee, and Christopher J. Hogan Jr. "Computational predictions of porosities, pore size distributions, and conductivities of aerosol deposited particulate films." *Powder Technology* 378 (2021): 400-409.

Abstract: The structure and resulting physical properties of aerosol deposited particulate films are governed by the size distribution and morphology of the depositing particles as well as the physics governing particle deposition. While particulate film deposition processes are qualitatively understood, the link between particle characteristics and deposition physics to film properties has not been probed systematically. Here we apply a combination of Langevin dynamics deposition simulations, Monte Carlo pore size distribution calculations, and predictions of the thermal conductivities to better establish such process parameter-film property relationships. We account for partial coalescence, polydispersity, and aggregate deposition. We establish that the deposition of polydisperse and aggregated particles leads to broadening of the pore size distribution function and an increase in the mode pore size. Via a non-continuum gas conductivity model, we show that aerosol deposited films can achieve porosities and thermal conductivities similar to conventional aerogels.

5.1 Introduction

Aerosol deposition techniques (Adachi et al., 1988, Akedo, 2006, Hanft et al., 2015, Yang et al., 1999) are a suite of methods to manufacture submicrometer thin films as well

as thicker coatings, reliant on the physics of particle transport to surfaces, which is an integral topic in particle technology (Morgeneyer et al., 2019). In the past several decades there has been considerable development in aerosol deposition, and presently aerosol deposition techniques span from supersonic cold spray at both high and low pressure (Akedo and Lebedev, 2002, Suzuki et al., 2017, An et al., 2020, Huang et al., 2007, Li et al., 2019, Adamczyk et al., 2019, McCallister et al., 2021), to flame aerosol deposition both within flame reactors and post-flame (Thimsen and Biswas, 2007, Thimsen et al., 2008, Lee et al., 2016, Tricoli and Elmøe, 2012, Wegner et al., 2012, Tolmachoff et al., 2009, Zhang et al., 2012c), plasma deposition (Firth and Holman, 2018, Holman and Kortshagen, 2010, Greenberg et al., 2017, Thimsen et al., 2014, Koh and Gordon, 2013, Vulic et al., 2019, Beaudette et al., 2020b, Kubo et al., 2013, Schlag et al., 2020), and electrostatic deposition, including via electrosprays (Rusinque et al., 2019, Castillo et al., 2018, Higuera, 2018, Hogan and Biswas, 2008b, Tang and Gomez, 2017). Often the goal in utilizing supersonic deposition techniques is to drive particle restructuring and the formation of dense coatings (Exner et al., 2019, Lee et al., 2011, Adamczyk and Fuierer, 2018). Conversely, lower velocity deposition, or deposition of hard materials without substantial restructuring can be driven by fluid, electrostatic, or thermophoretic forces and leads to uniquely nanostructured coatings. Such coatings can be incorporated onto a variety of devices, such as solid oxide fuel cells (Erilin et al., 2020, Choi et al., 2011, Choi et al., 2012), solar cells (Zhu et al., 2013), and heat transfer surfaces (Jo et al., 2018). Nanostructured, particulate coatings also result from particle collection and measurement processes, including filtration (Novick et al., 1992), electrostatic precipitation (Huang and Chen, 2003), and resistive soot sensors (Maricq and Bilby, 2018, Fragkiadoulakis et al.,

2018), wherein the physical properties of coating ultimately affect how the collection or measurement system behaves (e.g. pressure drop in filters). It is therefore important to understand the factors governing the nanostructures of such coatings, and how the nanostructure affects their behavior.

In the absence of substantial restructuring (sintering and particle rearrangement during deposition; Baric et al., 2019), the nanostructure of an aerosol-deposited coating results from the manner in which particles are deposited onto the substrate, i.e. the structure is dependent upon the advective force, pressure, temperature, particle size, and particle shape. The macroscale structures of resulting films are often examined by surface profilers and microscopes, while submicroscale structures, such as nanopores, are typically examined by measuring the nitrogen or argon adsorption isotherm and via tomographic image analysis (Rouquerol et al., 2013, Appoloni et al., 2004). Simultaneously, there have been efforts to simulate particle deposition and to understand how the physics governing deposition affect the resulting nanostructure. The earliest simulations along these lines reveal that when stochastic particle motion is significant (Meakin, 1986, Tassopoulos et al., 1989), dendritic structures result. Later simulations, utilizing Brownian dynamics equations or Monte Carlo techniques (Kulkarni and Biswas, 2004, Ogunsola and Ehrman, 2008, Higuera, 2018), Langevin dynamics equations (Lindquist et al., 2014, Mädler et al., 2006, Nasiri et al., 2015), lattice simulations (Rodríguez-Pérez et al., 2005), and ballistic simulations (Chen et al., 2017, Hogan and Biswas, 2008b) all confirm that particulate deposits are highly porous (with porosities exceeding 0.9 in many instances), but with both the film nanostructure and resulting physical properties adjustable by adjusting process conditions. Despite considerable progress in this area, there remain open questions in

understanding and optimizing aerosol deposition for porous film production. First, with few notable exceptions (Mädler et al., 2006, Baric et al., 2019, Kulkarni and Biswas, 2003), simulations have examined exclusively monodisperse, spherical particle deposition, where particles remain in point contact upon deposition. Experimentally, this is never the case; particles are invariably polydisperse, often aggregated, and incompletely coalesce upon deposition. Second, film nanostructures have been largely described in prior work via the film porosity as a function of thickness (Lindquist et al., 2014), while of equal or greater interest is the pore size distribution (Bhattacharya and Gubbins, 2006), as this can strongly affect film properties. Third, also with few exceptions (Chen et al., 2017), simulations have typically not been extended to predict film properties from the resulting nanostructures. The purpose of the present study is to address these three issues by computing the structures of films formed via aerosol deposition of monodisperse, polydisperse, aggregated, and coalescing particles using Langevin dynamics simulations. Subsequently, the resulting pore size distributions of such films, and resulting film thermal conductivities at atmospheric pressure are computed. For the former, we adapt the framework of Lindquist et al. (2014) to non-monodisperse particles; in this framework deposition is carried out using dimensionless Langevin dynamics, which are dependent upon diffusive (mass transfer) Knudsen Number (Gopalakrishnan and Hogan, 2011) and a deposition kinetic energy to thermal energy ratio. For the latter, we examine a case study of SiO_2 nanoparticle deposition, developing a model for thermal conductivity accounting for non-continuum effects in the gas which takes the pore size distribution as an input. The model is modified from prior approaches used to predict the thermal conductivities of silica aerogels (Zeng et al., 1994), but with proper scaling for the thermal conductivity in free

molecular limit. The subsequent sections describe the equations utilized, the specific calculations performed, and results of calculations. Our overall goal in completing this study is to demonstrate how predictions of aerosol-deposited film properties can derive from simulations of their formation. Within the context of porous SiO_2 coatings, our calculations suggest that aerosol-deposited materials should have similarly low thermal conductivities to conventional aerogel materials (Bisson et al., 2004, Wei et al., 2011, Bi et al., 2014).

5.2 Computational methods

5.2.1 Film formation

5.2.1.1 Simulation parameters and particle equations of motion

Film deposition is simulated onto a flat substrate by placing particles at a z-location (height) 2.1 dimensionless radii above the highest point in the film. For simulations with single spheres the domain is 50 x 50 dimensionless radii in area, for aggregates the domain is 250 x 250 dimensionless radii in area, and in all situations periodic boundary conditions are invoked on the four vertical faces. In instances with polydisperse particles, the geometric mean radius is used for distance normalization and in the case of aggregates, normalization is based upon the radius of a primary particle within an aggregate. Particles move towards the substrate, driven by a constant advective force, with particle inertia and thermal (diffusive) motion also considered. Particle-particle and particle-substrate interactions are neglected in the present study. While they can certainly be incorporated into such simulations, in general, the transport of particles to a substrate or growing deposit surface is not strongly influenced by short range interactions (Kulkarni and Biswas, 2004).

Particles are stepped in time following dimensionless Ermak & Buckholtz (1980) solution to the Langevin equation, which is provided by Lindquist et al. (2014):

$$\overrightarrow{v_p}^*(\tau+\Delta\tau) = \overrightarrow{v_p}^*(\tau)\exp(-\Delta\tau) - \chi_F{}^{\frac{1}{2}} Kn_D \hat{k}[1-\exp(-\Delta\tau)] + \overrightarrow{A_1} \tag{5.1}$$

$$\overrightarrow{x_p}^*(\tau+\Delta\tau) = \overrightarrow{x_p}^*(\tau) + \left(\overrightarrow{v_p}^*(\tau+\Delta\tau) + \overrightarrow{v_p}^*(\tau) + 2\chi_F{}^{\frac{1}{2}} Kn_D \hat{k}\right)\left(\frac{1-\exp(-\Delta\tau)}{1+\exp(-\Delta\tau)}\right) - \chi_F{}^{\frac{1}{2}} Kn_D \hat{k}\Delta\tau + \overrightarrow{A_2} \tag{5.2}$$

$$\left\langle \overrightarrow{A_1}^2 \right\rangle = 3Kn_D^2[1-\exp(-2\Delta\tau)] \tag{5.3}$$

$$\left\langle \overrightarrow{A_2}^2 \right\rangle = 6Kn_D^2[\Delta\tau - 2(\frac{1-\exp(-\Delta\tau)}{1+\exp(-\Delta\tau)})] \tag{5.4}$$

where $\overrightarrow{v_p}^*$ is dimensionless velocity vector and $\overrightarrow{x_p}^*$ is dimensionless position vector at dimensionless time, τ and $\tau+\Delta\tau$. The dimensionless time step is also based on the Lindquist et al. (2014) criterion of $\Delta\tau = 0.04Kn_D^{-2}r_c^2 * \min(1, \chi_F{}^{-\frac{1}{2}})$, where r_c is the dimensionless minimum distance to deposited particles or to the substrate. Kn_D is the diffusive Knudsen number, defined as:

$$Kn_D = \frac{(kTm_p)^{1/2}}{fa_p} \tag{5.5}$$

where kT is the thermal energy, m_p is the particle mass, f is the particle friction factor, and a_p is the geometric mean particle radius. χ_F is the ratio of the translational kinetic energy to the thermal energy as:

$$\chi_F = \frac{m_p U_0^2}{kT} \tag{5.6}$$

with U_0 the particle advective velocity. $\overrightarrow{A_1}$ and $\overrightarrow{A_2}$ are Gaussian distributed random vectors with zero mean and variances are given by equation (5.3) and (5.4), respectively. In equations (5.1-5.4), all length scales are normalized by the primary particle radius (or geometric mean radius), while time is normalized by the ratio of the geometric mean

particle mass to geometric mean friction factor (i.e. the inertial relaxation time). The entire system evolution is hence dependent on the dimensionless variables Kn_D and χ_F. As noted previously (Hunt et al., 2014, Lindquist et al., 2014), these numbers can be combined to yield more traditional dimensionless ratios, i.e. $\chi_F{}^{\frac{1}{2}}Kn_D$ is proportional to most definitions of Stokes number, while $\chi_F{}^{\frac{1}{2}}Kn_D{}^{-1}$ is proportional to Peclet number (furthermore, χ_F is proportional to the square of the particle Mach number, i.e. particle velocity to the speed of sound in a gas composed of the particles). Any two from the group of diffusive Knudsen number, translational-thermal energy ratio, Stokes number, and Peclet number can be used to describe the behavior of systems subject to the Langevin equation of motion for non-interacting particles. We elect to utilize diffusive Knudsen number and translational-thermal energy ratio as we argue they are the most "orthogonal" in terms of their physical representation; diffusive Knudsen number is not dependent upon advective velocity and is a dimensionless representation of pressure (it is its inverse), while translational-to-thermal energy ratio is pressure independent.

For each film simulated, particles are introduced into the simulation domain sequentially, with each particle allowed to deposit prior to the introduction of the next particle (the dilute limit approximation). We investigate monodisperse spherical particles depositing in point contact (i.e. sticking upon encountering the substrate or previously deposited particles), monodisperse spherical particles with a prescribed degree of coalescence upon deposition, polydisperse spherical particles depositing in point contact, and quasifractal aggregates composed of monodisperse particles depositing in point contact. For instances with single spherical particles, 3.5 x 10^4 particles are deposited to construct

particulate film geometries; with aggregate deposition 2.0 x 10^5 primary particles are deposited (2.0 x 10^3 – 10^5 aggregates).

5.2.1.2 Coalescence

The movement of each particle is terminated when the particle has a point contact with one of the deposited particles or with the substrate, as shown in Figure 5.1. To investigate the effect of coalescence of particles, we adjust the distance between two particles after deposition. As depicted in figure 5.1, primary particle "*a*" is already deposited and incorporated into the particulate film, while primary particle "*b*" is part of the moving particle which came into contact with particle "*a*". Without considering coalescence, the distance between these two neighboring particles at deposition is defined as the sum of their radii, $a_a + a_b$. However, coalesce reduces this distance and correspondingly increases the radii of the particles. We prescribe a coalescence ratio, θ, which is the fractional reduction in radius and determines the overlapped volume of the two particles, *dV*. For simplicity, we elect to increase only the size of particle "*b*" to a value $a_{b,new}$ due to coalescence at deposition, using the following relationships:

$$dV = \frac{\pi}{3}\left(\frac{\theta(a_a+a_b)}{2}\right)^2 (3a_a + 3a_b - \theta(a_a + a_b)) \tag{5.7a}$$

$$\frac{4}{3}\pi a_a^3 + \frac{4}{3}\pi a_b^3 + dV = \frac{4}{3}\pi a_a^3 + \frac{4}{3}\pi a_{b,new}^3 \tag{5.7b}$$

$$\frac{4}{3}\pi a_b^3 + dV = \frac{4}{3}\pi a_{b,new}^3 \tag{5.7c}$$

Through equations (5.7a-c), coalescence is assumed to occur to a finite extent, but on an infinitely fast timescale in comparison to time scale for particle transport to the substrate surface. This assumption would apply for a dilute system (i.e. an aerosol) and for

temperatures well below the bulk melting temperature of the depositing material. The effect of coalescence ratios of 0.0, 0.1, 0.2, and 0.3 are reported on in the *Results & Discussion* section.

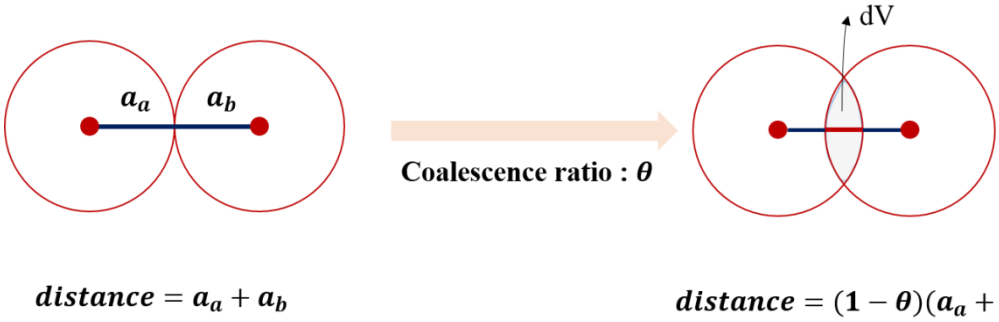

Figure 5.1 A description of coalescence between particles for a defined coalescence ratio (θ) level, yielded the volume dV.

5.2.1.3 Polydispersity

To examine the influence of particle polydispersity on particulate film structures, each particle radius is sampled from a lognormal distribution whose geometric standard deviation (GSD) is 1.05, 1.1, 1.2, 1.3, or 1.4. The geometric mean is a dimensionless value of 1.0 in all cases. Randomly generated radii are rounded to the nearest tenth to facilitate subsequent application of the pore size analysis algorithm, requires a finite number of discrete particle radius values. Input values, Kn_D and χ_F are calculated based on geometric mean radius; thus, when solving the particle equations of motion we introduce specific $Kn_{D,S}$ and $\chi_{F,S}$ as shown in equation (5.8a-b; where "S" denotes a specific sampled particle) and adjust equations (5.1-5.4) such that they apply to the sampled particle.

$$Kn_{D,S} = \frac{Kn_D}{\sqrt{a_{p,s}}} \frac{(1+Kn_S(1.257+0.4*exp\,(\frac{-1.1}{Kn_S})}{(1+Kn(1.257+0.4*exp(\frac{-1.1}{Kn}))} \quad (5.8a)$$

$$\chi_{F,S} = \chi_F a_{p,s}^3 \quad (5.8b)$$

where $a_{p,s}$ the dimensionless radius of a specific sampled particle, and Kn and Kn_S are Knudsen numbers based on the geometric mean radius and a specific radius respectively. For these instances, we specifically utilize Kn of 1.0, which is an input parameter.

5.2.1.4 Aggregate deposition

Aggregates are generated by the sequential algorithm (SA) where a spherical particle is attached to an aggregate iteratively satisfying the relation as follows:

$$N = k_f(\frac{R_g}{a_p})^{D_f} \tag{5.9}$$

where N is the number of primary particles per aggregate, k_f is pre-exponential factor, R_g is the radius of gyration, a_p is particle radius (identical for each particle), and D_f is the fractal dimension. Aggregate generation by SA is described in detail by Filippov et al. (2000). While this algorithm does not successfully recover the properties of larger aggregates with more than 100 primary particles, it is a simple approach to generate structures satisfying equation (5.9) with lower numbers of primary particles (i.e. fewer than 100). We examine chain-like aggregates (with lower $D_f = 1.8$ and $k_f = 2.0$) and dense aggregates (with higher $D_f = 2.5$, $k_f = 2.0$); example structures are depicted figure 5.2. In the aggregate deposition process, Kn_D and χ_F are the values for an aggregate (i.e. based on the aggregate mass and friction coefficient, but normalized with primary particle radius). Equations (5.1-5.4) require no adjustment to apply to aggregates with normalization in this manner. The same aggregate geometry is applied for prescribed conditions, but each aggregate is rotated randomly in advance of its placement on its initial coordinate.

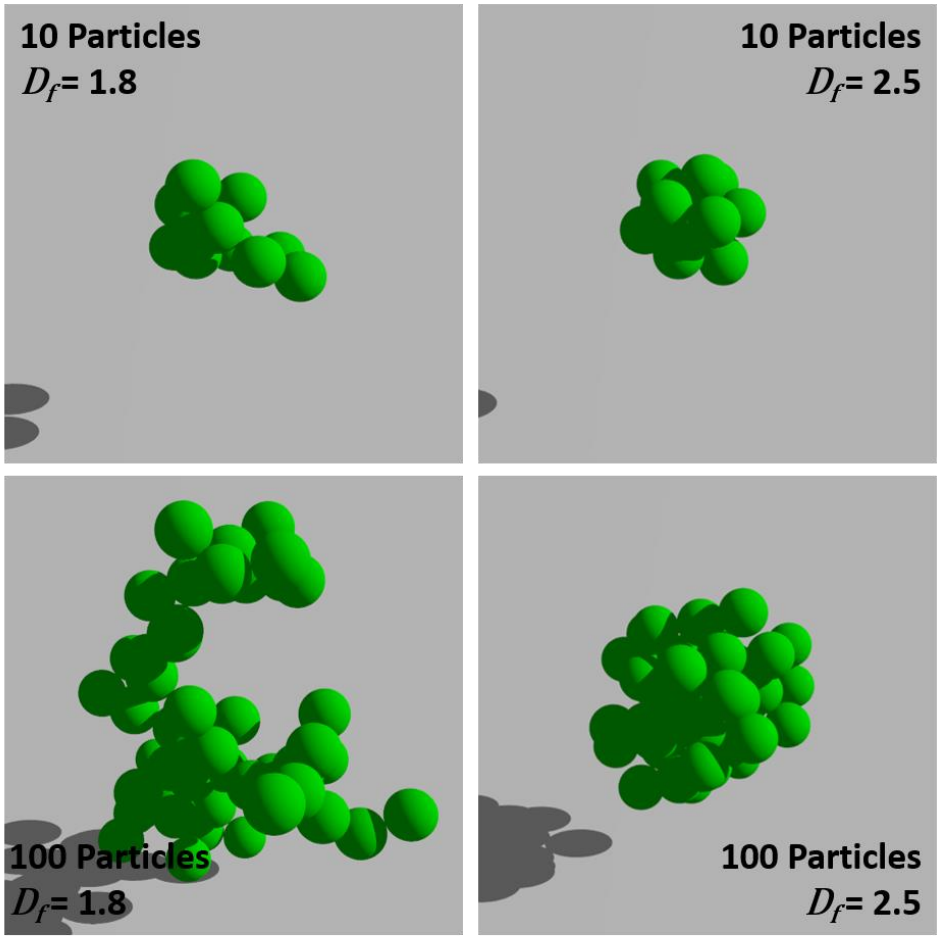

Figure 5.2 Depictions of aggregates at different numbers of primary particles and fractal dimensions.

5.2.1.5 Cases Examined

Monodisperse particles without coalescence and aggregation were deposited first under different Kn_D and χ_F conditions. Lindquist et al. (2014) showed that the porosity of the films resulting in these circumstances is determined by Kn_D and χ_F. In our study, 12 Kn_D, χ_F pairs were selected to generate films with porosities from 0.85 to 0.91. Second, monodisperse particles with variable coalescence ratios from 0.10 to 0.30 were deposited under with identical $Kn_D = 10$ and $\chi_F = 100$. Third, polydisperse particles with variable geometric standard deviations from 1.05 to 1.4 were deposited under the constant $Kn_D =$

10 and $\chi_F = 100$ condition. Finally, chain-like aggregates with D_f as 1.8 and dense aggregates with D_f as 2.5 were generated with the number of primary particles per aggregate in range of 2 to 100 (under the same $Kn_D = 10$ and $\chi_F = 100$ condition). We note that two primary particles is a constrained geometry, which was only examined once. All conditions are summarized in Table 5.1. Film deposition simulations resulted in the Cartesian coordinates and radii for the deposited primary particles, with the total number of particles deposited noted earlier in this section. We remark that the $Kn_D = 10$ condition applies for sub-10 nm particles at atmospheric pressure (or larger particles at reduced pressure), and $\chi_F = 100$ applies for a strong advective forcing velocity relative to the thermal velocity. It is specifically selected as χ_F in this range are encountered in recently developed and discussed aerosol deposition systems used in producing porous Si, ZnO and metal nanoparticle coatings (Firth and Holman, 2018, Vulic et al., 2019, Atkinson et al., 2020, Beaudette et al., 2020a). We also again note that the deposition process discussed neglects the effects of film rearrangement during or after deposition (i.e. compaction (Morgeneyer et al., 2008) is not studied). Such effects would need to be considered to develop links between deposition conditions, film structure, and film properties for thicker films (>10^3 particle radii in thickness).

Table 5.1 The summarization of conditions for each case examined.

Case	Area	$\mathbf{Log_{10}(Kn_D)}$	$\mathbf{Log_{10}(\chi_F)}$	$\boldsymbol{\theta}$	GSD	$\boldsymbol{D_f}$	$\mathbf{N_p}$
1	50×50	1	2	0	1	-	-
2	50×50	0	2	0	1	-	-
3	50×50	-1	0.3	0	1	-	-
4	50×50	-1.25	-0.5	0	1	-	-
5	50×50	-3	-4	0	1	-	-
6	50×50	-2	-2	0	1	-	-
7	50×50	-1.5	-2.2	0	1	-	-

8	50×50	-2	-3.2	0	1	-	-
9	50×50	-2.4	-4	0	1	-	-
10	50×50	-0.7	-1.4	0	1	-	-
11	50×50	-2	-4	0	1	-	-
12	50×50	-1.5	-3	0	1	-	-
13	50×50	1	2	10	1	-	-
14	50×50	1	2	20	1	-	-
15	50×50	1	2	30	1	-	-
16	50×50	1	2	0	1.05	-	-
17	50×50	1	2	0	1.10	-	-
18	50×50	1	2	0	1.20	-	-
19	50×50	1	2	0	1.30	-	-
20	50×50	1	2	0	1.4	-	-
21	250× 250	1	2	0	1	1.8	2
22	250× 250	1	2	0	1	1.8	5
23	250× 250	1	2	0	1	1.8	10
24	250× 250	1	2	0	1	1.8	20
25	250× 250	1	2	0	1	1.8	50
26	250× 250	1	2	0	1	1.8	100
27	250× 250	1	2	0	1	2.5	5
28	250× 250	1	2	0	1	2.5	10
29	250× 250	1	2	0	1	2.5	20
30	250× 250	1	2	0	1	2.5	50
31	250× 250	1	2	0	1	2.5	100

5.2.2 Pore analysis

5.2.2.1 Packing fraction

As investigated previously in aerosol deposited films (Mädler et al., 2006, Nasiri et al., 2015), porosity is a clearly quantifiable film characteristic, defined the ratio of the void volume to the total volume of the film. The porosity of a particulate film can be calculated by coordinates and radii of deposited particles. We quantify in here through determine of the packing fraction (ρ), or 1-porosity, was calculated at each dimensionless height of the film, z^*:

$$\rho(z^*) = \lim_{dz^* \to 0} \frac{\sum_{i=1}^{N} V_i(z^* \to z^* + dz^*)}{A^*_{tot} * dz^*} = \frac{\sum_{i=1}^{N} A_i(z^*)}{A^*_{tot}} \tag{5.10}$$

where dz^* is the small increment of dimensionless height, N is the number of particles, V_i is the volume of particle i between z^* and $z^* + dz^*$, A^*_{tot} is the total area of the film (2500 dimensionless units), and $A_i(z^*)$ is the cross section area of particle i at z^*. If dz^* is infinitesimal, the packing fraction can be approximate by the area fraction as shown in equation (5.10).

5.2.2.2 Pore size distribution

Directly linked to porosity and containing additional information is the pore size distribution (PSD), i.e. the volumetric density function of pore radius as a function of pore radius. The Brunauer-Emmett-Teller (BET) method (Brunauer et al., 1938), Barret-Joyner-Halenda (BJH) method (Barrett et al., 1951), and density functional theory (DFT) approach (Seaton and Walton, 1989) are the most common approaches to determine the PSD. Gelb & Gubbins (1999) developed a model to determine PSD for computationally described structures where the maximum pore radii are sampled by a probe particle. The maximum pore radius at a certain point is defined as the radius of the largest sphere that encompasses the void volume without overlapping any solid portion. $V_{pore}(a_{pore})$ is the coverable void volume by spheres which have radius a_{pore} or smaller. Therefore, PSD can be defined $P(a_{pore})$ as:

$$P(a_{pore}) = -\frac{dV_{pore}(a_{pore})}{da_{pore}} \tag{5.11}$$

Bhattacharya and Gubbins (2006) developed a FORTRAN code PSDsolv for fast calculation of PSD based on this algorithm. We use this code here to determine the PSDs of all simulated films, to understand how deposition physics influence the PSD.

5.2.3 Thermal conductivity

Beyond the link between deposition physics and structural properties is the link between structural properties and film performance. To examine how structure governs performance with the context of aerosol-deposited porous films, we develop and apply a model of thermal conductivity for porous particulate structures. In porous structures with gas within the pores, the gas thermal conductivity differs from the bulk thermal conductivity in free space because pores (which are smaller than the thermal mean free path of gas molecules) restrict the motion of gas molecules. Through a mass transfer analogy and functionally proposing an expression similar to Fuchs (Fuchs and Sutugin, 1970) and Dahneke (1983) for non-continuum mass transfer rates, the gas effective thermal conductivity in a pore, $K_{gas,\,pore}$ can be determined by the equation:

$$K_{gas,\,pore} = K_{gas,\,0}\left(\frac{1+A'Kn_T}{1+B'Kn_T+C'Kn_T^2}\right) \tag{5.12}$$

where $K_{gas,\,0}$ is the gas standard thermal conductivity in the free space, Kn_T is the thermal Knudsen number and A', B', and C' are constants depending upon the gas and solid network material. Kn_T, distinct from the mass transfer (Kn_D) and momentum transfer (Kn) Knudsen numbers, is most easily defined from the ratio of the continuum (Fourier) heat transfer rate to the free molecular (ballistic) heat transfer rate:

$$Kn_T = \frac{continuum\ rate}{Free\ molecular\ rate} = \frac{K_{gas,0}a_{pore}}{c_p\rho_{gas}\xi a_{pore}^2\overline{c}_{gas}} = \frac{\alpha}{\xi\sqrt{\frac{kT}{m_{gas}}}a_{pore}} \tag{5.13}$$

where a_{pore} is the pore radius, c_p is the gas specific heat capacity, ρ_{gas} is the gas mass density, $\overline{c}_{gas}$ is the gas mean thermal speed, α is the gas thermal diffusivity, ξ is the energy transfer accommodation coefficient (0 to 1, and depending upon the gas molecule and material), k is Boltzmann's constant, T is the temperature, and m_{gas} is the gas molecular

mass. To then account for a polydisperse distribution of pore radii, we first define a normalized PSD, $P'(a_{pore})$ such that:

$$\int_0^\infty P'(a_{pore})\, da_{pore} = 1 \tag{5.14a}$$

The total cross-sectional area occupied by pores, $A_{pore,tot}$ can be written as:

$$A_{pore,tot} = \pi \int_0^\infty P'(a_{pore}) a_{pore}^2\, da_{pore} \tag{5.14b}$$

The heat flow per unit temperature gradient through pores can be described as follows:

$$A_{pore,tot} K_{gas,eff} = \pi \int_0^\infty P'(a_{pore}) a_{pore}^2\, K_{gas,\,pore} da_{pore} \tag{5.14c}$$

Hence, we can define the gas effective thermal conductivity, $K_{gas,eff}$ as:

$$K_{gas,eff} = K_{gas,0} \frac{\int_0^\infty \left[P'(a_{pore}) a_{pore}^2 \left(\frac{1 + A' \left(\frac{\alpha \sqrt{\frac{m_{gas}}{kT}}}{a_{pore}} \right)}{1 + B' \left(\frac{\alpha \sqrt{\frac{m_{gas}}{kT}}}{a_{pore}} \right) + C' \left(\frac{\alpha^2 m_{gas}}{kT a_{pore}^2} \right)} \right) da_{pore} \right]}{\int_0^\infty [P'(a_{pore}) a_{pore}^2 da_{pore}]} \tag{5.15}$$

What remains is to determine the constants A', B', and C', which may depend upon gas and material combination. For SiO_2 particles in air fitting to the data presented by Zeng et al. (1994) we arrive at A'= 7.98, B'=9.52 and C'=3.42 (with fitting shown in Figure 5.3).

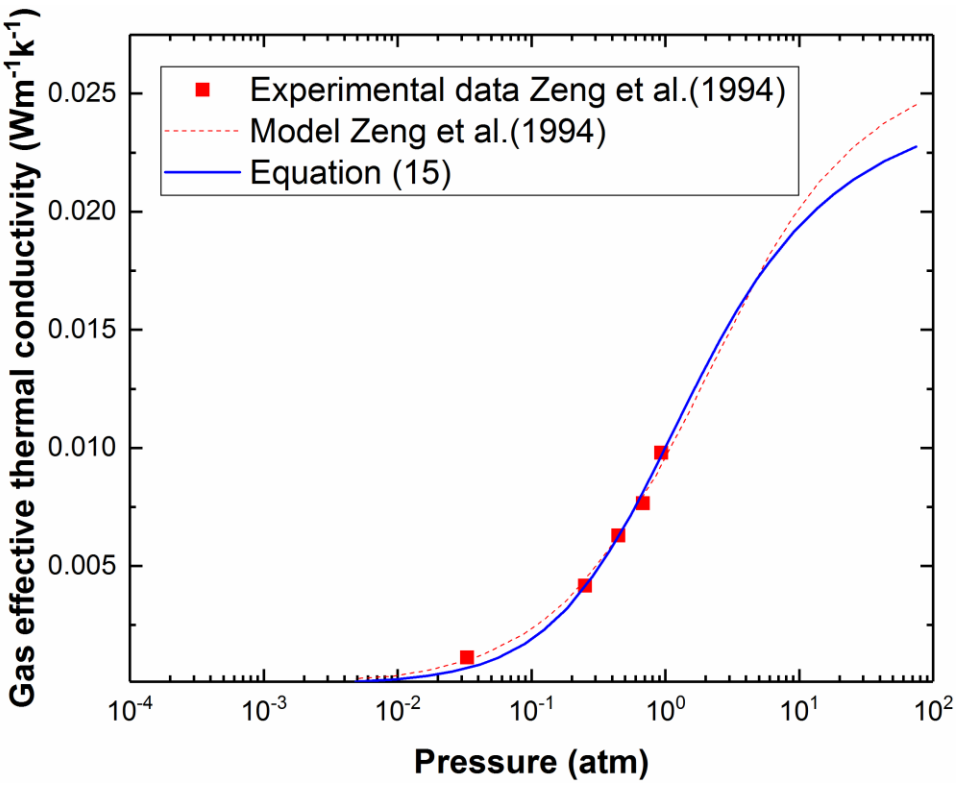

Figure 5.3 The fitting of the gas effective thermal conductivity model described in equation (5.15) to experimental results of Zeng et al. (1994)

We remark that Zeng et al. (1994) also present their own theory for non-continuum heat transfer in porous (aerogel) media. However, their proposed expression does not yield correct thermal Knudsen number scaling in the high thermal Knudsen number (ballistic) limit (Kn_T^{-1} dependence), hence our choice to redevelop this model. With $K_{gas,eff}$, the total effective conductivity of the film, $K_{tot,eff}$ can be estimated by the effective medium approximation of Landauer (1952):

$$K_{tot,\,eff} = \frac{1}{4}\left\{(3[1-\varphi]-1)K_s + (3\varphi-1)K_{gas.eff} + \left\{\left((3[1-\varphi]-1)K_s + (3\varphi-1)K_{gas.eff}\right)^2 + 8K_sK_{gas.eff}\right\}^{\frac{1}{2}}\right\} \tag{5.16}$$

where φ is porosity and K_s is the thermal conductivity of solid material. We remark that as the porosity approaches unity, if the particulate network is percolated, equation (5.16) will not yield accurate conductivity estimations. However, we believe this does not become a major issue in calculations until $\varphi > 0.99$ or the pressure is substantially reduced. To both examine the effective conductivity of porous films and to validate the use of equation (5.16), in the *Results & Discussion* section we compare to the SiO_2 aerogel thermal conductivity measurements of Bisson et al. (2004), Wei et al. (2011), and Bi et al. (2014) .

5.3 Results and Discussion

5.3.1 The structure of films

We first present depictions of the resulting porous structures in computations, followed by discussion of their porosities and PSDs. Figures 5.4 (a-i) contains side view depictions of the deposited films at variable conditions: (a-c) at variable coalescence ratios, (d-f) at different geometric standard deviations, and (g-i) at variable aggregate sizes. Similar to the depictions in Lindquist et al. (2014), the films are visibly porous, even at the high coalescence ratios examined, and apparently more porous for the polydisperse deposited particles of large geometric standard deviation distribution. For quantitative analysis, the packing fractions $\rho(z^*)$ and PSDs are displayed in figure 5.5. First, focusing on monodisperse, non-coalescing particles (figures 5.5a & 5.5b), results are shown for films deposited at 12 combinations of Kn_D and $\chi_F$which can be placed into 4 groups; the combinations displayed in red are films with the maximum packing fraction (minimum porosity) achievable by the single particle deposition model (as discussed by Lindquist et

al. (2014)) and the others in orange, yellow, and green are grouped to have the identical Peclet numbers of 10, 2.5, and 1 respectively. Consistent with the results of Lindquist et al. (2014), different Kn_D, χ_F combinations lead to films with different packing fractions: the packing fractions of red, orange, yellow and green films are 0.151, 0.127, 0.106 and 0.085 respectively, within the bulk of deposited film.

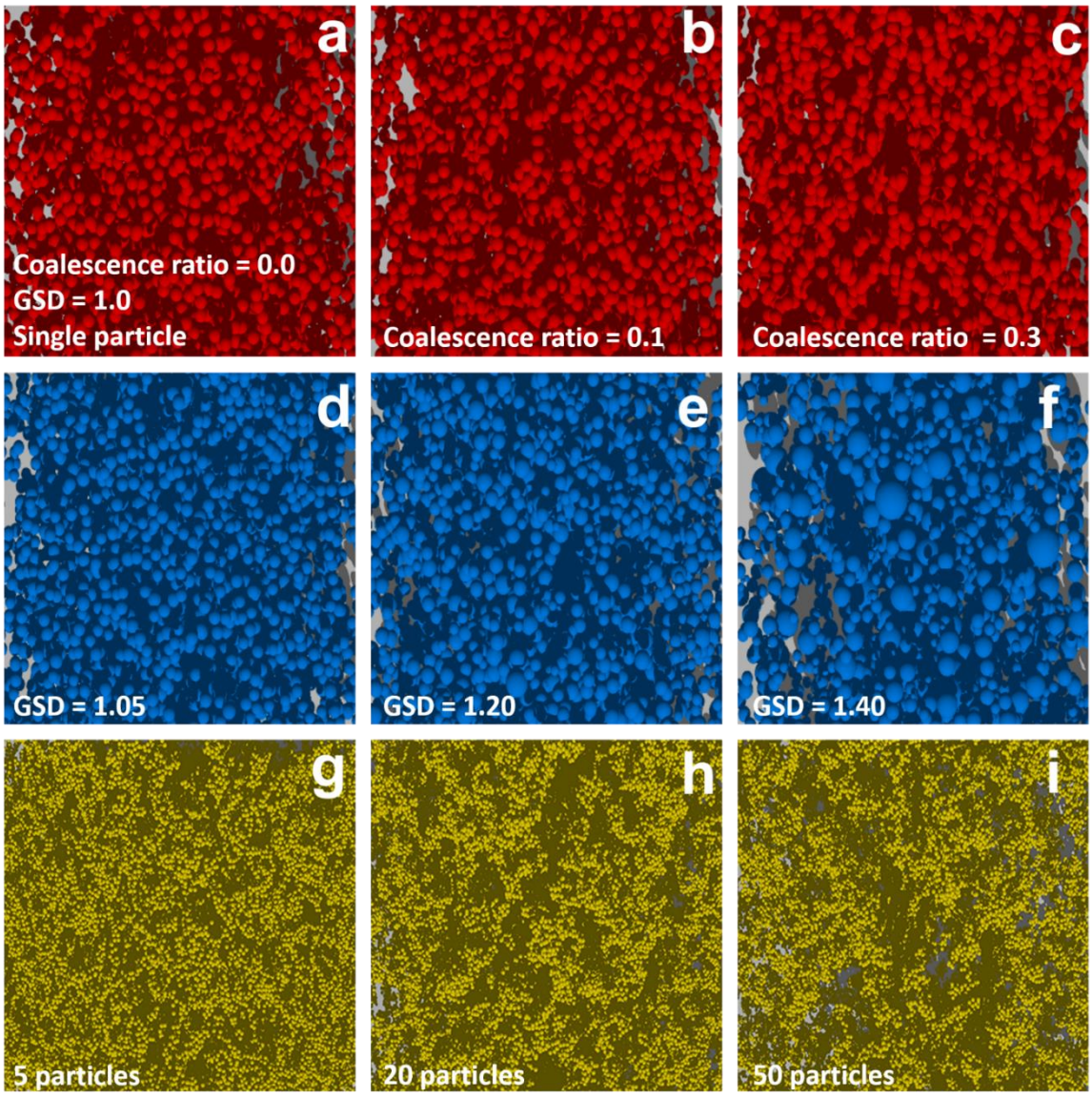

Figure 5.4 Side-view depictions of film morphologies under the fixed Kn_D=10, χ_F=100 conditions for different levels of coalescence **(a-c)**, polydispersity **(d-f)** and aggregation **(g-i)**. 35,000 particles were deposited on a 50×50 (particle radii) area for the singular particle deposition and 200,000 particles were deposited on a 250×250 area for the aggregate deposition. In each view, the substrate is at the bottom of the image.

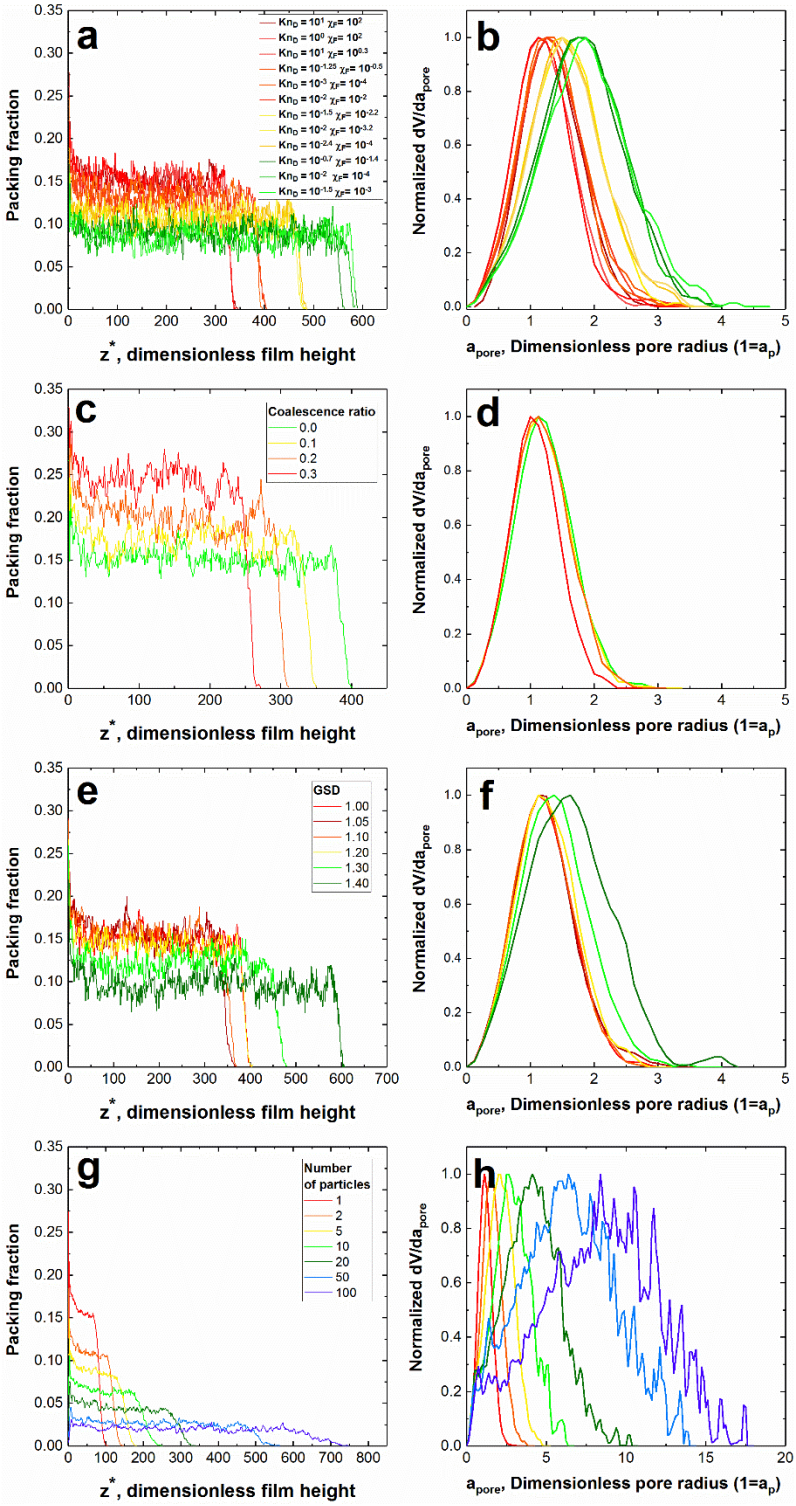

Figure 5.5 Packing fraction (1 – Porosity) and pore size distribution for different Kn_D and χ_F combinations **(a,b)** and different levels of coalescence **(c,d)**, polydispersity **(e,f)** and aggregation **(g,h)** under the fixed Kn_D =10, χ_F =100 conditions. The pore radius was normalized by the particle radius (a_p).

Interestingly, films within each group display almost identical pore size distributions, suggesting that the pore size distribution is almost completely determined by the film porosity. Subsequently, the $Kn_D = 10$ and $\chi_F = 100$ pair, which yields a 0.151 packing fraction for monodisperse particle deposition was selected as the standard condition to investigate the effect of other parameters: coalescence ratio, GSD of polydisperse particles, and the size of aggregates. Increasing the coalescence ratio (figure 5.5c & 5.5d) unsurprisingly yields denser films than the non-coalescing case; the packing fraction increased up to 0.246 at $\theta = 0.30$ and the pore size distribution narrows. When the GSD of particles (figures 5.5e & 5.5f) is increased to 1.05 and 1.1, the packing fraction slightly increases, but subsequently decreases with further increase in polydispersity. When the GSD reaches 1.4, the packing fraction decreases to 0.097 with a broader PSD peaked at a larger pore size. Finally, aggregate deposition is found to yield much more porous films whose packing fraction are lower than 0.05, and pore size distributions are significantly broader than those of denser films.

In general we find that increasing the coalescence ratio decreases porosity and narrows the PSD, while the deposition of polydisperse particles and aggregates largely increases film porosity and broadens the PSD, with the PSD mode shifting to larger pore radii. Figure 5.6 displays pore size distribution of all 31 films deposited under the conditions summarized in Table 5.1. The porosity of each case is represented colorimetrically. We find a direct correlation between PSD and porosity for all films; for nearly all films higher porosity correlates with an increase in PSD polydispersity, and mode pore radius. The densest films examined have PSDs peaked near dimensionless pore radii

of 1.0, suggesting that even with coalescence, in porous particulate films pore radii of similar size to the particles comprising films are expected.

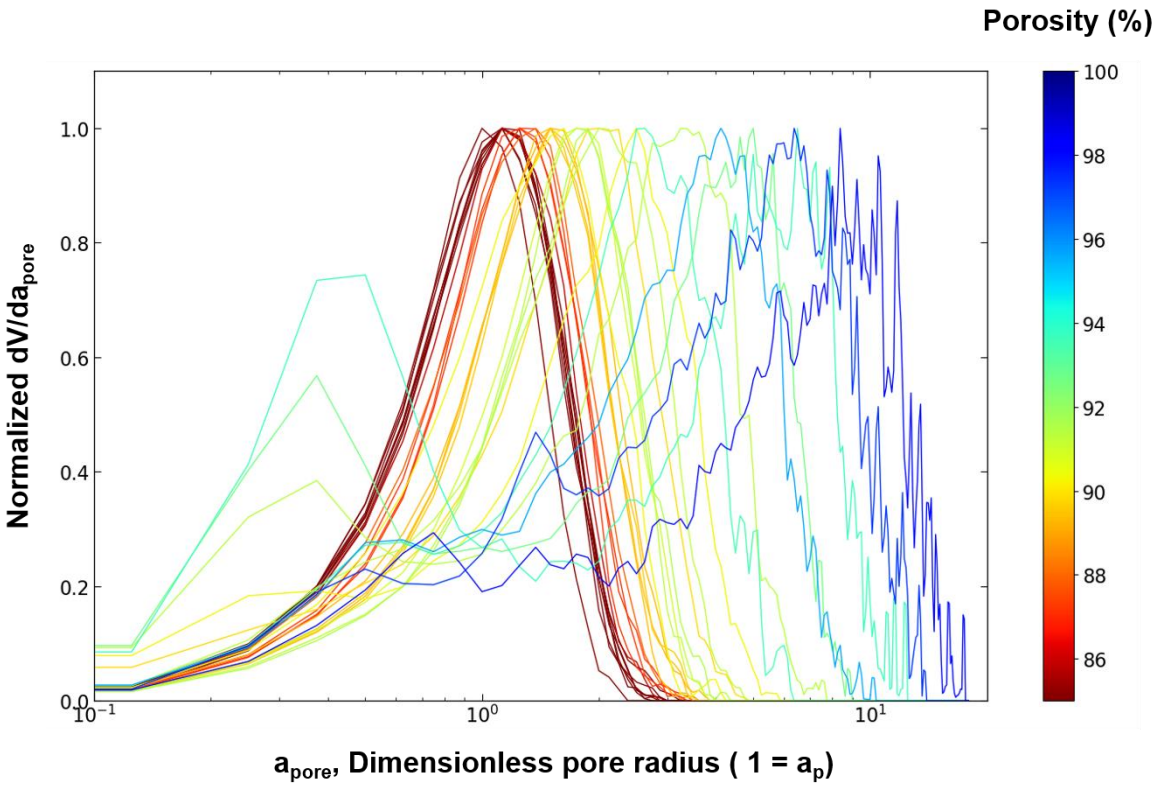

Figure 5.6 Pore size distributions at variable porosity, which is denoted via a color scale.

Interestingly, bimodal PSDs result from the deposition of aggregates with high fractal dimension (2.5). While there is noticeable "noise" in such PSDs, we find that this is the result of the need to discretize particle radii to specific values for PSD calculation, while the bimodal nature of these distributions is not the result of discretization or statistical uncertainty. Instead, such smaller pores, well below the primary particle radius, are present in the dense aggregates themselves, and hence remain present in films. We suggest that dense aggregate deposition is a method to produce bimodal PSD structures, with larger pore size distributions determined by aggregate-aggregate contacts and smaller pore sizes determined by individual aggregate structure.

5.3.2 Thermal Conduction in films

While validation of calculations would be ideally accomplished by comparison of experimentally evaluated film microstructures to those quantified here, systematic experimental studies of aerosol deposited particulate films have not yet been carried out. Instead, the bulk properties of films and porous particulate structures are more commonly reported. For comparison to such results, the gas effective thermal conductivity, $K_{gas,eff}$ is calculated for 31 films using equation (5.15). The PSDs based on dimensionless pore radius are converted into dimensional pore size distributions with variable primary particle radii assumed. $K_{gas,eff}$ is plotted as a function of porosity in figure 5.7 for air at atmospheric pressure and 300 K. $K_{gas,eff}$ increases both with increasing porosity and with the size of primary particles; both yield larger pores and corresponding smaller thermal Knudsen numbers. At the same time, two branches are seen at each particle size in figure 5.7, implying that the gas effective thermal conductivity can be varied at the same porosity. Branching is brought about by 5 data corresponding to dense aggregates and biomodal PSDs. The second mode radius of the bimodal distribution is greater than the mode radius of the unimodal pore size distribution at the same porosity, leading to a higher gas effective thermal conductivity.

While Figure 5.7 predictions are based on model results where the gas conductivity is parameterized by the data presented in Zeng et al. (1994), such predictions do require further validation. To do so, we remark that our results suggest a strong link between porosity and PSD, which likely extend beyond aerosol deposited films to more traditional aerogel synthesis approaches. We therefore compare model predictions to measurements of SiO_2 aerogel thermal conductivities. For comparison, the total effective thermal

conductivity for every film is evaluated with equation (5.16), with 1.1 W $m^{-1}K^{-1}$ applied as the thermal conductivity of SiO_2 particles.

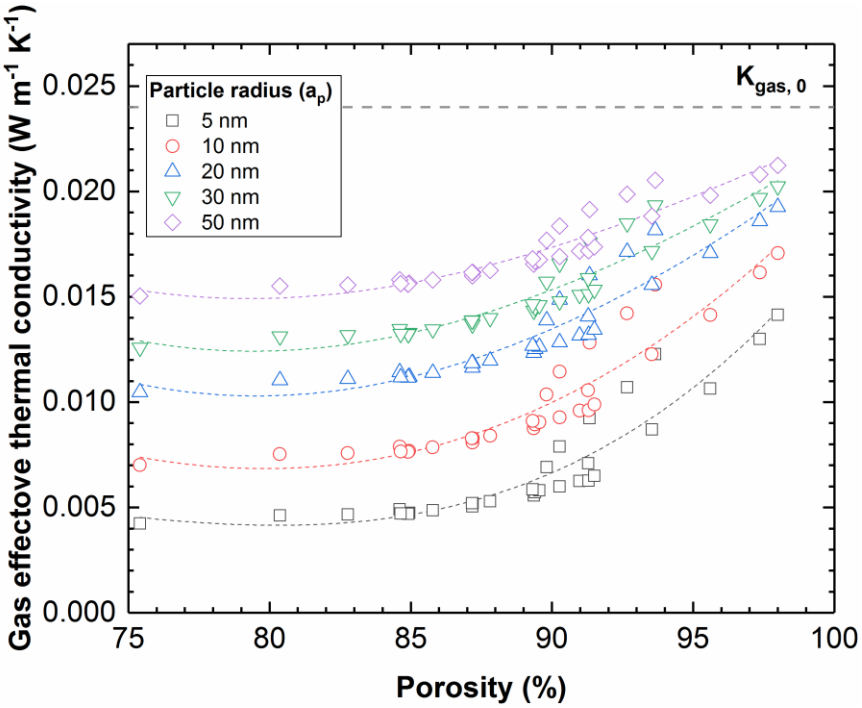

Figure 5.7 Effective gas thermal conductivity ($K_{gas,eff}$) in porous films with different radii of primary particles at variable porosity. The colored dashed lines are polynomial best fit guidelines, and the black dashed line is the gas standard thermal conductivity at 300 K, 0.024 W m^{-1} K^{-1}.

The calculated conductivities are shown in figure 5.8, alongside the experimental data of Bisson et al. (2004), Wei et al. (2011), and Bi et al. (2014). Strong agreement between predicted and measured conductivities is obtained for primary particle radii in the ~10 nm, which are typical values for aerogel primary particles. Interestingly, results suggest that thermal conductivity in aerogel-like materials and aerosol deposited porous films is minimized in the 0.85-0.90 porosity range; as porosity further increases, larger pore sizes increase the thermal Knudsen number and the gas effectivity conductivity, while lower porosity of course increase the concentration of higher conductivity SiO_2 particles. In total, modeling results suggest that conductivity minimization is best achieved by

minimizing the primary particle size for films of porosities in the 0.85-0.90 range. Such porosities are attainable in aerosol deposition at multiple different input conditions (Kn_D, χ_F, for polydisperse, aggregated and coalescing particles), and results further suggest that aerosol deposited films with thermal properties akin to aerogels can be produced.

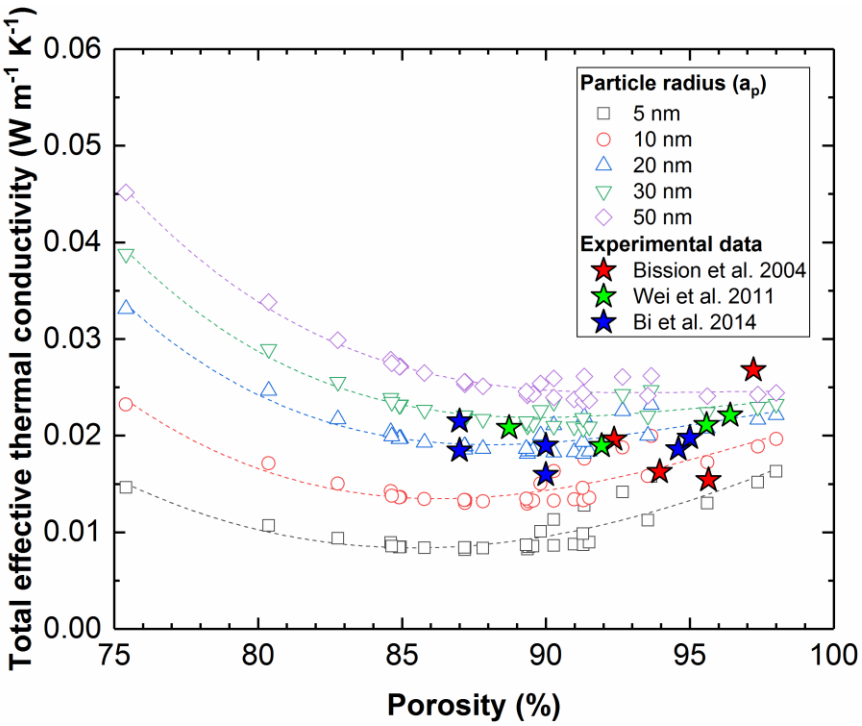

Figure 5.8 Effective total thermal conductivity ($K_{tot,eff}$) of films with different radii of primary particles at variable porosity. The colored dashed lines are polynomial fit guidelines.

5.4 Conclusions

We utilize Langevin dynamics simulations to examine the structures of aerosol deposited films, considering particles of varying degrees of coalescence, variable polydispersity, and variable extents of aggregates. Resulting film structures are parameterized in terms of porosity and pore size distribution, and subsequently pore size distributions are used to predict the thermal conductivities of the gas (air at atmospheric

pressure and 300 K) within the pores of the film, and the net film thermal conductivity. The model for gas conductivity variation is parameterized using results of aerogel measurements, and by construction correctly yields the bulk thermal conductivity at low thermal Knudsen number, and the proper scaling between thermal conductivity and pore radius and thermal Knudsen number expected at high thermal Knudsen number (a Kn_T^{-1} dependence, which is similar to the Kn^{-1} and Kn_D^{-1} observed for the effective friction coefficient and diffusion coefficient observed for momentum and mass transfer, respectively, at high Knudsen numbers). Such calculations provide a more complete picture on how film deposition process parameters lead to observed film structure and corresponding film performance than previously available. Based on the presented model and calculations, we make the two concluding remarks and suggestions.

For aerosol deposited films, pore size distribution is strongly determined by porosity, and in general the larger the porosity, the larger the mode pore radius and the broader the pore size distribution. With the exception of dense aggregates, which yield bimodal pore size distributions with a smaller mode which is below the particle radius, pore size distribution modes are near or above the primary particle geometric mean radius. These findings may aid in the design of particulate film deposition systems utilizing gas-phase synthesized or aerosolized particles. At the same time, the present calculations are limited to instances of modest deposition velocities and minimal particulate film restructuring. Future studies, incorporating restructuring phenomena either during or post deposition (Baric et al., 2019) may serve to further inform the extent to which pore size distribution is largely determined by porosity in aerosol deposited films.

Gas effective conductivity calculations suggest that aerosol-deposited films can achieve similar thermal conductivities to aerogel materials, with experimentally achievable process conditions for a variety of aerosol deposition systems. Despite the recent attention to aerosol deposition as a method to make coatings, regular implementation for porous coatings is not yet fully realized. Nonetheless we suggest it is a viable route to scalable porous materials, as film deposition does not carry with its requirements on narrow particle size distributions or the need to reduce aggregation, as often does the production of nanomaterials to be used in liquid suspensions.

Chapter 6. Conclusions

The goal of the studies conducted in this dissertation was to explore the potential of ion mobility spectrometry for improved chemical analysis by using 3 hyphenated IMS systems. Separately, particulate film deposition was simulated with consideration of agglomeration, polydispersity, and coalescence of primary particles. The conclusions of each study are summarized as follows.

First, the full size distribution of CMP slurries (SiO_2, Al_2O_3, TiO_2, ZrO_2, and CeO_2) were obtained by utilizing an air-jet nebulizer-DMA. The implementation of the online dilution modules in the nebulizer and reduction of droplet sizes prevented possible distortions of particle size distributions due to agglomerations and nonvolatile residues demonstrating a combination of an improved air-jet nebulizer and IMS can be a powerful tool for hydrosol sample analysis. Furthermore, the use of volume standards (with known volume concentration) enabled aerosol-hydrosol concentration conversions showing the promising IMS capability to directly quantify size distributions in the liquid phase. However, this process needs to be further standardized with an improved transfer function for the system. The comparison of resulting size distributions from IMS, DLS, and SEM suggested that IMS yields more accurate size distributions for spherical particles with higher polydispersity. However, for non-spherical particles different approaches yielded different equivalent diameters (IMS - mobility diameter, DLS - hydrodynamic diameter, SEM - projected area equivalent diameter) indicating that IMS based measurements cannot replace DLS and SEM but need to be utilized as a supplemental method. The suggested potential future work is to analyze slurry particles using an ICP-MS at the downstream of the IMS for information regarding atomic composition as a function of mobility diameters.

Second, an air-jet nebulizer-DMA-DMA investigated gas phase vapor uptake by low charge state protein ions in the mass range of 66-444 kDa (bovine serum albumin, transferrin, immunogloubin G, and apoferritin). The results suggest that protein ions adsorb water, nonane, and 1-butanol but their growth factors are less significant compared to those of soluble salts (the highest growth factor was around 1.06 with saturation of nonane). The growth factors appear to vary depending on vapor type, protein diameter, and the protein itself. Adjustment in pH levels of the sample solution did not display noticeable effects on growth factors except slightly larger standard deviations, and increased variations in growth factors with water vapor introduction. We applied κ-Köhler theory to quantify the amenability of protein ions to vapors and the analysis yielded higher κ values for nonane than for water and 1-butanol. However, the regression fitting for κ suggests that growth factors of protein ions cannot be interpretated by κ-Köhler perfectly. While this study denotes controlled vapor uptake measurements with tandem IMSs yield additional information beyond traditional low-field IMS experiments, growth factors and κ values still can be correlated with mobility diameter. In total, the results indicate vapor uptake measurements of protein ions are not completely orthogonal as a characterization tool to mobility at low field strengths. The resolution limits of the DMAs used in this study prevented the observation of possible conformational changes of protein ions and this limitation can be resolved by using different DMAs with higher resolutions (Perez-Lorenzo and de la Mora, 2021). The data analysis can be further improved by exploiting more complete TDMA inversion process (Gysel et al., 2009) wherein DMA transfer functions are accounted for. Suggested subsequent research is to adjust the temperature of the system to see the effect of temperature on the tendency of vapor uptake.

Third, I implemented an ESI-DMA-FAIMS system successfully. This system is a unique combination of gas phase ion mobility filters with potential to separate ions based on orthogonal characteristics, without mass spectrometry. The DMA measures K_0 directly before FAIMS measurements and the FAIMS detects compensation voltages of mobility selected ions at different dispersion field strengths which will significantly contribute to identification of α functions of numerous analytes which has not been fully reported. In this study, tetrabutylammonium$^+$, tetrahepytlammonium$^+$, tetradecylammonium$^+$, and tetradodecylammonium$^+$ were analyzed by the DMA-FAIMS system with air as the carrier gas at atmospheric pressure and at room temperature (295 K). Ion mobility of these 4 ions started varying at 80 Td and each compensation spectra deviates noticeably from each other above 150 Td. The truncated α functions of TBA^+, THA^+, TDA^+, and $TDDA^+$ were calculated but this approach was not effective at field strengths higher than 150 Td as described in previous studies. These results show that a higher order α function or improved inversion process from compensation voltages to α function is essential for precise analysis of DMA-FAIMS data. Even though differentiable CV spectra were observed between different analytes, the difference between TDA^+ and $TDDA^+$ was marginal. Therefore, future DMA-FAIMS measurements are suggested to utilize vapor introduction to carrier gas, and temperature and pressure adjustments to find optimal operating conditions to maximize separation capability.

Lastly, a study of particulate film simulation (Lindquist et al., 2014) was conducted by introducing agglomerates and polydisperse particles and adjusting the coalescence between particles. I analyzed the pore size distribution of resulting films using PSDsolv developed by Bhattacharya and Gubbins (2006). The pore size distribution appears to be

largely dependent on porosity regardless of individual parameters except large dense agglomerates which create bimodal pore size distributions. We calculated thermal conductivity of the resulting films based on a newly developed thermal conductivity model to consider non-continuum effects in pores. The calculated thermal conductivities were comparable to measured thermal conductivities of silica aerogels. We believe this study provides a more complete picture of particulate film formation and the results infer that aerosol deposition is a tractable approach to achieve films with comparable thermal characteristics to aerogel materials. However, this simulation did not consider reconstruction of particles after initial contact (to substrates or to other particles) nor deformation of particles holding the discrepancy between simulations and reality. The suggested subsequent work is to incorporate molecular dynamics models to consider factors like particle bouncing, reconstruction by external forces, and deformation of particles due to collisions.

Bibliography

ABRAMSSON, M. L., SAHIN, C., HOPPER, J. T. S., BRANCA, R. M. M., DANIELSSON, J., XU, M., CHANDLER, S. A., ÖSTERLUND, N., ILAG, L. L., LEPPERT, A., COSTEIRA-PAULO, J., LANG, L., TEILUM, K., LAGANOWSKY, A., BENESCH, J. L. P., OLIVEBERG, M., ROBINSON, C. V., MARKLUND, E. G., ALLISON, T. M., WINTHER, J. R. & LANDREH, M. 2021. Charge Engineering Reveals the Roles of Ionizable Side Chains in Electrospray Ionization Mass Spectrometry. *JACS Au,* 1**,** 2385-2393.

ADACHI, M., OKUYAMA, K., KOUSAKA, Y. & TANAKA, H. 1988. Preparation of gas sensitive film by deposition of ultrafine tin dioxide particles. *Journal of Aerosol Science,* 19**,** 253-263.

ADAMCZYK, J. & FUIERER, P. 2018. Compressive stress in nano-crystalline titanium dioxide films by aerosol deposition. *Surface and Coatings Technology,* 350**,** 542-549.

ADAMCZYK, J. M., GHOSH, S., BRADEN, T. L., HOGAN, C. J. & TOBERER, E. S. 2019. Alloyed Thermoelectric PbTe–SnTe Films Formed via Aerosol Deposition. *ACS Combinatorial Science,* 21**,** 753-759.

AGARWAL, J. K. & SEM, G. J. 1980. Continuous flow, single-particle-counting condensation nucleus counter. *Journal of Aerosol Science,* 11**,** 343-357.

AHONEN, L., LI, C., KUBEČKA, J., IYER, S., VEHKAMÄKI, H., PETÄJÄ, T., KULMALA, M. & HOGAN JR, C. J. 2019. Ion Mobility-Mass Spectrometry of Iodine Pentoxide–Iodic Acid Hybrid Cluster Anions in Dry and Humidified Atmospheres. *The Journal of Physical Chemistry Letters,* 10**,** 1935-1941.

AKEDO, J. 2006. Aerosol Deposition of Ceramic Thick Films at Room Temperature: Densification Mechanism of Ceramic Layers. *Journal of the American Ceramic Society,* 89**,** 1834-1839.

AKEDO, J. & LEBEDEV, M. 2002. Powder Preparation in Aerosol Deposition Method for Lead Zirconate Titanate Thick Films. *Japanese Journal of Applied Physics,* 41**,** 6980.

AKSENOV, A. A., KAPRON, J. & DAVIS, C. E. 2012. Predicting compensation voltage for singly-charged ions in high-field asymmetric waveform ion mobility spectrometry (FAIMS). *Journal of the American Society for Mass Spectrometry,* 23**,** 1794-1798.

AKSENOV, A. A. & KAPRON, J. T. 2010. Behaviour of tetraalkylammonium ions in high-field asymmetric waveform ion mobility spectrometry. *Rapid Communications in Mass Spectrometry: An International Journal Devoted to the Rapid Dissemination of Up-to-the-Minute Research in Mass Spectrometry,* 24**,** 1392-1396.

AN, S., JOSHI, B., YARIN, A. L., SWIHART, M. T. & YOON, S. S. 2020. Supersonic Cold Spraying for Energy and Environmental Applications: One-Step Scalable Coating Technology for Advanced Micro- and Nanotextured Materials. *Advanced Materials,* 32**,** 1905028.

APPOLONI, C. R., FERNANDES, C. P., INNOCENTINI, M. D. D. M. & MACEDO, Á. 2004. Ceramic foams porous microstructure characterization by X-ray microtomography. *Materials Research,* 7**,** 557-564.

ARMENTA, S., ALCALA, M. & BLANCO, M. 2011. A review of recent, unconventional applications of ion mobility spectrometry (IMS). *Analytica chimica acta,* 703**,** 114-123.

ASBURY, G. R. & HILL, H. H. 2000. Using Different Drift Gases To Change Separation Factors (α) in Ion Mobility Spectrometry. *Analytical Chemistry,* 72**,** 580-584.

ATKINSON, A. J., BI, Y., FIRTH, P., ALREHAILI, O., WESTERHOFF, P. & HOLMAN, Z. C. 2020. Aerosol impaction-driven assembly produces evenly dispersed nanoparticle coating on polymeric water treatment membranes. *Journal of Nanoparticle Research,* 22**,** 102.

BACHER, G., SZYMANSKI, W. W., KAUFMAN, S. L., ZÖLLNER, P., BLAAS, D. & ALLMAIER, G. 2001. Charge-reduced nano electrospray ionization combined with

differential mobility analysis of peptides, proteins, glycoproteins, noncovalent protein complexes and viruses. *Journal of Mass Spectrometry,* 36**,** 1038-1052.

BAKER, E. S., LIVESAY, E. A., ORTON, D. J., MOORE, R. J., DANIELSON III, W. F., PRIOR, D. C., IBRAHIM, Y. M., LAMARCHE, B. L., MAYAMPURATH, A. M. & SCHEPMOES, A. A. 2010. An LC-IMS-MS platform providing increased dynamic range for high-throughput proteomic studies. *Journal of proteome research,* 9**,** 997-1006.

BARIC, V., CIACCHI, L. C. & MÄDLER, L. 2019. Compaction-induced restructuring of aggregated nanoparticle films using the discrete element method. *Powder Technology,* 342**,** 773-779.

BARNETT, D. A., ELLS, B., GUEVREMONT, R., PURVES, R. W. & VIEHLAND, L. A. 2000. Evaluation of carrier gases for use in high-field asymmetric waveform ion mobility spectrometry. *Journal of the American Society for Mass Spectrometry,* 11**,** 1125-1133.

BARRETT, E. P., JOYNER, L. G. & HALENDA, P. P. 1951. The determination of pore volume and area distributions in porous substances. I. Computations from nitrogen isotherms. *Journal of the American Chemical society,* 73**,** 373-380.

BASIM, G., ADLER, J., MAHAJAN, U., SINGH, R. & MOUDGIL, B. 2000. Effect of particle size of chemical mechanical polishing slurries for enhanced polishing with minimal defects. *Journal of the Electrochemical Society,* 147**,** 3523.

BASTANINEJAD, M. & AHMADI, G. 2005. Modeling the effects of abrasive size distribution, adhesion, and surface plastic deformation on chemical-mechanical polishing. *Journal of the Electrochemical Society,* 152**,** G720.

BEAUDETTE, C. A., HELD, J. T., GREENBERG, B. L., NGUYEN, P. H., CONCANNON, N. M., HOLMES, R. J., MKHOYAN, K. A., AYDIL, E. S. & KORTSHAGEN, U. R. 2020a. Plasmonic nanocomposites of zinc oxide and titanium nitride. *Journal of Vacuum Science & Technology A,* 38**,** 042404.

BEAUDETTE, C. A., WANG, X. & KORTSHAGEN, U. R. 2020b. Nanocrystal-based inorganic nanocomposites: A new paradigm for plasma-produced optoelectronic thin films. *Plasma Processes and Polymers,* n/a**,** e2000002.

BEN-NISSAN, G. & SHARON, M. 2018. The application of ion-mobility mass spectrometry for structure/function investigation of protein complexes. *Current Opinion in Chemical Biology,* 42**,** 25-33.

BHATTACHARYA, S. & GUBBINS, K. E. 2006. Fast Method for Computing Pore Size Distributions of Model Materials. *Langmuir,* 22**,** 7726-7731.

BI, C., TANG, G. H., HU, Z. J., YANG, H. L. & LI, J. N. 2014. Coupling model for heat transfer between solid and gas phases in aerogel and experimental investigation. *International Journal of Heat and Mass Transfer,* 79**,** 126-136.

BISKOS, G., MALINOWSKI, A., RUSSELL, L. M., BUSECK, P. R. & MARTIN, S. T. 2006. Nanosize effect on the deliquescence and the efflorescence of sodium chloride particles. *Aerosol Science and Technology,* 40**,** 97-106.

BISSON, A., RIGACCI, A., LECOMTE, D. & ACHARD, P. 2004. Effective thermal conductivity of divided silica xerogel beds. *Journal of Non-Crystalline Solids,* 350**,** 379-384.

BOHRER, B. C., MERENBLOOM, S. I., KOENIGER, S. L., HILDERBRAND, A. E. & CLEMMER, D. E. 2008. Biomolecule Analysis by Ion Mobility Spectrometry. *Annual Review of Analytical Chemistry,* 1**,** 293-327.

BORNSCHEIN, R. E., NIU, S., ESCHWEILER, J. & RUOTOLO, B. T. 2016. Ion Mobility-Mass Spectrometry Reveals Highly-Compact Intermediates in the Collision Induced Dissociation of Charge-Reduced Protein Complexes. *Journal of the American Society for Mass Spectrometry,* 27**,** 41-49.

BRUNAUER, S., EMMETT, P. H. & TELLER, E. 1938. Adsorption of Gases in Multimolecular Layers. *Journal of the American Chemical Society,* 60**,** 309-319.

BURYAKOV, I. 2002. Coefficient of ion mobility versus electric field strength dependence in gases: Experimental determination. *Technical Physics,* 47**,** 1453-1457.

BURYAKOV, I., KOLOMIETS, Y. N. & LUPPU, B. 2001. Detection of explosive vapors in the air using an ion drift nonlinearity spectrometer. *Journal of Analytical Chemistry,* 56**,** 336-340.

BURYAKOV, I., KRYLOV, E., NAZAROV, E. & RASULEV, U. K. 1993. A new method of separation of multi-atomic ions by mobility at atmospheric pressure using a high-frequency amplitude-asymmetric strong electric field. *International Journal of Mass Spectrometry and Ion Processes,* 128**,** 143-148.

BUSH, M. F., HALL, Z., GILES, K., HOYES, J., ROBINSON, C. V. & RUOTOLO, B. T. 2010. Collision Cross Sections of Proteins and their Complexes: a Calibration Framework and Database for Gas-Phase Structural Biology. *Analytical Chemistry,* 82**,** 9557-9565.

BUTCHER, D., MIKSOVSKA, J., RIDGEWAY, M. E., PARK, M. A. & FERNANDEZ-LIMA, F. 2019. The effects of solution additives and gas-phase modifiers on the molecular environment and conformational space of common heme proteins. *Rapid Communications in Mass Spectrometry,* 33**,** 399-404.

CAMPBELL, J. L., ZHU, M. & HOPKINS, W. S. 2014. Ion-molecule clustering in differential mobility spectrometry: lessons learned from tetraalkylammonium cations and their isomers. *Journal of The American Society for Mass Spectrometry,* 25**,** 1583-1591.

CARBONE, F. & LARRIBA-ANDALUZ, C. 2021. The size-mobility relationship of ions, aerosols, and other charged particle matter. *Journal of aerosol science,* 151.

CARNAHAN, B. & TARASSOV, A. 1995. US Patent# 5420424. *Ion Mobility Spectrometer*.

CASTILLO, J. L., MARTIN, S., RODRIGUEZ-PEREZ, D., HIGUERA, F. J. & GARCIA-YBARRA, P. L. 2018. Nanostructured porous coatings via electrospray atomization and deposition of nanoparticle suspensions. *Journal of Aerosol Science,* 125**,** 148-163.

CHANG, R. Y. W., SLOWIK, J. G., SHANTZ, N. C., VLASENKO, A., LIGGIO, J., SJOSTEDT, S. J., LEAITCH, W. R. & ABBATT, J. P. D. 2010. The hygroscopicity parameter (κ) of ambient organic aerosol at a field site subject to biogenic and anthropogenic influences: relationship to degree of aerosol oxidation. *Atmos. Chem. Phys.,* 10**,** 5047-5064.

CHEN, D.-R., PUI, D. Y., HUMMES, D., FISSAN, H., QUANT, F. & SEM, G. 1998. Design and evaluation of a nanometer aerosol differential mobility analyzer (Nano-DMA). *Journal of Aerosol Science,* 29**,** 497-509.

CHEN, Q., GUEST, J. R. & THIMSEN, E. 2017. Visualizing Current Flow at the Mesoscale in Disordered Assemblies of Touching Semiconductor Nanocrystals. *The Journal of Physical Chemistry C,* 121**,** 15619-15629.

CHEN, X., SETO, T., KORTSHAGEN, U. R. & HOGAN JR, C. J. 2020. Size and structural characterization of Si nanocrystal aggregates from a low pressure nonthermal plasma reactor. *Powder Technology,* 373**,** 164-173.

CHIU, F.-C. & LAI, C.-M. 2010. Optical and electrical characterizations of cerium oxide thin films. *Journal of Physics D: Applied Physics,* 43**,** 075104.

CHO, K., HOGAN, C. J. & BISWAS, P. 2007. Study of the mobility, surface area, and sintering behavior of agglomerates in the transition regime by tandem differential mobility analysis. *Journal of Nanoparticle Research,* 9**,** 1003-1012.

CHOI, J.-J., CHOI, J.-H., RYU, J., HAHN, B.-D., KIM, J.-W., AHN, C.-W., YOON, W.-H. & PARK, D.-S. 2012. Microstructural evolution of YSZ electrolyte aerosol-deposited on porous NiO-YSZ. *Journal of the European Ceramic Society,* 32**,** 3249-3254.

CHOI, J.-J., OH, S.-H., NOH, H.-S., KIM, H.-R., SON, J.-W., PARK, D.-S., CHOI, J.-H., RYU, J., HAHN, B.-D., YOON, W.-H. & LEE, H.-W. 2011. Low temperature fabrication of nano-structured porous LSM–YSZ composite cathode film by aerosol deposition. *Journal of Alloys and Compounds,* 509**,** 2627-2630.

CHOI, W., ABIADE, J., LEE, S.-M. & SINGH, R. K. 2004. Effects of Slurry Particles on Silicon Dioxide CMP. *Journal of The Electrochemical Society,* 151**,** G512.
COHEN, M. J. & KARASEK, F. 1970. Plasma chromatography™—a new dimension for gas chromatography and mass spectrometry. *Journal of Chromatographic science,* 8**,** 330-337.
COLLINS, D. R., COCKER, D. R., FLAGAN, R. C. & SEINFELD, J. H. 2004. The scanning DMA transfer function. *Aerosol Science and Technology,* 38**,** 833-850.
COVINGTON, J., DER SCHEE, M. V., EDGE, A., BOYLE, B., SAVAGE, R. & ARASARADNAM, R. 2015. The application of FAIMS gas analysis in medical diagnostics. *Analyst,* 140**,** 6775-6781.
CUMERAS, R., FIGUERAS, E., DAVIS, C. E., BAUMBACH, J. I. & GRACIA, I. 2015a. Review on ion mobility spectrometry. Part 1: current instrumentation. *Analyst,* 140**,** 1376-1390.
CUMERAS, R., FIGUERAS, E., DAVIS, C. E., BAUMBACH, J. I. & GRACIA, I. 2015b. Review on ion mobility spectrometry. Part 2: hyphenated methods and effects of experimental parameters. *Analyst,* 140**,** 1391-1410.
CUNNINGHAM, E. 1910. On the velocity of steady fall of spherical particles through fluid medium. *Proceedings of the Royal Society of London. Series A, Containing Papers of a Mathematical and Physical Character,* 83**,** 357-365.
DAHNEKE, B. E. 1983. Simple Kinetic Theory of Brownian Diffusion in Vapors and Aerosols. *In:* MEYER, R. E. (ed.) *Theory of Dispersed Multiphase Flow.* New York: Academic Press.
DAVIDSON, K. L., OBERREIT, D. R., HOGAN, C. J. & BUSH, M. F. 2017. Nonspecific aggregation in native electrokinetic nanoelectrospray ionization. *International Journal of Mass Spectrometry,* 420**,** 35-42.
DAVIES, C. 1945a. Definitive equations for the fluid resistance of spheres. *Proceedings of the Physical Society,* 57**,** 259.
DAVIES, C. N. 1945b. Definitive equations for the fluid resistance of spheres. *Proceedings of the Physical Society,* 57**,** 259-270.
DE JUAN, L. & DE LA MORA, J. F. 1996. On-line sizing of colloidal nanoparticles via electrospray and aerosol techniques. ACS Publications.
DE LA MORA, J. F. & KOZLOWSKI, J. 2013. Hand-held differential mobility analyzers of high resolution for 1–30 nm particles: Design and fabrication considerations. *Journal of Aerosol Science,* 57**,** 45-53.
ECKHARDT, N., ALTMANN, J., FAUSTMANN, P., REINHOLD, B. & MA, H. 2019. Multiparameter modelling An approach to forecast process performance based on slurry parameters. *International Conference on Planarization/CMP Technology.* Hsinchu, Taiwan.
EICEMAN, G. & STONE, J. 2004. Peer reviewed: ion mobility spectrometers in national defense. ACS Publications.
EIGUREN FERNANDEZ, A., LEWIS, G. S. & HERING, S. V. 2014. Design and laboratory evaluation of a sequential spot sampler for time-resolved measurement of airborne particle composition. *Aerosol Science and Technology,* 48**,** 655-663.
ELLIS, H., MCDANIEL, E., ALBRITTON, D., VIEHLAND, L., LIN, S. & MASON, E. 1978. Transport properties of gaseous ions over a wide energy range. Part II. *Atomic data and nuclear data tables,* 22**,** 179-217.
ELLIS, H., PAI, R., MCDANIEL, E., MASON, E. & VIEHLAND, L. 1976. Transport properties of gaseous ions over a wide energy range. *Atomic Data and Nuclear Data Tables,* 17**,** 177-210.
EPSTEIN, P. S. 1924. On the resistance experienced by spheres in their motion through gases. *Physical Review,* 23**,** 710.
ERILIN, I. S., AGARKOV, D. A., BURMISTROV, I. N., PUKHA, V. E., YALOVENKO, D. V., LYSKOV, N. V., LEVIN, M. N. & BREDIKHIN, S. I. 2020. Aerosol deposition of thin-

film solid electrolyte membranes for anode-supported solid oxide fuel cells. *Materials Letters,* 266**,** 127439.
ERMAK, D. L. & BUCKHOLZ, H. 1980. Numerical-Integration of the Langevin Equation - Monte-Carlo Simulation. *Journal of Computational Physics,* 35**,** 169-182.
EWING, R. G., ATKINSON, D. A., EICEMAN, G. & EWING, G. 2001. A critical review of ion mobility spectrometry for the detection of explosives and explosive related compounds. *Talanta,* 54**,** 515-529.
EXNER, J., SCHUBERT, M., HANFT, D., KITA, J. & MOOS, R. 2019. How to treat powders for the room temperature aerosol deposition method to avoid porous, low strength ceramic films. *Journal of the European Ceramic Society,* 39**,** 592-600.
FENN, J. B., MANN, M., MENG, C. K., WONG, S. F. & WHITEHOUSE, C. M. 1989. Electrospray ionization for mass spectrometry of large biomolecules. *Science,* 246**,** 64-71.
FERNANDEZ MAESTRE, R. 2017. Calibration of the mobility scale in ion mobility spectrometry: the use of 2,4-lutidine as a chemical standard, the two-standard calibration method and the incorrect use of drift tube temperature for calibration. *Analytical Methods,* 9**,** 4288-4292.
FERNÁNDEZ-GARCÍA, J. & FERNÁNDEZ DE LA MORA, J. 2013. Measuring the Effect of Ion-Induced Drift-Gas Polarization on the Electrical Mobilities of Multiply-Charged Ionic Liquid Nanodrops in Air. *Journal of the American Society for Mass Spectrometry,* 24**,** 1872-1889.
FERNÁNDEZ-MAESTRE, R., MEZA-MORELOS, D. & WU, C. 2016. Shift reagents in ion mobility spectrometry: the effect of the number of interaction sites, size and interaction energies on the mobilities of valinol and ethanolamine. *Journal of Mass Spectrometry,* 51**,** 378-383.
FILIPPOV, A. V., ZURITA, M. & ROSNER, D. E. 2000. Fractal-like aggregates: Relation between morphology and physical properties. *Journal of Colloid and Interface Science,* 229**,** 261-273.
FIRTH, P. & HOLMAN, Z. C. 2018. Aerosol Impaction-Driven Assembly System for the Production of Uniform Nanoparticle Thin Films with Independently Tunable Thickness and Porosity. *ACS Applied Nano Materials,* 1**,** 4351-4357.
FISCHBACH, F. & ANDEREGG, J. 1965. An X-ray scattering study of ferritin and apoferritin. *Journal of molecular biology,* 14**,** 458-IN15.
FRAGKIADOULAKIS, P., GEIVANIDIS, S. & SAMARAS, Z. 2018. Modeling a resistive soot sensor by particle deposition mechanisms. *Journal of Aerosol Science,* 123**,** 76-90.
FUCHS, N. & STECHKINA, I. 1962. Resistance of a gaseous medium to the motion of a spherical particle of a size comparable to the mean free path of the gas molecules. *Transactions of the Faraday Society,* 58**,** 1949-1952.
FUCHS, N. A. & SUTUGIN, A. G. 1970. *Highly dispersed aerosols,* Ann Arbor,, Ann Arbor Science Publishers.
GAMERO-CASTAÑO, M. & DE LA MORA, J. F. 2002. Ion-induced nucleation: Measurement of the effect of embryo's size and charge state on the critical supersaturation. *The Journal of Chemical Physics,* 117**,** 3345-3353.
GANDHI, B. K. & BORSE, S. V. 2004. Nominal particle size of multi-sized particulate slurries for evaluation of erosion wear and effect of fine particles. *Wear,* 257**,** 73-79.
GELB, L. D. & GUBBINS, K. E. 1999. Pore Size Distributions in Porous Glasses: A Computer Simulation Study. *Langmuir,* 15**,** 305-308.
GONZÁLEZ FLÓREZ, A. I., MUCHA, E., AHN, D.-S., GEWINNER, S., SCHÖLLKOPF, W., PAGEL, K. & VON HELDEN, G. 2016. Charge-Induced Unzipping of Isolated Proteins to a Defined Secondary Structure. *Angewandte Chemie International Edition,* 55**,** 3295-3299.

GOPALAKRISHNAN, R. & HOGAN, C. J. 2011. Determination of the Transition Regime Collision Kernel from Mean First Passage Times. *Aerosol Science and Technology,* 45**,** 1499-1509.

GOPALAKRISHNAN, R. & HOGAN JR, C. J. 2011. Determination of the transition regime collision kernel from mean first passage times. *Aerosol Science and Technology,* 45**,** 1499-1509.

GOPALAKRISHNAN, R., MCMURRY, P. H. & HOGAN, C. J. 2015a. The Bipolar Diffusion Charging of Nanoparticles: A Review and Development of Approaches for Non-Spherical Particles. *Aerosol Science and Technology,* 49**,** 1181-1194.

GOPALAKRISHNAN, R., MCMURRY, P. H. & HOGAN JR, C. J. 2015b. The electrical mobilities and scalar friction factors of modest-to-high aspect ratio particles in the transition regime. *Journal of Aerosol Science,* 82**,** 24-39.

GOPALAKRISHNAN, R., THAJUDEEN, T. & HOGAN JR, C. J. 2011. Collision limited reaction rates for arbitrarily shaped particles across the entire diffusive Knudsen number range. *The Journal of chemical physics,* 135**,** 054302.

GREENBERG, B. L., ROBINSON, Z. L., REICH, K. V., GORYNSKI, C., VOIGT, B. N., FRANCIS, L. F., SHKLOVSKII, B. I., AYDIL, E. S. & KORTSHAGEN, U. R. 2017. ZnO Nanocrystal Networks Near the Insulator–Metal Transition: Tuning Contact Radius and Electron Density with Intense Pulsed Light. *Nano Letters,* 17**,** 4634-4642.

GUDDAT, S., THEVIS, M., KAPRON, J., THOMAS, A. & SCHÄNZER, W. 2009. Application of FAIMS to anabolic androgenic steroids in sport drug testing. *Drug Testing and Analysis,* 1**,** 545-553.

GUEVREMONT, R. 2004. High-field asymmetric waveform ion mobility spectrometry: a new tool for mass spectrometry. *Journal of Chromatography A,* 1058**,** 3-19.

GUEVREMONT, R. & PURVES, R. W. 1999. Atmospheric pressure ion focusing in a high-field asymmetric waveform ion mobility spectrometer. *Review of Scientific Instruments,* 70**,** 1370-1383.

GYSEL, M., MCFIGGANS, G. B. & COE, H. 2009. Inversion of tandem differential mobility analyser (TDMA) measurements. *Journal of Aerosol Science,* 40**,** 134-151.

HANFT, D., EXNER, J., SCHUBERT, M., STOCKER, T., FUIERER, P. & MOOS, R. 2015. An Overview of the Aerosol Deposition Method: Process Fundamentals and New Trends in Materials Applications. *Journal of Ceramic Science and Technology,* 6**,** 147-181.

HARRISON, P. Ferritin: an iron-storage molecule. Seminars in hematology, 1977. 55-70.

HIGUERA, F. J. 2018. Structure of deposits formed from electrosprayed aggregates of nanoparticles. *Journal of Aerosol Science,* 118**,** 45-58.

HIRAYAMA, K., AKASHI, S., FURUYA, M. & FUKUHARA, K.-I. 1990. Rapid confirmation and revision of the primary structure of bovine serum albumin by ESIMS and Frit-FAB LC/MS. *Biochemical and biophysical research communications,* 173**,** 639-646.

HOGAN, C. J. & BISWAS, P. 2008a. Monte Carlo simulation of macromolecular ionization by nanoelectrospray. *Journal of the American Society for Mass Spectrometry,* 19**,** 1098-1107.

HOGAN, C. J. & BISWAS, P. 2008b. Porous film deposition by electrohydrodynamic atomization of nanoparticle sols. *Aerosol Science and Technology,* 42**,** 75-85.

HOGAN, C. J. & DE LA MORA, J. F. 2011. Ion mobility measurements of nondenatured 12–150 kDa proteins and protein multimers by Tandem Differential Mobility Analysis–Mass Spectrometry (DMA-MS). *Journal of the American Society for Mass Spectrometry,* 22**,** 158-172.

HOGAN, C. J. & FERNANDEZ DE LA MORA, J. 2011. Ion Mobility Measurements of Non-Denatured 12 - 150 kDa Proteins and Protein Multimers by Tandem Differential Mobility Analysis - Mass Spectrometry (DMA-MS). *Journal of the American Society for Mass Spectrometry,* 22**,** 158-172.

HOGAN JR, C. J. & BISWAS, P. 2008. Narrow size distribution nanoparticle production by electrospray processing of ferritin. *Journal of Aerosol Science,* 39**,** 432-440.

HOLMAN, Z. C. & KORTSHAGEN, U. R. 2010. A flexible method for depositing dense nanocrystal thin films: impaction of germanium nanocrystals. *Nanotechnology,* 21**,** 335302.

HUANG, C., NICHOLS, W. T., O'BRIEN, D. T., BECKER, M. F., KOVAR, D. & KETO, J. W. 2007. Supersonic jet deposition of silver nanoparticle aerosols: Correlations of impact conditions and film morphologies. *Journal of Applied Physics,* 101**,** 064902.

HUANG, S.-H. & CHEN, C.-C. 2003. Loading Characteristics of a Miniature Wire-Plate Electrostatic Precipitator. *Aerosol Science and Technology,* 37**,** 109-121.

HUNT, B., THAJUDEEN, T. & HOGAN, C. J. 2014. The Single-Fiber Collision Rate and Filtration Efficiency for Nanoparticles I: The First-Passage Time Calculation Approach. *Aerosol Science and Technology,* 48**,** 875-885.

HUXLEY, L., CROMPTON, R. & ELFORD, M. 1966. Use of the parameter E/N. *Physics Bulletin,* 17**,** 251.

HÄMERI, K., VÄKEVÄ, M., HANSSON, H.-C. & LAAKSONEN, A. 2000. Hygroscopic growth of ultrafine ammonium sulphate aerosol measured using an ultrafine tandem differential mobility analyzer. *Journal of Geophysical Research: Atmospheres,* 105**,** 22231-22242.

JANG, S., KULKARNI, A., QIN, H. & KIM, T. 2016. Note: Evaluation of slurry particle size analyzers for chemical mechanical planarization process. *Review of Scientific Instruments,* 87**,** 046101.

JEON, S., OBERREIT, D. R., VAN SCHOONEVELD, G., GAO, Z., BISCHOF, J. C., HAYNES, C. L. & HOGAN, C. J. 2016a. Ion-Mobility-Based Quantification of Surface-Coating-Dependent Binding of Serum Albumin to Superparamagnetic Iron Oxide Nanoparticles. *ACS Applied Materials & Interfaces,* 8**,** 24482-24490.

JEON, S., OBERREIT, D. R., VAN SCHOONEVELD, G. & HOGAN, C. J. 2016b. Liquid Nebulization–Ion Mobility Spectrometry Based Quantification of Nanoparticle–Protein Conjugate Formation. *Analytical Chemistry,* 88**,** 7667-7674.

JEON, S., OBERREIT, D. R., VAN SCHOONEVELD, G. & HOGAN, C. J. 2016c. Nanomaterial size distribution analysis via liquid nebulization coupled with ion mobility spectrometry (LN-IMS). *Analyst,* 141**,** 1363-1375.

JIANG, J., ATTOUI, M., HEIM, M., BRUNELLI, N. A., MCMURRY, P. H., KASPER, G., FLAGAN, R. C., GIAPIS, K. & MOURET, G. 2011. Transfer functions and penetrations of five differential mobility analyzers for sub-2 nm particle classification. *Aerosol science and technology,* 45**,** 480-492.

JO, H. S., KIM, M.-W., KIM, T. G., AN, S., PARK, H.-G., LEE, J.-G., JAMES, S. C., CHOI, J. & YOON, S. S. 2018. Supersonically spray-coated copper meshes as textured surfaces for pool boiling. *International Journal of Thermal Sciences,* 132**,** 26-33.

KADDIS, C. S., LOMELI, S. H., YIN, S., BERHANE, B., APOSTOL, M. I., KICKHOEFER, V. A., ROME, L. H. & LOO, J. A. 2007. Sizing Large Proteins and Protein Complexes by Electrospray Ionization Mass Spectrometry and Ion Mobility. *Journal of the American Society for Mass Spectrometry,* 18**,** 1206-1216.

KAFLE, A., COY, S. L., WONG, B. M., FORNACE, A. J., GLICK, J. J. & VOUROS, P. 2014. Understanding Gas Phase Modifier Interactions in Rapid Analysis by Differential Mobility-Tandem Mass Spectrometry. *Journal of the American Society for Mass Spectrometry,* 25**,** 1098-1113.

KAFLE, G. K., KHOT, L. R., SANKARAN, S., BAHLOL, H. Y., TUFARIELLO, J. A. & HILL JR, H. H. 2016. State of ion mobility spectrometry and applications in agriculture: A review. *Engineering in agriculture, environment and food,* 9**,** 346-357.

KAUFMAN, S. L., SKOGEN, J. W., DORMAN, F. D., ZARRIN, F. & LEWIS, K. C. 1996. Macromolecule analysis based on electrophoretic mobility in air: Globular proteins. *Analytical Chemistry,* 68**,** 1895-1904.

KILÁR, F., SIMON, I., LAKATOS, S., VONDERVISZT, F., MEDGYESI, G. A. & ZÁVODSZKY, P. 1985. Conformation of human IgG subclasses in solution: Small-angle X-ray scattering and hydrodynamic studies. *European journal of biochemistry,* 147**,** 17-25.

KIM, D.-H., KANG, H.-G., KIM, S.-K., PAIK, U. & PARK, J.-G. 2006. Reduction of large particles in ceria slurry by aging and selective sedimentation and its effect on shallow trench isolation chemical mechanical planarization. *Japanese journal of applied physics,* 45**,** 6790.

KIM, H., YANG, J. C. & KIM, T. 2010. Measurement of CMP Slurry Abrasive Size Distribution by Scanning Mobility Particle Sizer. *Electrochemical and Solid State Letters,* 13**,** H137.

KIM, J. H., MULHOLLAND, G. W., KUKUCK, S. R. & PUI, D. Y. 2005. Slip correction measurements of certified PSL nanoparticles using a nanometer differential mobility analyzer (nano-DMA) for Knudsen number from 0.5 to 83. *Journal of Research of the National Institute of Standards and technology,* 110**,** 31.

KIMOTO, S., DICK, W. D., HUNT, B., SZYMANSKI, W. W., MCMURRY, P. H., ROBERTS, D. L. & PUI, D. Y. 2017. Characterization of nanosized silica size standards. *Aerosol Science and Technology,* 51**,** 936-945.

KNUTSON, E. & WHITBY, K. 1975a. Aerosol classification by electric mobility: apparatus, theory, and applications. *Journal of Aerosol Science,* 6**,** 443-451.

KNUTSON, E. O. & WHITBY, K. T. 1975b. Aerosol classification by electric mobility: apparatus, theory, and applications. *Journal of Aerosol Science,* 6**,** 443-451.

KOH, T. L. & GORDON, M. J. 2013. Thin-film deposition with high pressure capillary micro-discharges under different supersonic flow and shock regimes. *Journal of Physics D: Applied Physics,* 46**,** 495204.

KOLAKOWSKI, B. M. & MESTER, Z. 2007. Review of applications of high-field asymmetric waveform ion mobility spectrometry (FAIMS) and differential mobility spectrometry (DMS). *Analyst,* 132**,** 842-864.

KRAUSE, B., MEYER, T., SIEG, H., KÄSTNER, C., REICHARDT, P., TENTSCHERT, J., JUNGNICKEL, H., ESTRELA-LOPIS, I., BUREL, A., CHEVANCE, S., GAUFFRE, F., JALILI, P., MEIJER, J., BÖHMERT, L., BRAEUNING, A., THÜNEMANN, A. F., EMMERLING, F., FESSARD, V., LAUX, P., LAMPEN, A. & LUCH, A. 2018. Characterization of aluminum, aluminum oxide and titanium dioxide nanomaterials using a combination of methods for particle surface and size analysis. *RSC Advances,* 8**,** 14377-14388.

KRYLOV, E. 2003. Comparison of the planar and coaxial field asymmetrical waveform ion mobility spectrometer (FAIMS). *International Journal of Mass Spectrometry,* 225**,** 39-51.

KRYLOV, E., NAZAROV, E., MILLER, R., TADJIKOV, B. & EICEMAN, G. 2002. Field dependence of mobilities for gas-phase-protonated monomers and proton-bound dimers of ketones by planar field asymmetric waveform ion mobility spectrometer (PFAIMS). *The Journal of Physical Chemistry A,* 106**,** 5437-5444.

KU, B. K. & DE LA MORA, J. F. 2009. Relation between electrical mobility, mass, and size for nanodrops 1–6.5 nm in diameter in air. *Aerosol Science and Technology,* 43**,** 241-249.

KUBO, M., ISHIHARA, Y., MANTANI, Y. & SHIMADA, M. 2013. Evaluation of the factors that influence the fabrication of porous thin films by deposition of aerosol nanoparticles. *Chemical Engineering Journal,* 232**,** 221-227.

KULDINOW, D., PRZYBYLAK, A., PEREZ LORENZO, L. J., OBERREIT, D. & DE LA MORA, J. F. 2021. Cluster activation studies with a diffusive condensation particle counter: Effect of chemical composition. *Journal of Aerosol Science***,** 105917.

KULKARNI, P. & BISWAS, P. 2003. Morphology of Nanostructured Films for Environmental Applications: Simulation of Simultaneous Sintering and Growth. *Journal of Nanoparticle Research,* 5**,** 259-268.

KULKARNI, P. & BISWAS, P. 2004. A Brownian dynamics simulation to predict morphology of nanoparticle deposits in the presence of interparticle interactions. *Aerosol Science and Technology,* 38**,** 541-554.

KWAK, D., KIM, J., OH, S., BAE, C. & KIM, T. 2020. Application of electrospray-scanning mobility particle sizer for the measurement of sub-10 nm chemical mechanical planarization slurry abrasive size distribution. *Review of Scientific Instruments,* 91**,** 075117.

KWANTWI-BARIMA, P., HOGAN, C. J. & CLOWERS, B. H. 2019. Deducing Proton-Bound Heterodimer Association Energies from Shifts in Ion Mobility Arrival Time Distributions. *The Journal of Physical Chemistry A,* 123**,** 2957-2965.

KWANTWI-BARIMA, P., HOGAN, C. J. & CLOWERS, B. H. 2020. Probing Gas-Phase-Clustering Thermodynamics with Ion Mobility–Mass Spectrometry: Association Energies of Phenylalanine Ions with Gas-Phase Alcohols. *Journal of the American Society for Mass Spectrometry,* 31**,** 1803-1814.

KWANTWI-BARIMA, P., OUYANG, H., HOGAN, C. J. & CLOWERS, B. H. 2017. Tuning Mobility Separation Factors of Chemical Warfare Agent Degradation Products via Selective Ion-Neutral Clustering. *Analytical Chemistry,* 89**,** 12416-12424.

LAMBIN, P. 1978. Reliability of molecular weight determination of proteins by polyacrylamide gradient gel electrophoresis in the presence of sodium dodecyl sulfate. *Analytical biochemistry,* 85**,** 114-125.

LANDAUER, R. 1952. The Electrical Resistance of Binary Metallic Mixtures. *Journal of Applied Physics,* 23**,** 779-784.

LARRIBA, C. & FERNANDEZ DE LA MORA, J. 2012. The Gas Phase Structure of Coulombically Stretched Polyethylene Glycol Ions. *The Journal of Physical Chemistry B,* 116**,** 593-598.

LARRIBA, C., HOGAN, C. J., ATTOUI, M., BORRAJO, R., FERNANDEZ-GARCIA, J. & FERNANDEZ DE LA MORA, J. 2011a. The Mobility-Volume Relationship below 3.0 nm examined by Tandem Mobility-Mass Measurement. *Aerosol Science and Technology,* 45**,** 453-467.

LARRIBA, C. & HOGAN JR, C. J. 2013. Ion mobilities in diatomic gases: measurement versus prediction with non-specular scattering models. *The Journal of Physical Chemistry A,* 117**,** 3887-3901.

LARRIBA, C., HOGAN JR, C. J., ATTOUI, M., BORRAJO, R., GARCIA, J. F. & DE LA MORA, J. F. 2011b. The mobility–volume relationship below 3.0 nm examined by tandem mobility–mass measurement. *Aerosol Science and Technology,* 45**,** 453-467.

LARRIBA-ANDALUZ, C. & CARBONE, F. 2021. The size-mobility relationship of ions, aerosols, and other charged particle matter. *Journal of Aerosol Science,* 151**,** 105659.

LEE, J., HE, S., SONG, G. & HOGAN, C. J. 2022. Size distribution monitoring for chemical mechanical polishing slurries: An intercomparison of electron microscopy, dynamic light scattering, and differential mobility analysis. *Powder Technology,* 396**,** 395-405.

LEE, J. G., KIM, D.-Y., LEE, J.-H., KIM, M.-W., AN, S., JO, H. S., NERVI, C., AL-DEYAB, S. S., SWIHART, M. T. & YOON, S. S. 2016. Scalable Binder-Free Supersonic Cold Spraying of Nanotextured Cupric Oxide (CuO) Films as Efficient Photocathodes. *ACS Applied Materials & Interfaces,* 8**,** 15406-15414.

LEE, M. W., PARK, J. J., KIM, D. Y., YOON, S. S., KIM, H. Y., KIM, D. H., JAMES, S. C., CHANDRA, S., COYLE, T., RYU, J. H., YOON, W. H. & PARK, D. S. 2011. Optimization of supersonic nozzle flow for titanium dioxide thin-film coating by aerosol deposition. *Journal of Aerosol Science,* 42**,** 771-780.

LENGGORO, I. W., WIDIYANDARI, H., HOGAN JR, C. J., BISWAS, P. & OKUYAMA, K. 2007. Colloidal nanoparticle analysis by nanoelectrospray size spectrometry with a heated flow. *Analytica chimica acta,* 585**,** 193-201.

LENGGORO, I. W., XIA, B., OKUYAMA, K. & DE LA MORA, J. F. 2002. Sizing of colloidal nanoparticles by electrospray and differential mobility analyzer methods. *Langmuir,* 18**,** 4584-4591.

LEWIS, K. C., DOHMEIER, D. M., JORGENSON, J. W., KAUFMAN, S. L., ZARRIN, F. & DORMAN, F. D. 1994. Electrospray-condensation particle counter: a molecule-counting LC detector for macromolecules. *Analytical chemistry,* 66**,** 2285-2292.

LI, C. & HOGAN, C. J. 2017. Vapor specific extents of uptake by nanometer scale charged particles. *Aerosol Science and Technology,* 51**,** 653-664.

LI, C., LEE, A. L., CHEN, X., POMERANTZ, W. C., HAYNES, C. L. & HOGAN JR, C. J. 2020a. Multidimensional nanoparticle characterization through ion mobility-mass spectrometry. *Analytical chemistry,* 92**,** 2503-2510.

LI, C., SINGH, N., ANDREWS, A., OLSON, B. A., SCHWARTZENTRUBER, T. E. & HOGAN, C. J. 2019. Mass, momentum, and energy transfer in supersonic aerosol deposition processes. *International Journal of Heat and Mass Transfer,* 129**,** 1161-1171.

LI, L., CHAHL, H. S. & GOPALAKRISHNAN, R. 2020b. Comparison of the predictions of Langevin Dynamics-based diffusion charging collision kernel models with canonical experiments. *Journal of Aerosol Science,* 140**,** 105481.

LI, M., GUHA, S., ZANGMEISTER, R., TARLOV, M. J. & ZACHARIAH, M. R. 2011. Quantification and Compensation of Nonspecific Analyte Aggregation in Electrospray Sampling. *Aerosol Science and Technology,* 45**,** 849-860.

LINDQUIST, G. J., PUI, D. Y. H. & HOGAN JR, C. J. 2014. Porous particulate film deposition in the transition regime. *Journal of Aerosol Science,* 74**,** 42-51.

LIU, B. Y. & PUI, D. Y. 1974. A submicron aerosol standard and the primary, absolute calibration of the condensation nuclei counter. *Journal of Colloid and Interface Science,* 47**,** 155-171.

LIU, Y., ATTOUI, M., LI, Y., CHEN, J., LI, Q. & WANG, L. 2021. Characterization of a Kanomax® fast condensation particle counter in the sub-10 nm range. *Journal of Aerosol Science,* 155**,** 105772.

LIU, Y., ATTOUI, M., YANG, K., CHEN, J., LI, Q. & WANG, L. 2020. Size-resolved chemical composition analysis of ions produced by a commercial soft X-ray aerosol neutralizer. *Journal of Aerosol Science,* 147**,** 105586.

LUZZATI, V., WITZ, J. & NICOLAIEFF, A. 1961. La structure de la sérum albumine de boeuf en solution à pH 5,3 et 3,6: Étude par diffusion centrale absolue des rayons X. *Journal of Molecular Biology,* 3**,** 379-392.

MAI, H., KONG, W., SEINFELD, J. H. & FLAGAN, R. C. 2018. Scanning DMA data analysis II. Integrated DMA-CPC instrument response and data inversion. *Aerosol Science and Technology,* 52**,** 1400-1414.

MAIBER, A., PREMNATH, V., GHOSH, A., NGUYEN, T. A., ATTOUI, M. & HOGAN, C. J. 2011. Determination of gas phase protein ion densities via ion mobility analysis with charge reduction. *Physical Chemistry Chemical Physics,* 13**,** 21630-21641.

MAISSER, A. & HOGAN, C. J. 2017. Examination of Organic Vapor Adsorption onto Alkali Metal and Halide Atomic Ions via Ion Mobility-Mass Spectrometry. *ChemPhysChem,* 18**,** 3039-3046.

MAISSER, A., THOMAS, J. M., LARRIBA-ANDALUZ, C., HE, S. & HOGAN, C. J. 2015. The Mass-Mobility Distributions of Ions Produced by a Po-210 Source in Air. *Journal of Aerosol Science,* 90**,** 36-50.

MAKINEN, M. A., ANTTALAINEN, O. A. & SILLANPÄÄ, M. E. 2010. Ion mobility spectrometry and its applications in detection of chemical warfare agents. ACS Publications.

MARICQ, M. M. & BILBY, D. 2018. The impact of voltage and flow on the electrostatic soot sensor and the implications for its use as a diesel particulate filter monitor. *Journal of Aerosol Science,* 124**,** 41-53.

MARTEL, P., KIM, S. & POWELL, B. 1980. Physical characteristics of human transferrin from small angle neutron scattering. *Biophysical Journal,* 31**,** 371-380.
MASON, E. A. & MCDANIEL, E. W. 1988a. *Transport properties of ions in gases,* Wiley, New York.
MASON, E. A. & MCDANIEL, E. W. 1988b. *Transport properties of ions in gases,* Wiley Online Library.
MASON, H. W. E. A. M. G. T. A. E. W. M. A. E. A. 1984. Transport properties of gaseous ions over a wide energy range. Part III. *Atomic Data and Nuclear Data Tables,* 31**,** 113-151.
MCCALLISTER, J. J. H., GAMMAGE, M. D., KETO, J. W., BECKER, M. F. & KOVAR, D. 2021. Influence of agglomerate morphology on micro cold spray of Ag nanopowders. *Journal of Aerosol Science,* 151**,** 105648.
MCDANIEL, E. W. & MASON, E. A. 1973. *The Mobility and Diffusion of Ions in Gases*.
MCMURRY, P. H. 2000. The history of condensation nucleus counters. *Aerosol Science & Technology,* 33**,** 297-322.
MEAKIN, P. 1986. Diffusion-limited surface deposition in the limit of large anisotropy. *Physical Review A,* 33**,** 1984-1989.
MEYER, N. A., ROOT, K., ZENOBI, R. & VIDAL-DE-MIGUEL, G. 2016. Gas-Phase Dopant-Induced Conformational Changes Monitored with Transversal Modulation Ion Mobility Spectrometry. *Analytical Chemistry,* 88**,** 2033-2040.
MILLER, R. A., NAZAROV, E. G., EICEMAN, G. A. & KING, A. T. 2001. A MEMS radio-frequency ion mobility spectrometer for chemical vapor detection. *Sensors and Actuators A: Physical,* 91**,** 301-312.
MILLIKAN, R. A. 1911. The Isolation of an Ion, a Precision Measurement of its Charge, and the Correction of Stokes's Law. *Physical Review (Series I),* 32**,** 349.
MILLIKAN, R. A. 1923. The general law of fall of a small spherical body through a gas, and its bearing upon the nature of molecular reflection from surfaces. *Physical Review,* 22**,** 1.
MORGENEYER, M., BRENDEL, L. & SCHWEDES, J. 2008. Compaction of bidisperse cohesive powders. *Granular Matter,* 10**,** 295.
MORGENEYER, M., RAMÍREZ-GÓMEZ, A., POLETTO, M., WARD-SMITH, S., TWEEDIE, R. J., HENG, J. Y. Y., MAASS, S. & BRESSOT, C. 2019. Particle technology as a uniform discipline? Towards a holistic approach to particles, their creation, characterisation, handling and processing! *Chemical Engineering Research and Design,* 146**,** 162-165.
MÄDLER, L., LALL, A. A. & FRIEDLANDER, S. K. 2006. One-step aerosol synthesis of nanoparticle agglomerate films: simulation of film porosity and thickness. *Nanotechnology,* 17**,** 4783-4795.
NASIBULIN, A. G., FERNANDEZ DE LA MORA, J. & KAUPPINEN, E. I. 2008. Ion-Induced Nucleation of Dibutyl Phthalate Vapors on Spherical and Nonspherical Singly and Multiply Charged Polyethylene Glycol Ions. *The Journal of Physical Chemistry A,* 112**,** 1133-1138.
NASIRI, N., ELMØE, T. D., LIU, Y., QIN, Q. H. & TRICOLI, A. 2015. Self-assembly dynamics and accumulation mechanisms of ultra-fine nanoparticles. *Nanoscale,* 7**,** 9859-9867.
NAYLOR, C. N., REINECKE, T. & CLOWERS, B. H. 2020. Assessing the Impact of Drift Gas Polarizability in Polyatomic Ion Mobility Experiments. *Analytical Chemistry,* 92**,** 4226-4234.
NICKEL, C., ANGELSTORF, J., BIENERT, R., BURKART, C., GABSCH, S., GIEBNER, S., HAASE, A., HELLACK, B., HOLLERT, H., HUND-RINKE, K., JUNGMANN, D., KAMINSKI, H., LUCH, A., MAES, H. M., NOGOWSKI, A., OETKEN, M., SCHAEFFER, A., SCHIWY, A., SCHLICH, K., STINTZ, M., VON DER KAMMER, F. & KUHLBUSCH, T. A. J. 2014. Dynamic light-scattering measurement comparability of nanomaterial suspensions. *Journal of Nanoparticle Research,* 16**,** 2260.

NOVICK, V. J., MONSON, P. R. & ELLISON, P. E. 1992. The effect of solid particle mass loading on the pressure drop of HEPA filters. *Journal of Aerosol Science,* 23**,** 657-665.

OBERREIT, D. R., RAWAT, V. K., LARRIBA-ANDALUZ, C., OUYANG, H., MCMURRY, P. H. & HOGAN, C. J. 2015. Analysis of heterogeneous water vapor uptake by metal iodide cluster ions via differential mobility analysis-mass spectrometry. *The Journal of Chemical Physics,* 143**,** 104204.

OGUNSOLA, O. & EHRMAN, S. 2008. A Monte Carlo and continuum study of mechanical properties of nanoparticle based films. *Journal of Nanoparticle Research,* 10**,** 31-39.

O'DONNELL, R. M., SUN, X. & HARRINGTON, P. D. B. 2008. Pharmaceutical applications of ion mobility spectrometry. *TrAC Trends in Analytical Chemistry,* 27**,** 44-53.

PARK, K., DUTCHER, D., EMERY, M., PAGELS, J., SAKURAI, H., SCHECKMAN, J., QIAN, S., STOLZENBURG, M. R., WANG, X., YANG, J. & MCMURRY, P. H. 2008. Tandem Measurements of Aerosol Properties—A Review of Mobility Techniques with Extensions. *Aerosol Science and Technology,* 42**,** 801-816.

PEREZ-LORENZO, L. J. & DE LA MORA, J. F. 2021. Exceeding a resolving power of 50 for virus size determination by differential mobility analysis. *Journal of Aerosol Science,* 151**,** 105658.

PETTERS, M. D. & KREIDENWEIS, S. M. 2007. A single parameter representation of hygroscopic growth and cloud condensation nucleus activity. *Atmos. Chem. Phys.,* 7**,** 1961-1971.

PHILIPOSSIAN, A. & MITCHELL, E. 2003. Slurry utilization efficiency studies in chemical mechanical planarization. *Japanese journal of applied physics,* 42**,** 7259.

POHL, M. C. & GRIFFITHS, D. A. 1996. The importance of particle size to the performance of abrasive particles in the CMP process. *Journal of Electronic Materials,* 25**,** 1612-1616.

PURVES, R. W., BARNETT, D. A., ELLS, B. & GUEVREMONT, R. 2000. Investigation of bovine ubiquitin conformers separated by high-field asymmetric waveform ion mobility spectrometry: cross section measurements using energy-loss experiments with a triple quadrupole mass spectrometer. *Journal of the American Society for Mass Spectrometry,* 11**,** 738-745.

PURVES, R. W., GUEVREMONT, R., DAY, S., PIPICH, C. W. & MATYJASZCZYK, M. S. 1998. Mass spectrometric characterization of a high-field asymmetric waveform ion mobility spectrometer. *Review of Scientific Instruments,* 69**,** 4094-4105.

PURVES, R. W., OZOG, A. R., AMBROSE, S. J., PRASAD, S., BELFORD, M. & DUNYACH, J.-J. 2014. Using Gas Modifiers to Significantly Improve Sensitivity and Selectivity in a Cylindrical FAIMS Device. *Journal of the American Society for Mass Spectrometry,* 25**,** 1274-1284.

RADER, D. J. 1990. Momentum slip correction factor for small particles in nine common gases. *Journal of aerosol science,* 21**,** 161-168.

RADER, D. J. & MCMURRY, P. H. 1986. Application of the tandem differential mobility analyzer to studies of droplet growth or evaporation. *Journal of Aerosol Science,* 17**,** 771-787.

RAWAT, V. K., VIDAL-DE-MIGUEL, G. & HOGAN, C. J. 2015. Modeling vapor uptake induced mobility shifts in peptide ions observed with transversal modulation ion mobility spectrometry-mass spectrometry. *Analyst,* 140**,** 6945-6954.

REMSEN, E. E., ANJUR, S., BOLDRIDGE, D., KAMITI, M., LI, S., JOHNS, T., DOWELL, C., KASTHURIRANGAN, J. & FEENEY, P. 2006. Analysis of large particle count in fumed silica slurries and its correlation with scratch defects generated by CMP. *Journal of The Electrochemical Society,* 153**,** G453.

REVERCOMB, H. & MASON, E. A. 1975a. Theory of plasma chromatography/gaseous electrophoresis. Review. *Analytical Chemistry,* 47**,** 970-983.

REVERCOMB, H. E. & MASON, E. A. 1975b. Theory of Plasma Chromatography Gaseous Electrophoresis - Review. *Analytical Chemistry,* 47**,** 970-983.

ROBERTS, R. C., MAKEY, D. G. & SEAL, U. S. 1966. Human transferrin: molecular weight and sedimentation properties. *Journal of Biological Chemistry,* 241**,** 4907-4913.
ROBINSON, E. W. & WILLIAMS, E. R. 2005. Multidimensional separations of ubiquitin conformers in the gas phase: relating ion cross sections to H/D exchange measurements. *Journal of the American Society for Mass Spectrometry,* 16**,** 1427-1437.
RODRÍGUEZ-PÉREZ, D., CASTILLO, J. L. & ANTORANZ, J. C. 2005. Relationship between particle deposit characteristics and the mechanism of particle arrival. *Physical Review E,* 72**,** 021403.
ROEHL, J. E. 1991. Environmental and process applications for ion mobility spectrometry. *Applied Spectroscopy Reviews,* 26**,** 1-57.
ROGAK, S. N., FLAGAN, R. C. & NGUYEN, H. V. 1993. The mobility and structure of aerosol agglomerates. *Aerosol Science and Technology,* 18**,** 25-47.
RORRER, L. C. & YOST, R. A. 2011. Solvent vapor effects on planar high-field asymmetric waveform ion mobility spectrometry. *International Journal of Mass Spectrometry,* 300**,** 173-181.
RORRER, L. C. & YOST, R. A. 2015. Solvent vapor effects in planar high-field asymmetric waveform ion mobility spectrometry: Solvent trends and temperature effects. *International Journal of Mass Spectrometry,* 378**,** 336-346.
ROSSER, S. & DE LA MORA, J. F. 2005. Vienna-type DMA of high resolution and high flow rate. *Aerosol Science and Technology,* 39**,** 1191-1200.
ROTH, G. A., NEU-BAKER, N. M. & BRENNER, S. A. 2015. Comparative characterization methods for metal oxide nanoparticles in aqueous suspensions. *Journal of Chemical Health & Safety,* 22**,** 26-32.
ROUQUEROL, J., ROUQUEROL, F., LLEWELLYN, P., MAURIN, G. & SING, K. S. 2013. *Adsorption by powders and porous solids: principles, methodology and applications*, Academic Press
RUOTOLO, B. T., BENESCH, J. L. P., SANDERCOCK, A. M., HYUNG, S. J. & ROBINSON, C. V. 2008. Ion mobility-mass spectrometry analysis of large protein complexes. *Nature Protocols,* 3**,** 1139-1152.
RUOTOLO, B. T., GILES, K., CAMPUZANO, I., SANDERCOCK, A. M., BATEMAN, R. H. & ROBINSON, C. V. 2005. Evidence for macromolecular protein rings in the absence of bulk water. *Science,* 310**,** 1658-1661.
RUOTOLO, B. T. & ROBINSON, C. V. 2006. Aspects of native proteins are retained in vacuum. *Current Opinion in Chemical Biology,* 10**,** 402-408.
RUS, J., MORO, D., SILLERO, J., FREIXA, J. & DE LA MORA, J. F. A high flow rate DMA with high transmission and resolution designed for new API instruments. 56th ASMS Conference on Mass Spectrometry and Allied Topics, 2008.
RUS, J., MORO, D., SILLERO, J. A., ROYUELA, J., CASADO, A., ESTEVEZ-MOLINERO, F. & DE LA MORA, J. F. 2010. IMS–MS studies based on coupling a differential mobility analyzer (DMA) to commercial API–MS systems. *International Journal of Mass Spectrometry,* 298**,** 30-40.
RUSINQUE, H., FEDIANINA, E., WEBER, A. & BRENNER, G. 2019. Numerical study of the controlled electrodeposition of charged nanoparticles in an electric field. *Journal of Aerosol Science,* 129**,** 28-39.
SCALF, M., WESTPHALL MICHAEL, S., KRAUSE, J., KAUFMAN STANLEY, L. & SMITH LLOYD, M. 1999. Controlling Charge States of Large Ions. *Science,* 283**,** 194-197.
SCALF, M., WESTPHALL, M. S. & SMITH, L. M. 2000. Charge Reduction Electrospray Mass Spectrometry. *Analytical Chemistry,* 72**,** 52-60.
SCHLAG, L., ISAAC, N. A., NAHRSTEDT, H., REIPRICH, J., ISPAS, A., STAUDEN, T., PEZOLDT, J., BUND, A. & JACOBS, H. O. 2020. Nanoparticle gas phase

electrodeposition: Fundamentals, fluid dynamics, and deposition kinetics. *Journal of Aerosol Science*, 105652.

SCHNEIDER, B. B., COVEY, T. R. & NAZAROV, E. G. 2013. DMS-MS separations with different transport gas modifiers. *International Journal for Ion Mobility Spectrometry,* 16**,** 207-216.

SEATON, N. & WALTON, J. 1989. A new analysis method for the determination of the pore size distribution of porous carbons from nitrogen adsorption measurements. *Carbon,* 27**,** 853-861.

SHIMADA, M., HAN, B., OKUYAMA, K. & OTANI, Y. 2002. Bipolar charging of aerosol nanoparticles by a soft X-ray photoionizer. *Journal of Chemical Engineering of Japan,* 35**,** 786-793.

SHIN, C., CHOI, J., KWAK, D., KIM, J., YANG, J., CHAE, S.-K. & KIM, T. 2019. Evaluation of Size Distribution Measurement Methods for Sub-100 nm Colloidal Silica Nanoparticles and Its Application to CMP Slurry. *ECS Journal of Solid State Science and Technology,* 8**,** P3195.

SHVARTSBURG, A. A., BRYSKIEWICZ, T., PURVES, R. W., TANG, K., GUEVREMONT, R. & SMITH, R. D. 2006. Field asymmetric waveform ion mobility spectrometry studies of proteins: Dipole alignment in ion mobility spectrometry? *The Journal of Physical Chemistry B,* 110**,** 21966-21980.

SHVARTSBURG, A. A., SMITH, R. D., WILKS, A., KOEHL, A., RUIZ-ALONSO, D. & BOYLE, B. 2009. Ultrafast differential ion mobility spectrometry at extreme electric fields in multichannel microchips. *Analytical chemistry,* 81**,** 6489-6495.

STOLZENBURG, M. R. 1988. *An ultrafine aerosol size distribution measuring system.* University of Minnesota.

STOLZENBURG, M. R. 2018. A review of transfer theory and characterization of measured performance for differential mobility analyzers. *Aerosol Science and Technology,* 52**,** 1194-1218.

STOLZENBURG, M. R. & MCMURRY, P. H. 1991. An ultrafine aerosol condensation nucleus counter. *Aerosol Science and Technology,* 14**,** 48-65.

STOLZENBURG, M. R. & MCMURRY, P. H. 2008. Equations governing single and tandem DMA configurations and a new lognormal approximation to the transfer function. *Aerosol Science and Technology,* 42**,** 421-432.

STRATMANN, F., KAUFFELDT, T., HUMMES, D. & FISSAN, H. 1997. Differential electrical mobility analysis: A theoretical study. *Aerosol Science and Technology,* 26**,** 368-383.

SUZUKI, M., TSUCHIYA, T. & AKEDO, J. 2017. Effect of starting powder morphology on film texture for bismuth layer-structured ferroelectrics prepared by aerosol deposition method. *Japanese Journal of Applied Physics,* 56**,** 06GH02.

TAMADATE, T., HIGASHI, H., HOGAN, C. J. & SETO, T. 2020. The charge reduction rate for multiply charged polymer ions via ion–ion recombination at atmospheric pressure. *Physical Chemistry Chemical Physics,* 22**,** 25215-25226.

TAMMET, H. 1995. Size and mobility of nanometer particles, clusters and ions. *Journal of Aerosol Science,* 26**,** 459-475.

TANG, J. & GOMEZ, A. 2017. Controlled mesoporous film formation from the deposition of electrosprayed nanoparticles. *Aerosol Science and Technology,* 51**,** 755-765.

TASSOPOULOS, M., O'BRIEN, J. A. & ROSNER, D. E. 1989. Simulation of microstructure/mechanism relationships in particle deposition. *AIChE Journal,* 35**,** 967-980.

THAJUDEEN, T., GOPALAKRISHNAN, R. & HOGAN JR, C. J. 2012. The collision rate of nonspherical particles and aggregates for all diffusive Knudsen numbers. *Aerosol Science and Technology,* 46**,** 1174-1186.

THAJUDEEN, T., JEON, S. & HOGAN JR, C. J. 2015. The mobilities of flame synthesized aggregates/agglomerates in the transition regime. *Journal of Aerosol Science,* 80**,** 45-57.

THIMSEN, E. & BISWAS, P. 2007. Nanostructured photoactive films synthesized by a flame aerosol reactor. *AIChE Journal,* 53**,** 1727-1735.

THIMSEN, E., JOHNSON, M., ZHANG, X., WAGNER, A. J., MKHOYAN, K. A., KORTSHAGEN, U. R. & AYDIL, E. S. 2014. High electron mobility in thin films formed via supersonic impact deposition of nanocrystals synthesized in nonthermal plasmas. *Nature Communications,* 5**,** 5822.

THIMSEN, E., RASTGAR, N. & BISWAS, P. 2008. Nanostructured TiO2 films with controlled morphology synthesized in a single step process: Performance of dye-sensitized solar cells and photo watersplitting. *Journal of Physical Chemistry C,* 112**,** 4134-4140.

THOMAS, J. M., HE, S., LARRIBA-ANDALUZ, C., DEPALMA, J. W., JOHNSTON, M. V. & HOGAN, C. J. 2016. Ion Mobility Spectrometry-Mass Spectrometry Examination of the Structures, Stability, and Extent of Hydration of Dimethylamine-Sulfuric Acid Clusters. *Physical Chemistry Chemical Physics,* 18**,** 22962-22972

TOLMACHOFF, E. D., ABID, A. D., PHARES, D. J., CAMPBELL, C. S. & WANG, H. 2009. Synthesis of nano-phase TiO(2) crystalline films over premixed stagnation flames. *Proceedings of the Combustion Institute,* 32**,** 1839-1845.

TRICOLI, A. & ELMØE, T. D. 2012. Flame spray pyrolysis synthesis and aerosol deposition of nanoparticle films. *AIChE Journal,* 58**,** 3578-3588.

TYNDALL, A. M. 1938. *The mobility of positive ions in gases,* The University Press.

UDE, S. & DE LA MORA, J. F. 2005. Molecular monodisperse mobility and mass standards from electrosprays of tetra-alkyl ammonium halides. *Journal of Aerosol Science,* 36**,** 1224-1237.

VALENTINE, S. J., PLASENCIA, M. D., LIU, X., KRISHNAN, M., NAYLOR, S., UDSETH, H. R., SMITH, R. D. & CLEMMER, D. E. 2006. Toward plasma proteome profiling with ion mobility-mass spectrometry. *Journal of proteome research,* 5**,** 2977-2984.

VIEHLAND, L. & MASON, E. 1995. Transport properties of gaseous ions over a wide energy range, IV. *Atomic Data and Nuclear Data Tables,* 60**,** 37-95.

VULIC, N., CARPENTER, J. V., FIRTH, P., RODKEY, N., HOLMAN, Z. C. & GOODNICK, S. M. 2019. Pore Formation in Silicon Nanoparticle Thin Films and Its Impact on Optical Properties. *ACS Applied Energy Materials,* 2**,** 8587-8595.

WANG, H., ZHAO, Q., XIE, S., ZHOU, H. & HE, Y. 2020. Effect of Abrasive Particle Size Distribution on Removal Rate of Silicon Wafers. *ECS Journal of Solid State Science and Technology,* 9**,** 124001.

WANG, S. C. & FLAGAN, R. C. 1990. Scanning electrical mobility spectrometer. *Aerosol Science and Technology,* 13**,** 230-240.

WANG, X., MA, N., LEI, T., GRÖß, J., LI, G., LIU, F., MEUSEL, H., MIKHAILOV, E., WIEDENSOHLER, A. & SU, H. 2019. Effective density and hygroscopicity of protein particles generated with spray-drying process. *Journal of Aerosol Science,* 137**,** 105441.

WARAKSA, E., PERYCZ, U., NAMIEŚNIK, J., SILLANPÄÄ, M., DYMERSKI, T., WÓJTOWICZ, M. & PUTON, J. 2016. Dopants and gas modifiers in ion mobility spectrometry. *TrAC Trends in Analytical Chemistry,* 82**,** 237-249.

WEGNER, K., VINATI, S., PISERI, P., ANTONINI, A., ZELIOLI, A., BARBORINI, E., DUCATI, C. & MILANI, P. 2012. High-rate production of functional nanostructured films and devices by coupling flame spray pyrolysis with supersonic expansion. *Nanotechnology,* 23**,** 185603.

WEI, G., LIU, Y., ZHANG, X., YU, F. & DU, X. 2011. Thermal conductivities study on silica aerogel and its composite insulation materials. *International Journal of Heat and Mass Transfer,* 54**,** 2355-2366.

WEI, M. S., KEMPERMAN, R. H. & YOST, R. A. 2019. Effects of solvent vapor modifiers for the separation of opioid isomers in micromachined FAIMS-MS. *Journal of The American Society for Mass Spectrometry,* 30**,** 731-742.

WIEDENSOHLER, A. 1988. An approximation of the bipolar charge distribution for particles in the submicron size range. *Journal of aerosol science,* 19**,** 387-389.

WIEDENSOHLER, A., BIRMILI, W., NOWAK, A., SONNTAG, A., WEINHOLD, K., MERKEL, M., WEHNER, B., TUCH, T., PFEIFER, S., FIEBIG, M., FJÄRAA, A. M., ASMI, E., SELLEGRI, K., DEPUY, R., VENZAC, H., VILLANI, P., LAJ, P., AALTO, P., OGREN, J. A., SWIETLICKI, E., WILLIAMS, P., ROLDIN, P., QUINCEY, P., HÜGLIN, C., FIERZ-SCHMIDHAUSER, R., GYSEL, M., WEINGARTNER, E., RICCOBONO, F., SANTOS, S., GRÜNING, C., FALOON, K., BEDDOWS, D., HARRISON, R., MONAHAN, C., JENNINGS, S. G., O'DOWD, C. D., MARINONI, A., HORN, H. G., KECK, L., JIANG, J., SCHECKMAN, J., MCMURRY, P. H., DENG, Z., ZHAO, C. S., MOERMAN, M., HENZING, B., DE LEEUW, G., LÖSCHAU, G. & BASTIAN, S. 2012. Mobility particle size spectrometers: harmonization of technical standards and data structure to facilitate high quality long-term observations of atmospheric particle number size distributions. *Atmos. Meas. Tech.,* 5**,** 657-685.

WILKS, A., HART, M., KOEHL, A., SOMERVILLE, J., BOYLE, B. & RUIZ-ALONSO, D. 2012. Characterization of a miniature, ultra-high-field, ion mobility spectrometer. *International Journal for Ion Mobility Spectrometry,* 15**,** 199-222.

WILSON, C. T. R. 1911. On a method of making visible the paths of ionising particles through a gas. *Proceedings of the Royal Society of London. Series A, Containing Papers of a Mathematical and Physical Character,* 85**,** 285-288.

WILSON, C. T. R. 1912. On an expansion apparatus for making visible the tracks of ionising particles in gases and some results obtained by its use. *Proceedings of the Royal Society of London. Series A, Containing Papers of a Mathematical and Physical Character,* 87**,** 277-292.

WILSON, C. T. R. 1933. On a new type of expansion apparatus. *Proceedings of the Royal Society of London. Series A, Containing Papers of a Mathematical and Physical Character,* 142**,** 88-91.

WOOD, D. L. & NASSAU, K. 1982. Refractive index of cubic zirconia stabilized with yttria. *Applied Optics,* 21**,** 2978-2981.

XIE, Y. & BHUSHAN, B. 1996. Effects of particle size, polishing pad and contact pressure in free abrasive polishing. *Wear,* 200**,** 281-295.

YANG, G., BISWAS, P., BOOLCHAND, P. & SABATA, A. 1999. Deposition of Multifunctional Titania Ceramic Films by Aerosol Routes. *Journal of the American Ceramic Society,* 82**,** 2573-2579.

YOU, R., LI, M., GUHA, S., MULHOLLAND, G. W. & ZACHARIAH, M. R. 2014. Bionanoparticles as Candidate Reference Materials for Mobility Analysis of Nanoparticles. *Analytical Chemistry,* 86**,** 6836-6842.

ZENG, S. Q., HUNT, A. J., CAO, W. & GREIF, R. 1994. Pore Size Distribution and Apparent Gas Thermal Conductivity of Silica Aerogel. *Journal of Heat Transfer,* 116**,** 756-759.

ZHANG, C., THAJUDEEN, T., LARRIBA, C., SCHWARTZENTRUBER, T. E. & HOGAN, C. J. 2012a. Determination of the Scalar Friction Factor for Non-spherical Particles and Aggregates Across the Entire Knudsen Number Range by Direct Simulation Monte Carlo (DSMC). *Aerosol Science and Technology,* 46**,** 1065-1078.

ZHANG, C., THAJUDEEN, T., LARRIBA, C., SCHWARTZENTRUBER, T. E. & HOGAN JR, C. J. 2012b. Determination of the scalar friction factor for nonspherical particles and aggregates across the entire Knudsen number range by direct simulation Monte Carlo (DSMC). *Aerosol Science and Technology,* 46**,** 1065-1078.

ZHANG, Y. Y., LI, S. Q., DENG, S. L., YAO, Q. & TSE, S. D. 2012c. Direct synthesis of nanostructured TiO2 films with controlled morphologies by stagnation swirl flames. *Journal of Aerosol Science,* 44**,** 71-82.

ZHANG, Z., LIU, W., SONG, Z. & HU, X. 2010. Two-Step Chemical Mechanical Polishing of Sapphire Substrate. *Journal of The Electrochemical Society,* 157**,** H688.

ZHU, T., LI, C., YANG, W., ZHAO, X., WANG, X., TANG, C., MI, B., GAO, Z., HUANG, W. & DENG, W. 2013. Electrospray Dense Suspensions of TiO2 Nanoparticles for Dye Sensitized Solar Cells. *Aerosol Science and Technology,* 47**,** 1302-1309.